UNIVERSITÉ DE SHERBROOKE

Faculté de génie
Département de génie chimique et de génie biotechnologique

Analyse du Transfert de Chaleur par Ébullition et Condensation à l'Intérieur d'un Caloduc Horizontal

Thèse de doctorat
Spécialité : génie chimique

Roshanak Rabiee

Jurés:
Prof. Martin Désilets (Directeur)
Prof. Pierre Proulx (co-directeur)
Prof. Jocelyn Veilleux (Rapporteur)
Prof. Louis Gosselin (Examinateur)
Prof. Sébastien Poncet (Examinateur)

Université de Sherbrooke

Sherbrooke (Québec) Canada

Mars 2019

Document adopté à la Faculté de génie de l'Université de Sherbrooke par le Comité de la recherche et des études supérieures et le Comité des programmes (2019).

À ma mère

RÉSUMÉ

L'utilisation de différents types de caloducs dans les systèmes de climatisation, de ventilation et d'évacuation de la chaleur a considérablement augmenté. Les caloducs sont des dispositifs de transfert de chaleur à deux phases générant un flux de chaleur élevé avec un faible gradient de température et une perte de charge minimale. La réduction des coûts de maintenance est l'un des avantages de l'utilisation de caloducs, due à l'absence de pièces mécaniques, à la réduction de l'espace occupé et à la surveillance, la fabrication et la maintenance simplifiées. Les caloducs sont des conducteurs thermiques très efficaces en raison des flux de chaleur élevés obtenus lors de l'évaporation et de la condensation du fluide de travail. Pour optimiser les performances d'un caloduc, il est nécessaire d'étudier précisément ce qui se passe à l'intérieur des sections de l'évaporateur et du condenseur.

Ce projet consiste à développer un modèle numérique simulant un écoulement diphasique à l'intérieur d'un caloduc à l'aide de codes CFD développés dans OpenFOAM. Le modèle est capable de prédire les principales variables représentant le comportement des deux phases telles que la vitesse, la température, la pression et la fraction volumique de chaque phase dans l'évaporateur ou le condenseur. Une attention particulière est consacrée à la simulation de la condensation car il n'existe pas de modèle numérique de ce type dans la littérature pour l'analyse du transfert de chaleur par condensation. En outre, une combinaison d'ébullition et de condensation dans un caloduc est une autre contribution de ce travail. Dans ce projet, le modèle de fractionnement du flux thermique de la paroi dans le cadre de l'approche eulérienne en deux phases a été appliqué. L'effet du transfert de quantité de mouvement et du transfert d'énergie entre les deux phases est également pris en compte.

La capacité du modèle numérique a été validée par des données expérimentales obtenues à partir d'essais réalisés sur un prototype construit à l'Université de Sherbrooke. Ensuite, un modèle validé est utilisé pour évaluer les performances de ce caloduc. Enfin, deux types de structures de gorge ont été suggérés et des tests expérimentaux ont été effectués pour étudier toute amélioration des performances du caloduc.

Mots-clés : flux en deux phases, modèle d'Euler-Euler, caloduc, ébullition et condensation, résistance thermique, tube lisse horizontal, fraction de surface.

ABSTRACT

The usage of different types of heat pipe in air conditioning, ventilation and heat removal systems has tremendously increased. Heat pipes are two-phase heat transfer devices and they are generating high heat flux with minimum temperature gradient and pressure drop. Lower service costs, due to the absence of mechanical parts, less occupied space and easier monitoring, manufacturing and maintenance are some of the advantages of using heat pipes. Heat pipes are highly effective thermal conductors due to the high heat fluxes obtained during boiling and condensation. For the optimization of heat pipe performances, it is necessary to study what happens inside the evaporator and condenser sections, precisely.

This project deals with the development of a numerical model to simulate the two-phase flow inside of the heat pipe using CFD codes developed in OpenFOAM. The model is able to predict the main two-phase variables such as velocity, temperature, pressure and volume fractions of each phase in the evaporator or condenser. Special attention is devoted to the simulation of condensation since there is no such numerical model in the open literature for the analysis of condensation heat transfer. In addition, the combination of boiling and condensation inside the heat pipe is another contribution of this work. In this project, a wall heat flux partition model in the framework of two-phase Eulerian approach has been applied. The effect of the interfacial momentum and energy transfer between the two phases is also taken account.

The capability of numerical model was validated by comparing numerical prediction with experimental data obtained from tests which have been conducted using a built-up prototype designed at Université de Sherbrooke. Then, the validated numerical model is used to assess the performances of this heat pipe. Finally, two types of grooves have been suggested and some experimental tests were performed to investigate any improvement in the heat pipe performance.

Keywords Two-phase flow, Euler-Euler model, heat pipe, boiling and condensation, thermal resistance, horizontal smooth tube, area fraction.

ACKNOWLEDGMENTS

This thesis is dedicated to my mother and my family who always loved and supported me. A special acknowledgement should be made to my mother for her patience and love along the completion of this degree. I would like to acknowledge my beloved father and dedicate this thesis to the memories he hacked in my heart.

I would like to thank my supervisors, Prof. Désilets, for guiding me and helping me to reach my potential. Prof. Désilets is admirable for both personal and professional attributes that he has. Many thanks to Prof. Proulx for his helps to complete this degree. I learned a lot from his collaboration.

I would also like to warmly thank my committee members, Professor Veilleux, Professor Poncet and Professor Gosselin for their precise and valuable comments.

Also, want to thank all my colleagues at UdeS, who have been good friends. Being a part of this group was a pleasure for me.

TABLE OF CONTENTS

List of Figures

List of Tables

List of Symbols

Latin Symbols		
A	Surface area	m^2
A_w	Contact area per unit volume	m^{-1}
A_b	Boiling area fraction	---
A_c	Condensation area fraction	---
a_L	Experimental parameter	---
C_D	Drag coefficient	---
C_L	Lift coefficient	---
C_{wL}	Wall lubrication coefficient	---
C_P	Specific heat capacity	kJ/kg.K
C_{sf}	Experimental constant that depends on surface-fluid combination	---
C_{hl}	Liquid Stanton number	---
C_f	Fanning friction factor	---
Co	Condensation number	---
C_{sf}	Experimental constant for surface-fluid interaction	---
d_w	Bubble departure diameter	m
d_w^c	Liquid droplet diameter	m
D	Hydraulic diameter	m
f	Detachment frequency	Hz or s^{-1}
g	Gravity	m/s^2
h	Heat transfer coefficient	$W/m^2.K$
i	Specific Enthalpy	J/kg
I^t	Identity matrix	---
I	Electrical current	A
J_v	Dimensionless vapor velocity	---
G	Inlet mass flux	$kg/m^2.s$
h_{lv}	Latent heat (vaporization latent heat)	J/kg
H_c	Stanton heat transfer coefficient	---
k^t	Kinetic energy of turbulent	J/kg
L	Length of tube	m
q_a	Conductive heat flux	W/m^2
q_a^t	Turbulent conductive heat flux	W/m^2
q''_{wall}	Wall heat flux	W/m^2
$q^{c''}_{wall}$	Single-phase convective heat flux	W/m^2
$q^{e''}_{wall}$	Evaporation heat flux	W/m^2
$q^{q''}_{wall}$	Quenching heat flux	W/m^2

$q_{wall}^{cd"}$	Condensation heat flux	W/m^2
$\bar{M}$	Molecular weight	kg/mole
M_a	Interfacial momentum exchange between two phases	N.s
$\dot{\imath}$	Mass flux generated by boiling	$kg/m^2.s$
$\dot{\imath}$	Mass flux generated by condensation	$kg/m^2.s$
$N"$	Nucleation site density	m^{-2}
$\bar{R}$	Universal gas constant	kJ/mol.K
Nu	Nusselt number	---
Pr	Prandtl number	---
P	Pressure	Pa
Po	Power	W
P_r	Reduced pressure	---
U	Velocity	m/s
U_r	Relative velocity between two phases	m/s
V	Voltage drop	V
$\bar{M}_a$	Averaged inter-phase momentum transfer	N.s
M_a^d	Momentum of drag force	N.s
M_a^l	Momentum of lift force	N.s
M_a^{wl}	Momentum of lubrication force	N.s
M_a^{vm}	Momentum of virtual mass force	N.s
M_a^{td}	Momentum of turbulent dispersion force	N.s
Re	Reynolds number	---
R	Thermal resistance	K/W
R_{pe}	Radial thermal resistance of evaporator	K/W
R_{pc}	Radial thermal resistance of condenser	K/W
$R_{int.evap}$	Thermal resistance of boiling	K/W
$R_{int.cond}$	Thermal resistance of condenser	K/W
R_{pa}	Axial thermal resistance of wall	K/W
R_{wa}	Axial thermal resistance of wick	K/W
T	Temperature	K,°C
T_r	Reduced temperature	---
t	Time	s
x	Vapor quality (see Eq.4.24)	---
X_{tt}	Martinelli parameter	---
Greek symbols		
ρ	Density	kg/m^3
α	Phase fraction	---
Γ_{ba}^{+}	Evaporation rate per unit volume	$kg/s.m^3$
Γ_{ab}^{+}	Condensation rate per unit volume	$kg/s.m^3$
μ	Dynamic viscosity	$kg/s.m^3$
υ	Kinematic viscosity	m^2/s

$\dot{\iota}$	Volumetric flow rate	m^3/s
λ	Thermal conductivity	W/m.K
τ	Laminar viscosity stress	N/m^2
τ^t	Turbulent viscosity stress	N/m^2
σ	Surface tension	kg/s^2
σ_P	Uncertainty in power	---
σ_V	Uncertainty in voltage	---
σ_I	Uncertainty in current	---
σ_T	Uncertainty in temperature	---
σ_T	Uncertainty in thermal resistance	---
Δ	Delta or difference operator	---
∇	Gradient operator	---
subscripts		
adj	Adjacent to the wall	
a	Phase a or vapor	
b	Phase b or liquid	
crt	Critical	
cap	Capillary	
cond	Condenser	
corr	Correlation	
evap	Evaporator	
equiv	Equivalent	
exp	Experimental	
fric	Friction	
int	Interfacial	
l	Liquid	
num	Numerical	
ref	Reference	
sat	Saturation	
sim	Simulation	
static	Static	
sub	Subcooled	
sup	Superheat	
v	Vapor	
wall	Wall	
w	Water	
t	Turbulent	

1. CHAPTER ONE: Introduction

1.1 Heat exchanger and application of heat pipe

The common challenge in heating and cooling industry is to recover as much thermal energy as possible from waste air in order to heat incoming fresh air and save substantial energy during air conditioning or heating of buildings. Also, conventional heating and cooling systems occupy more space and they usually require fire control system, smoke damper and also pressure loss in duct which leads to higher energy consumption on air transport. However, one main objective of designing a heating and cooling system is to increase its thermal efficiency, occupy less space, having high heat transfer rate without pressure drop across the exchanger. High-pressure drop also causes a lot of noises in heat exchanger and also increases the manufacturing, operations and maintenance costs. Heat pipes are among new air conditioning technologies that can substitute conventional systems. Their lower service costs, higher thermal efficiency and easier monitoring, applicability, manufacturing and maintenance are some of the advantages of using heat pipes explaining increasing demand for using them in the design of heat and ventilation systems. Due to the high heat transfer coefficients in boiling and condensation regime, heat pipes are highly effective thermal conductors. The effective thermal conductivity varies with heat pipe length, and can approach 100 kW/m·K for long heat pipes, in comparison with approximately 0.4 kW/m·K for copper with the same dimension. A 15-cm-long, 0.6-cm-diameter horizontal cylindrical heat pipe with water inside, for example, can transfer 300W of heat with less than a 10 °C temperature drop from one end to the other. Some heat pipes have demonstrated a heat flux of more than 23 kW/cm². Because of these reasons, they are widely used in different areas such as heat sinks for cooling electrical components and computers, spacecraft thermal control system, solar thermal, permafrost cooling, ventilation or recovery systems and heat exchangers [1].

Heat pipe generally consists of an evaporator, condenser, adiabatic section and a working fluid, which undergoes a phase change process from liquid to vapor (boiling) in the evaporator and vapor to liquid (condensation) in the condenser. In other words, the working fluid rapidly absorbs large amounts of energy as latent heat of vaporization from a heat source and releases

it to the cooler side without any mechanical parts. Adiabatic section is only an intermediate part that connects the two sections.

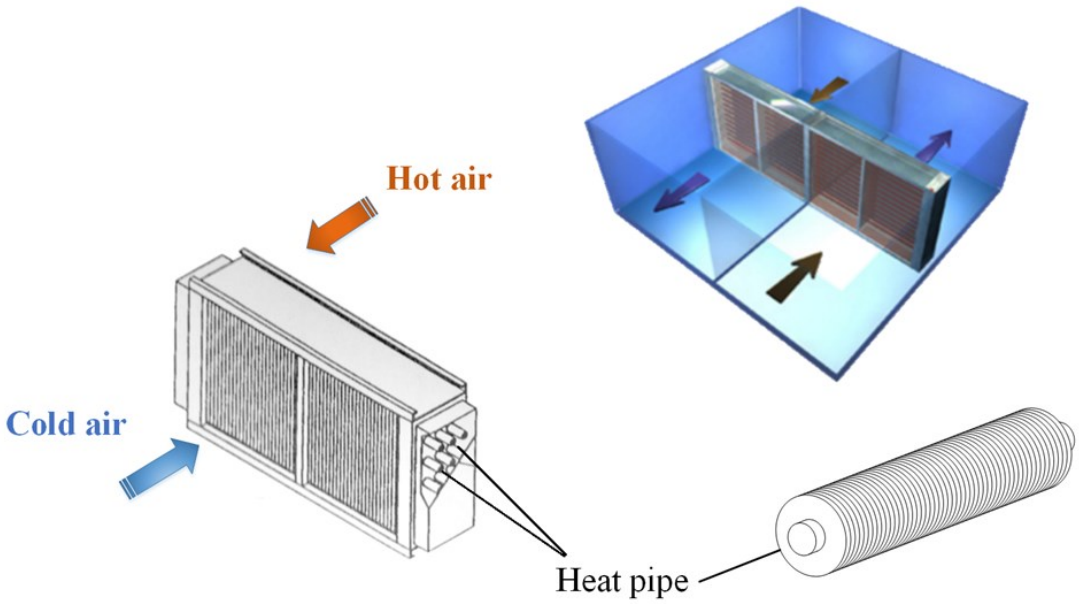

Figure 1-1: Heat pipe as part of a ventilation system-adapted figure from [2]

In order to analyze a heat pipe model, it is necessary to simulate each section and the phase changes that happened, precisely. The challenging work in the simulation of evaporator is the modeling of bubble formation that strictly affects the heat transfer rate. Moreover, there are few numerical works for estimation of heat transfer in the condensation regimes. The combination of boiling and condensation inside a heat exchanger like a heat pipe definitely brings challenging difficulties to solve. This complexity is increased even more when the system is a closed one because of small pressure variations in such applications.

The critical items for the design of an optimum heat pipe are the pipe material, dimensions, type of working fluid, operating conditions and surface roughness. The operation of a heat pipe is based on phase change and liquid-vapor interfaces. If the working fluid is heated above a certain temperature, evaporator would dry out and in this case, the thermal efficiency of the heat pipe is suddenly reduced. On the other hand, below a certain temperature, the working fluid will not undergo boiling and the evaporator will not work properly, the heat pipe will be flooded by condensed vapor and again its performance is considerably degraded. The pipe dimensions

control the surface area and consequently influence the heat transfer rate. The type of working fluid and pipe material is influencing the liquid-vapor interface and affect phase change processes, directly. Surface roughness like existing grooves will increase the density of nucleation sites for initiating boiling and condensation. Therefore, it is necessary to evaluate the effect of these parameters on heat transfer for optimizing the behavior of a heat pipe.

1.2 Operation principles of heat pipe

Generally, a heat pipe consists of three main sections: an evaporator section, a condenser section and an adiabatic section (Figure 1-2). These components are inside of a sealed container (pipe wall and end caps) and an amount of working fluid circulates between sections. In some heat pipes, a wick structure, grooves or coating are added to the wall for helping the circulation of flow between the evaporator and condenser. However, based on the type of heat pipes, other forces like gravity, capillary, centrifugal, electrostatic and osmotic forces can help flow circulation between the two main sections. The working fluid should have the following properties: high latent heat of vaporization, high thermal conductivity, low viscosity and high surface tension.

When the heat is externally applied to the evaporator section, the saturated liquid vaporizes, and the pressure of the evaporator increases due to accumulation of vapor at the top. This phenomenon is pushing vapor flow towards the condenser where it condenses to liquid at the contact of the cooled walls maintained at a temperature below the saturation point. The liquid film at top section of the condenser falls down to the bottom where it accumulates and returns to the evaporator section. The vapor and liquid circulate continuously between evaporator and condenser due to pressure differences. Therefore, the heat pipe can continuously transport the latent heat of vaporization from the evaporator (hot zone) to the condenser section (colder zone) [3].

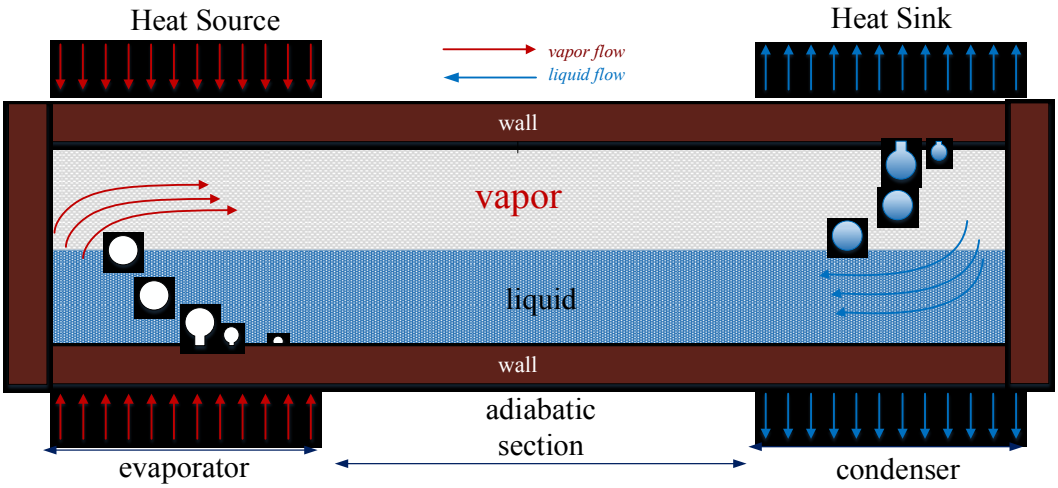

Figure 1-2: Vapor-liquid interface in a closed heat pipe-adapted figure from- [1]

1.3 A brief review of classification of heat pipes

There are various types of heat pipes used in air conditioning system including vertical, horizontal, annular, rotating and pulsating heat pipes. In this section, the main types of heat pipes are briefly introduced:

- **Two-Phase vertical heat pipe or thermosyphon**: In the case of a thermosyphon, the evaporator is located below the condenser section. There is no wick structure since gravity force can return liquid to evaporator. When heat is applied to the evaporator, the liquid is vaporized and flows upward to the condenser section. Vapor is then condensed on cooled walls and returns back to the evaporator section along the wall with the help of the gravity force (Figure 1-3).

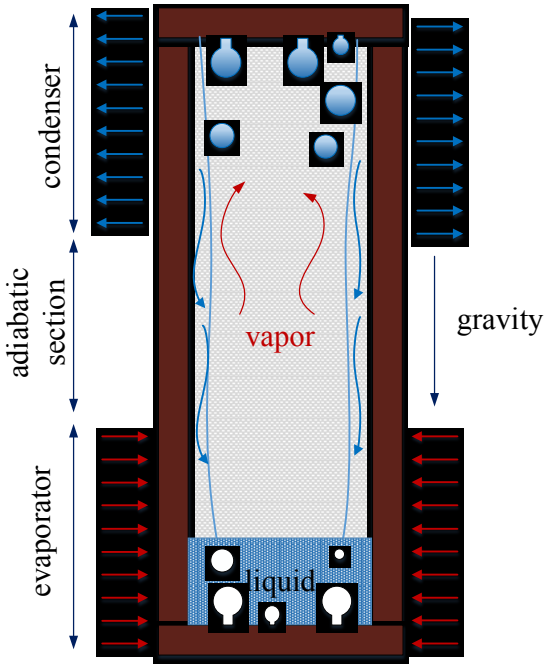

Figure 1-3: Gravity-assisted wickless heat pipe, thermosyphon- adapted figure from- [1]

- **Horizontal, capillary heat pipe**: In these heat exchangers, beside the evaporator, condenser and adiabatic sections, a wick structure is usually added to assist the liquid in returning to the evaporator. When heat is applied, the working fluid absorbs the latent heat and vaporizes. Then, the vapor moves to the condenser section driven by the pressure difference where it releases its latent heat to an external cooling system. Liquid then returns to the evaporator helped by capillary forces. (Figure 1-4).

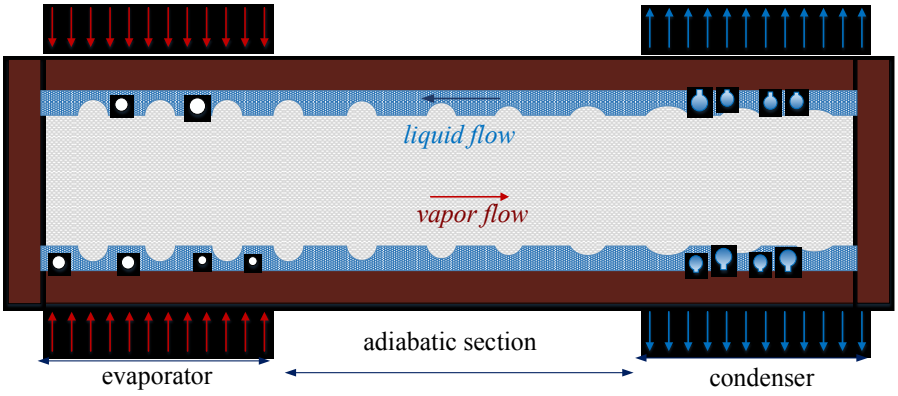

Figure 1-4: Conventional horizontal heat pipe with wick structure- adapted figure from- [1]

- **Rotating heat pipes:** In this type, a centrifugal force drives back the liquid to the evaporator (Figure 1-5). In disk-shaped heat pipes, heat is provided at the outer radius and extracted at the inner radius, which allows the flow to be driven back to the evaporator by the centrifugal force with the aid of an internal taper. Therefore, a wick structure is not used in rotating heat pipes. The cylindrical and disk rotating heat pipe are used in electrical motors, metal cutting tools, turbine components and automobile brakes.

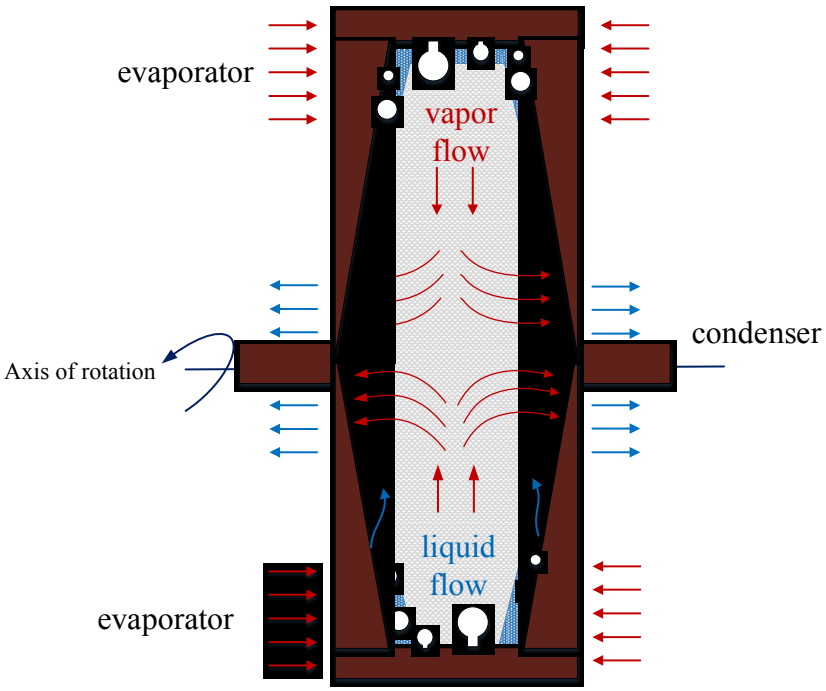

Figure 1-5: A sample of rotating heat pipe- adapted figure from- [1]

- **Pulsating heat pipes**: A long tube is bent into many sections, which causes liquid slug and vapor plug to fluctuate along the channel, periodically. The diameter of pulsating heat pipe is usually small (less than 5 mm) and vapor plug and liquid slug are formed across pipe as a result of capillary effect. An oscillating movement of vapor plug and liquid slug is generated due to pressure difference between cooling section and heating section. A sample of Un-looped and looped pulsating heat pipes is shown in Figure 1-6.

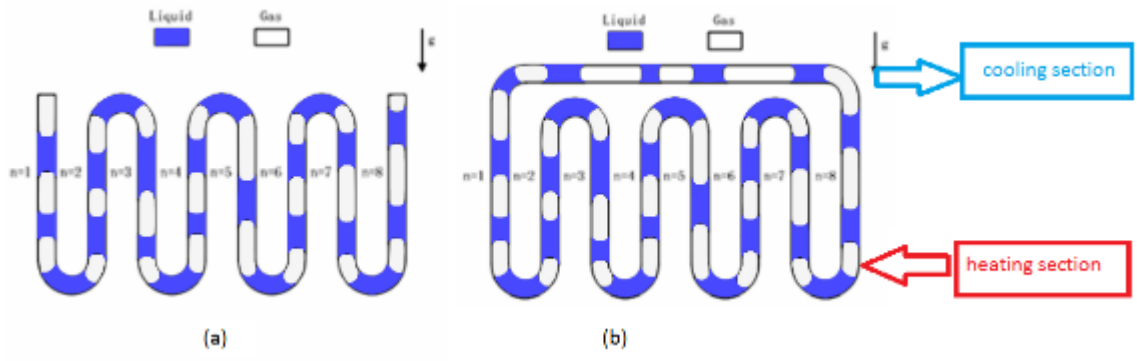

Figure 1-6: a) Un-looped pulsating heat pipe, b) looped pulsating heat pipe- adapted figure from- [3]

1.4 Operating limits of a heat pipe

The limiting parameters in the heat transport of conventional heat pipes are: viscous limit, sonic limit (shock happened at the end of the evaporator like at the throat of a nozzle), entrainment limit, capillary limit, boiling limit [3].

- **Viscous limit**: it mostly happens during start up, when the operating temperature is extremely low and the applied heat is small. In these conditions, the viscous force is larger than the pressure gradient and the liquid stream cannot overcome the friction force to circulate between sections.
- **Sonic limit**: with the increasing velocity of vapor in a long heat pipe, it can reach to sonic speed and a chock happened at the end of evaporator section. The sonic limit usually occurs in startup or steady condition of very long heat pipe.
- **Entrainment limit**: at high velocity, the shear forces at the liquid-vapor interface are increased and push the liquid to the condenser section. If the entrainment is too high, the evaporator can dry out. The entrainment limit has been seen in low temperature heat pipes with small diameters and high temperature heat pipe when applied heat at evaporator section is high.
- **Capillary limit:** this limitation is more critical in the design of low temperature heat pipes when the capillary pressure is not sufficient to return liquid to the evaporator section. Any attempt to increase the heat transfer above the capillary limit causes dry out of the evaporation section [3]. Capillary pressure must be greater than total pressure loss in order to drive liquid back to the evaporator. The total pressure drop in the system ΔP_{total} is the

sum of the pressure drop of vapor and liquid due to friction, hydrostatic pressure difference, pressure drops of vapor in the evaporator and the condenser [4].

$$\Delta P_{total} = \Delta P_l + \Delta P_v = \Delta P_{l,\text{fric}} + \Delta P_{l,static} + \Delta P_{v,evap} + \Delta P_{l,cond} \qquad (1.1)$$

Based on Young-Laplace equation, the capillary force must develop a pressure greater than the total pressure drop, under normal operation [more explanations are found in Appendix section 9.1]

$$\Delta P_{cap,\max} \geq \Delta P_{total} \qquad (1.2)$$

- **Boiling limit**: It happens due to high value of applied heat at evaporator, a situation which leads to dry out. The vapor bubbles that form in wick structure prevent the liquid to reach and wet the wall surface. The boiling limit is usually seen in a heat pipe with non-metallic working fluid [5].

Launay et al. [4] concluded that the boiling and capillary limit are the two main limitations in heat pipe performance and other factors have negligible effects. In order to increase the capillary force and boiling limit, the pore size in the evaporator, which acts as a nucleation site, should be as low as possible and the saturation pressure must be high enough. As shown in Figure 1-7, the maximum heat transport capability of heat pipe is constrained by the five limits mentioned before. A steady-state operating mode can only be reached in the area below this curve [6].

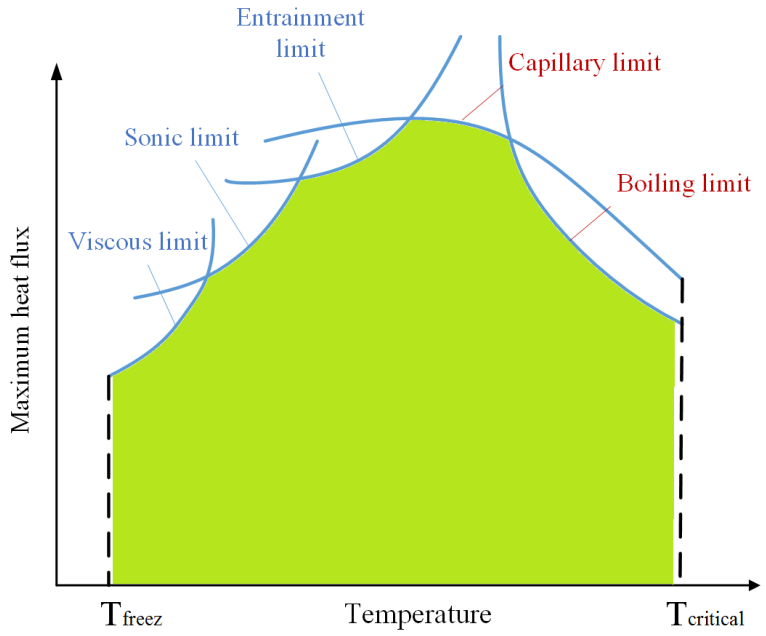

Figure 1-7: Heat transfer limitation in a heat pipe - adapted figure from [6]

1.5 Heat pipe function analysis

The thermal-fluid phenomena occurring in a heat pipe can be divided into four basic categories: (1) heat conduction in the wall or wick; (2) liquid flow in the wick structure; (3) interaction between the liquid and vapor and (4) vapor flow in the core region. The interaction between these regions is illustrated in (Figure 1-8).

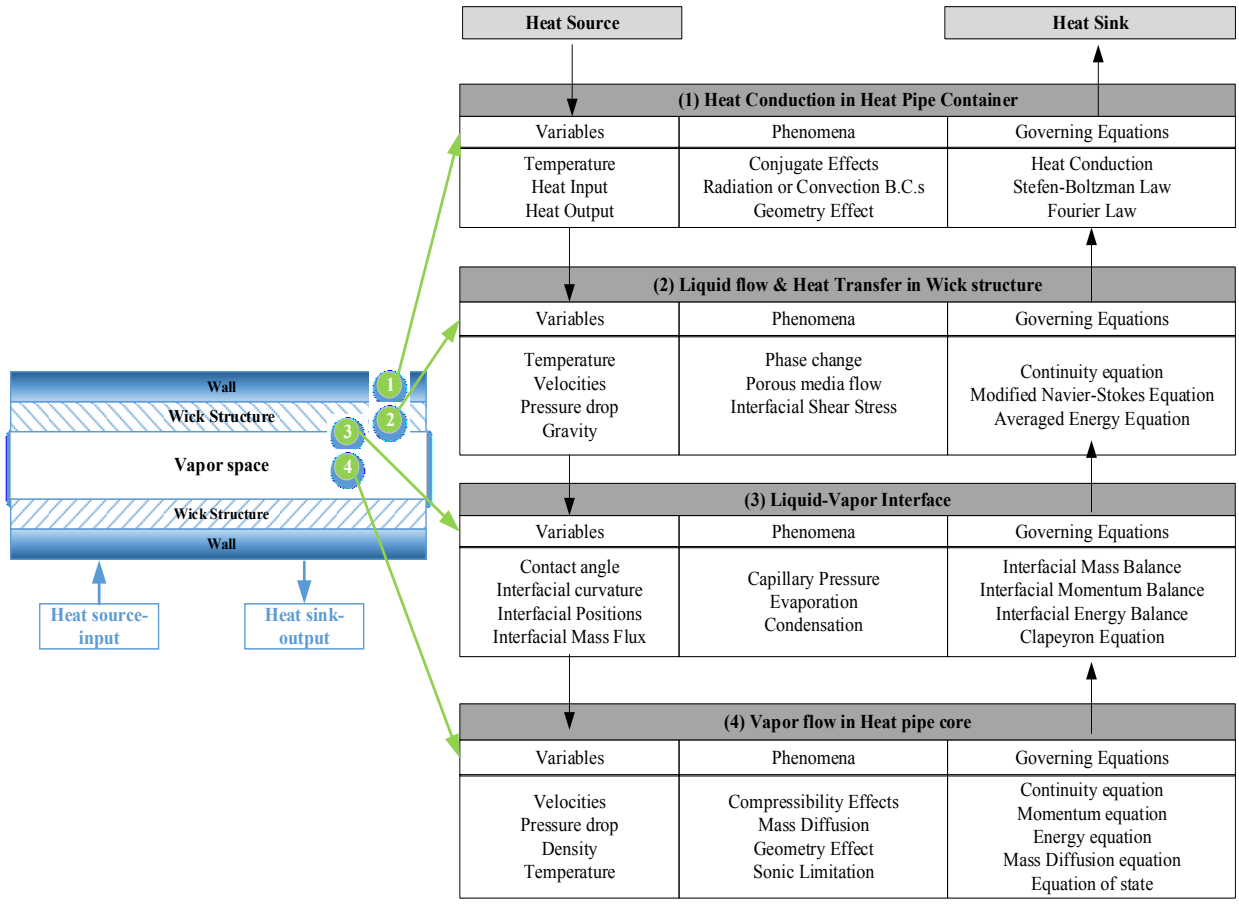

Figure 1-8: Flow chart of heat pipe operation and interaction between different regions- adapted figure from- [1]

Heat pipe components and idealized thermodynamic cycle of operation are depicted in Figure 1-9-a. A quantity of heat Q_{in} is applied to evaporator section. Under steady state, the same quantity of heat is rejected at the condenser. The work, enclosed surface in T-S diagram, is generated inside of heat pipe and used to compensate losses in system and draw liquid back to the evaporator section.

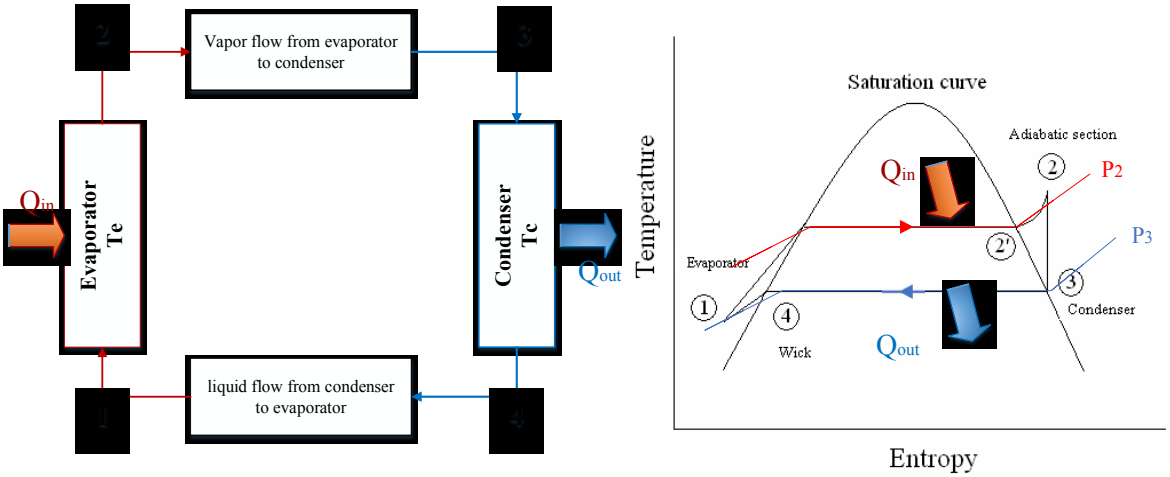

Figure 1-9: a) Various components of heat pipe- b) Temperature-Entropy diagram in thermodynamic cycle of heat pipe - adapted figure from- [1]

According to Figure 1-9-b, the fluid enters the evaporator as a compressed liquid at T1 and receives heat. Then, it leaves evaporator at point 2 or 2' as superheated or saturated vapor. Due to the pressure difference between the evaporator and the condenser (P_2>P_3), the vapor flows to condenser section in path 2-3 or 2'-3. Then, the vapor enters the condenser as saturated vapor and loses its latent heat. Next, it enters adiabatic section as saturated liquid (point 4). Finally, the liquid leaves the adiabatic section to enter evaporator as a compressed liquid and completes cycle (point 1). If one considers the heat pipe as thermal circuit, a different thermal resistance can be defined for each section as shown in Figure 1-10.

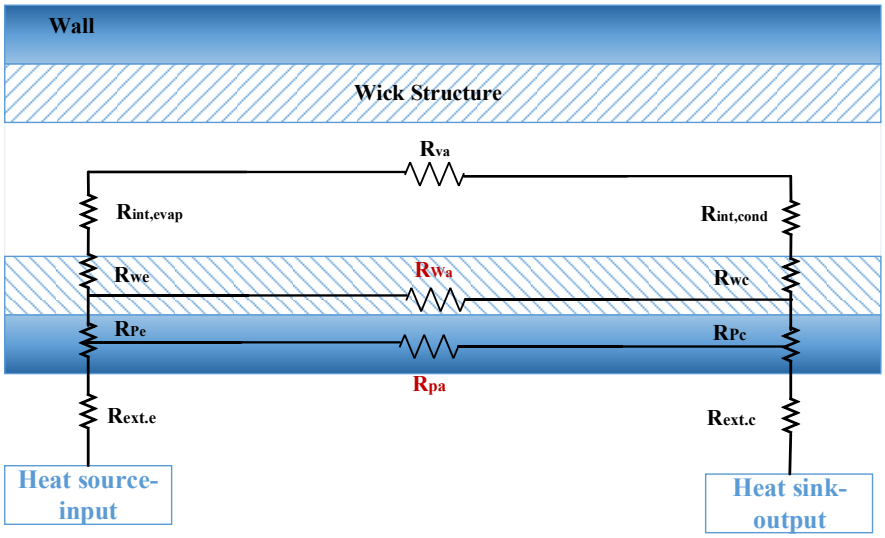

Figure 1-10: Thermal resistance across a horizontal heat pipe- adapted figure from [6]

The total thermal resistance includes all single heat resistances where R_p and R_w represent the radial conduction in the wall region and wick structure (respectively in evaporator zone and condenser zone). R_{ext} stands for the convection resistance between the external flow and wall, and R_{va}, R_{pa} and R_{wa} represent the axial conduction through the vapor, wall and liquid in the wick structure, respectively. $R_{int,evap}$ and $R_{int,cond}$ are interfacial resistance between liquid and vapor related to boiling and condensation. Comparing the orders of the thermal resistances, some of the parallel and serial resistances in the circuit like R_{wa}, R_{pa} can be neglected (see TABLE 1-1). Also, the convection caused by the external flow adds more complexity to the system since a conjugated heat transfer problem need to be solved. By neglecting the wick structure and assuming a constant heat flux at wall, the main thermal resistances in the heat pipe circuit are related to R_{va}, R_{pe}, R_{pc}, $R_{int.evap}$ and $R_{int,c}$ [6].

$$R_{total} = R_{\text{int}.evap} + R_{pe} + R_{\text{int.cond}} + R_{pc} + R_{va} \qquad (1.3)$$

TABLE 1-1: Thermal resistance model in heat pipe and their order of magnitude [6]

Resistance	Order of Magnitude (K/W)
Rw.a→ axial resistance on wick structure	10^{4}
Rp.a→ axial resistance of the pipe wall	10^{2}
Rv.a→ axial resistance of vapor	10^{-8}
Rwe, Rw.c → radial resistance of liquid in wick structure (evaporator or condenser)	10^{+1}
Rp.c, Rp.e → radial resistance of the pipe wall at the evaporator or condenser	10^{-1}
Rint.evap,cond→ liquid-phase interface radial resistance	10^{-5}

1.6 Heat pipe performance

The performance of the heat pipe is typically estimated from the heat transfer coefficient, thermal resistance and pressure drop. In most published works ([7] and [8]), the thermal resistance is defined as the key characteristic of heat pipe performance. The equivalent thermal resistance is characterized by the temperature difference between the evaporator and condenser divided by the power of evaporator or condenser. The equivalent thermal resistance is calculated with the following equation:

$$R_{equiv} = \frac{(T_{evap-wall} - T_{cond-wall})}{Po_{evap} = Po_{cond}} \rightarrow R_{equiv} = \frac{1}{(\pi DL_{evap} + \pi DL_{cond})h_{equiv}} \quad (1.4)$$

Beside the equivalent thermal resistance, one can define the thermal resistance of the evaporator and condenser, individually.

$$R_{evap} = \frac{(T_{evap-wall} - T_{sat})}{Po_{evap}}$$
$$R_{cond} = \frac{(T_{sat} - T_{cond-wall})}{Po_{cond}} \quad (1.5)$$

1.7 Research project description

This project deals with a heat transfer analysis and optimizing of a heat pipe used in industrial ventilation systems with the help of a numerical model and experimental prototype. The model represents the lab-prototype, which is a smooth U-type pipe half-filled with refrigerant, without any wick structure. The convection on the external surface of the heat pipe is neglected. As mentioned in the previous section, it adds a lot of complexity to the analysis. Additionally, the assumption of assuming a constant heat flux at boundary is acceptable. Therefore, in analysis of heat transfer for a heat pipe, only the inside part is considered.

The heat transfer inside a heat pipe can be divided in different regimes. When the liquid is subcooled, the heat transfer is governed by single-phase forced convection. When heat is increased however, boiling will start in cavities or nucleation sites at the heated walls. The generated bubbles will grow and then detach when a critical size is reached. In the condenser, the saturated vapor in contact with the wall below saturation temperature will condense and thus release its latent heat of vaporization. Comparing to heat conduction in wall and natural convection in the vapor core, the biggest portion of heat transfer is devoted to boiling and condensation. Therefore, an appropriate modeling of the phase changes process is the key step for the study heat transfer in heat pipes.

The first part of this work is the simulation of the bubble nucleation in the evaporation section, which strictly affects the heat transfer rate. There are various works including numerical and experimental that have been done to study boiling phenomena, such as [9] & [10]. The work of these authors became references for the implementation of the boiling model into the commercial software and in OpenFOAM. On the other hand, only a few investigations are

published on developing prediction models for condensation phenomena. Therefore, the first object of this PhD thesis is proposing a numerical model compatible with the boiling model (available in OpenFOAM solver) for the simulation of the condensation inside a pipe. After developing an acceptable condensation model, the next step is to simulate a complete heat pipe including an evaporator and condenser working simultaneously. The complexity is important due to the combination of the boiling and condensation models that strongly interact. This challenge becomes even more severe when the system is a closed one, inside which the variation of pressure affect the solution of the equations, drastically. After having validated the numerical model, the thermal resistance is defined as a main characteristic for heat pipe and some sensitivity analysis are performed to seek under which conditions the heat pipe has better performances.

As a part of the project, a heat pipe prototype has been built-up to validate the numerical model with experimental data (Figure 1-11). This physical model is based on a real industrial heat pipe used at Venmar Inc. for large ventilation systems. In this prototype, the working fluid is R-134a and the pipe material is aluminum alloy, the same material as used in the industrial application. This model and its specification will be described in Chapter 5.

Figure 1-11: Prototype of heat pipe build in chemical engineering laboratory in UdeS

1.8 Objectives

The main purposes of the present PhD project are:

- Develop a new model compatible with the OpenFOAM solver to simulate heat transfer during condensation.
- Combine boiling and condensation models to represent the behaviour of a heat pipe.
- Design, fabricate and perform experimental tests on a setup at UdeS to study the operation of scaled down heat pipe representative of the industrial one.
- Validate the numerical model with experimental data obtained from the tests.
- Investigate the effect of independent parameters on the heat pipe performance and propose an optimized prototype aiming a higher thermal efficiency for the industrial ventilation systems.
- Design two-groove structures for heat pipe and analyze their performance to seek which geometry has better performance.

1.9 Study plan

Although, there are many experimental works to study the heat pipe behaviour, only a few investigations are presented on the development of numerical models. With the help of such models, the influence of important variables such as velocity, pressure, temperature and phase fraction[1] of each phase can be separately observed. Some models that can be applied for boiling and condensation are available in commercial software. Typically, the implemented models take into account the interfacial heat transfer between two phases, in the bulk of the working fluid. However, the wall heat flux, which is one of the most important term, can only be represented with simplified boundary conditions like constant temperature or convection conditions. Thus, such a simplified representation of boiling and condensation at the wall can merely approximate these complex phenomena. Therefore, a numerical approach that generates precise solutions with respect to experimental results is proposed in this work.

[1] Phase fraction: volume ratio of vapor to total volume

In the next chapter, the state of the art, the concept of boiling and condensation are reviewed, then, some relations for prediction of heat transfer coefficients for boiling and condensation in different regimes are introduced, which are divided into four main regimes: pool boiling, flow boiling, pool condensation and flow condensation. Finally, the phase change modeling and governing equations are presented.

The numerical solution is obtained through using an open source tool, OpenFOAM, written in C++ and run on Linux systems. The boiling model is already available and validated. However, its concept is comprehensively reviewed in chapter 3 in order to have a better comprehension of phase change model. Some part of this concept is repeated in chapter 4 and 5. Borrowing the idea of boiling model, a new model for simulation of condensation is suggested. The model is introduced in chapter 4 with the related results that have been published in International Journal of Heat and Mass Transfer [11].

After the validation of condensation, both boiling and condensation models are used to simulate the behaviour of a complete heat pipe, as shown in chapter 5. Important difficulties arise when both phenomena work simultaneously in a closed system. The critical point at this stage is the variation of flow parameters like pressure. After having validated the numerical model, some sensitivity analysis on the numerical model are performed to seek the effects of independent parameters on heat pipe function and to propose an optimum prototype. The results of this work have also been published in International Journal of Heat and Mass Transfer [12].

Two designs of grooves inside the heat pipe are proposed and built based on sensitivity analysis conducted with the numerical model and based on literature works. In chapter 6, the improvement of the heat pipe performance in the presence of new groove structure are empirically investigated and the results are compared with the performance of smooth heat pipe described in chapter 5.

Finally, the conclusions of the present work and suggestions for future works are presented in chapter 7.

1.10 Methodology

In order to generate a numerical model representing a two-phase flow in a closed system, a Computational Fluid Dynamics (CFD) methodology is used in this study. The mathematical

model is based on conservation equations of Navier-Stokes. PISO[2], SIMPLE[3] and PIMPLE (combination of PISO and SIMPLE) algorithms are applied in OpenFOAM for the pressure-velocity coupling and to prevent checker-board instability. The solver developed for turbulent flow is selected to calculate turbulent terms generated by chaotic behaviour of bubbles. As shown in TABLE 1-2, there are numerous solvers available for simulation of multiphase flow in OpenFOAM .

TABLE 1-2: Some available solvers in OpenFOAM to model phase changes

Solver name	Description	Method
InterFoam	Laminar, two incompressible flows, isothermal immiscible fluids	VoF, phase-fraction based interface capturing approach, PISO algorithm
twoPhaseEulerFoam	heat transfer, laminar/turbulent, compressible fluid phases with one phase dispersed, e.g. gas bubbles in liquid	Two-Fluid method, PIMPLE algorithm
compressibleInterFoam	compressible, non-isothermal immiscible fluids	using a VoF (volume of fluid) phase-fraction based interface capturing approach
reactingTwoPhaseEulerFoam	system of many compressible fluid, including heat transfer, laminar/turbulent	Two-Fluid method, PIMPLE algorithm, phase change modeling boiling, convection of two phases

The best and most appropriate solver that fits to our problem for modeling the phase change and the interaction between the two phases is the "*reactingtwoPhaseEulerFoam"*. This solver is enthalpy-based and uses an Euler-Eulerian approach in which each phase is considered as a continuous phase. It means that the boundary conditions are applied for each phase separately and each variable such as velocity, pressure, temperature, and phase fraction is considered for both phases.

The structure of the OpenFOAM code consists of three parts: pre-processing, solver and post-processing (Figure 1-12). In pre-processing tool, user need to define the geometry, mesh, fluid

[2] Pressure Implicit with Splitting of Operator
[3] Semi-Implicit Method for Pressure Linked Equations

properties, initial values and boundary conditions. In the solver tool, the governing equations are discretized while in the post-processing tool, results of the solution can be visualized (using tool like Paraview). One of OpenFOAM benefits is that user can add or modify governing equations and extend existing solvers to new needs.

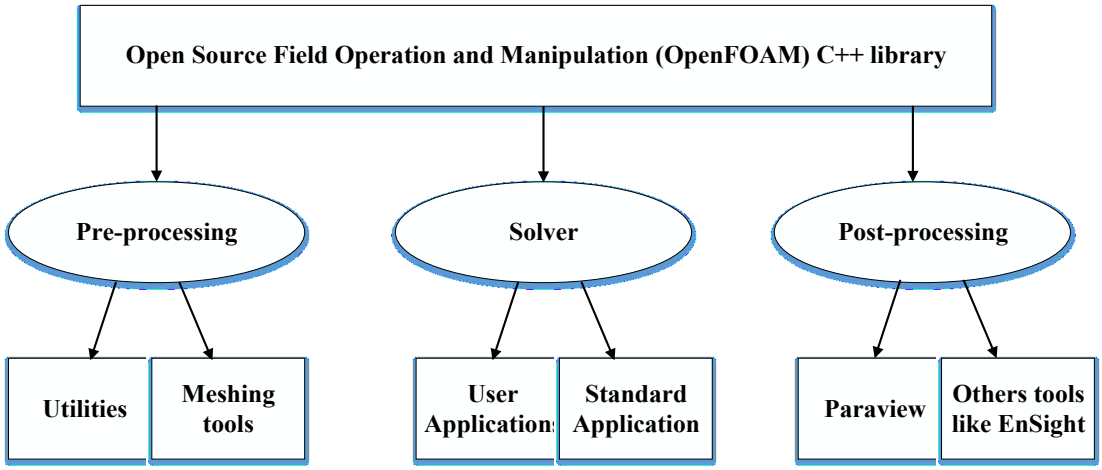

Figure 1-12: Structure of code in OpenFOAM- [13]

This PhD project is focussed on the optimization of a heat pipe prototype by using a mathematical model validated with experimental data. Since the boiling model is already available in OpenFOAM, there are three main steps to reach final purpose.

- Initial model: First, condensation inside a 3-D channel is separately considered, without the wall region (as shown in Figure 1-13). The nearest existent OpenFOAM solver for modeling phase change is chosen. Wall heat flux and mass generation terms are then added to the general equation. This model is validated by comparing the numerical predictions with experimental data found in open literature.

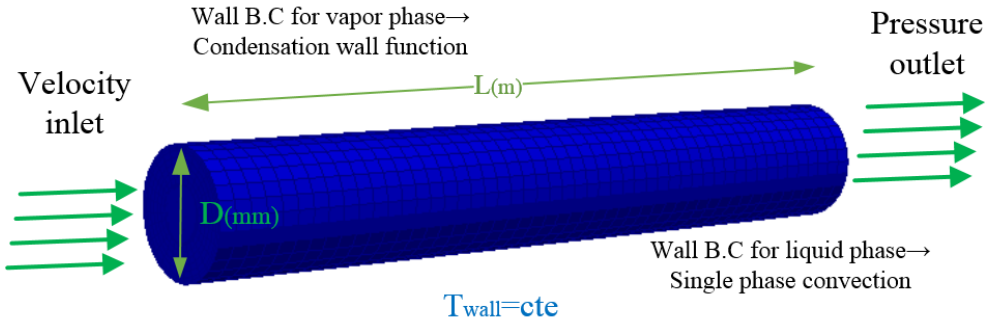

Figure 1-13: Simulation of flow condensation in 3-D cylindrical channel

- Second model: After the validation of the condensation model, boiling and condensation models are combined into a complete model of heat pipe, which is a U-type smooth channel with a circular cross section and filling ratio of 50% (as shown in Figure 1-14). The experimental data obtained from the tests is used to validate suggested model in OpenFOAM.

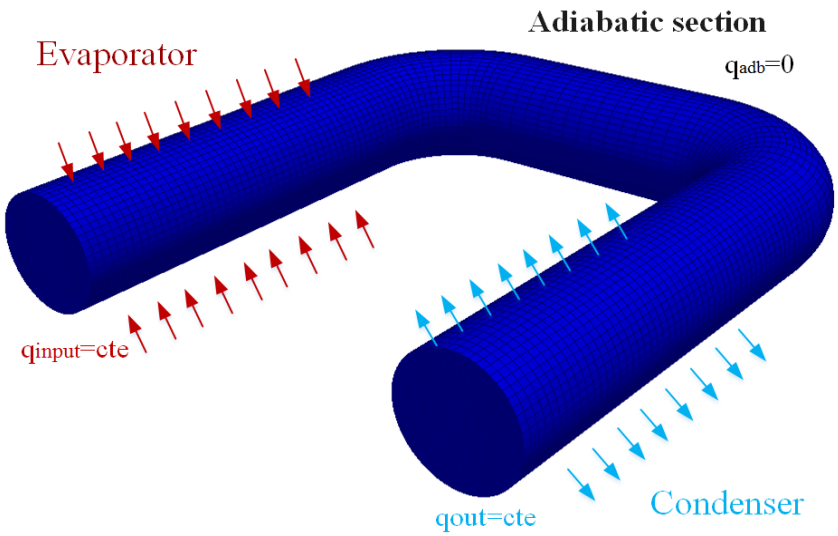

Figure 1-14: Complete model of U-type smooth heat pipe

- Optimized model: After having validated the numerical model, some numerical sensitivity analysis are performed to investigate the effect of independent parameters like size of the tube, applied heat, external mass flow rate of water, type of refrigerant and filling ratio on the heat pipe performance, which can be characterized by its thermal resistance.

2 CHAPTER TWO: State of the art

2.1 Phase change concepts

In this section, the concepts of boiling and condensation are briefly reviewed then some correlations for the calculation of heat transfer coefficients are introduced as found in literatures.

2.1.1 Boiling concepts

Boiling happens when at specific pressure, the temperature of a liquid becomes greater than its saturation temperature T_{sat} and bubbles are then generated. The important parameters in boiling are the latent heat of vaporization h_{lv}, the surface tension at the liquid-vapor interface and the thermal properties of the fluid like its thermal conductivity, specific heat, density and viscosity. At the boiling point, the thermal equilibrium is perturbed and bubbles are not in thermodynamic equilibrium with the surrounding liquid. The pressure difference between liquid and vapor is balanced by the surface tension at the interface (Young-Laplace equation). In addition, the temperature difference between newly created bubble and surrounding liquid is the driving force for heat transfer between the two phases. There are two categories of boiling: (a) pool boiling and (b) flow boiling also called forced convection boiling.

2.1.1.1 Pool boiling

Pool boiling is a stationary flow while bubbles grow and rise due to buoyancy effects. Pool boiling consists of four primary regimes: (a) natural convection boiling (no bubbles generated), (b) nucleate boiling (bubbles rise and grow), (c) transition boiling and (d) film boiling [14]. They are briefly explained in the following as presented in Figure 2-1:

- **Natural convection boiling (A→B)**: It looks like evaporation when the liquid temperature is higher than its saturation temperature ($\Delta T_{sup}=T_l-T_{sat}$ is about between 2 ^{o}C and 5 ^{o}C). The liquid is superheated and evaporates when it rises to free surface.
- **Nucleation boiling (B→D)**: Bubbles form but collapse and dissipate into the liquid rapidly (subcooled boiling region). The stirring and agitation caused by the entrainment of liquid to the heater surface is responsible for increasing the local heat transfer coefficient. Bubbles can grow and rise to the free surface making numerous continuous columns of vapor (saturated boiling region). At this point, the heat transfer coefficient is tremendously

increased by effect of the liquid entrainment and evaporation. The maximum heat transfer coefficient occurs where the heated surface is covered by bubble, *(*ΔT is between 5 °C and 30 °C).

- **Transition boiling (D→E)**: The heated surface is covered by a vapor film, which acts as a thermal insulator. Due to the low thermal conductivity of vapor relative to liquid, the heat transfer suddenly drops. In reality, boiling cannot follow the transition part of the boiling curve unless applied power is reduced (ΔT is between 30 °C to 120 °C).
- **Film boiling (E→F)**: after a drop of the heat transfer coefficient at the end of the transition regime, the radiation of vapor, which is significant at high temperature, causes the heat transfer to rise again (ΔT is between 120 °C and 1000 °C).

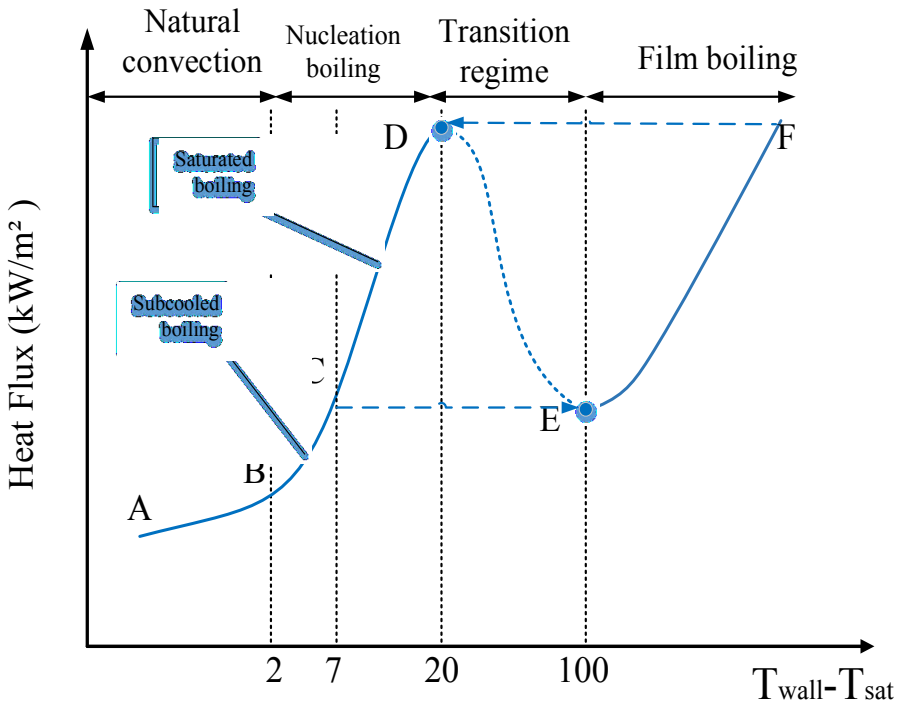

Figure 2-1: Boiling curve, heat flux vs superheat temperature- adapted figure from [15], [9]

The natural convection and nucleation boiling are two main practical regimes that are mostly observed in applications. There are various models in the literature for the prediction of pool boiling in different regimes as mentioned in following table.

TABLE 2-1: Proposed correlation for pool boiling regime

Reference	Model	Regime
Cooper (1984) [16]	$h = 1.7 \times 55 P_r^{(0.12-0.2 Log C_{sf})} (-\log P_r)^{-0.55} \bar{M}^{-0.5} \times q_{wall}^{0.67}$ $P_r = P_{sat} / P_{crt}, \bar{M} = 102.03 (for \quad R134a)$	General
Ribatski et Jobardo (2009)[17]	$h = 100 \times P_r^{(0.45)} (-\log P_r)^{-0.8} \bar{M}^{-0.5} \mathrm{Re}_a^{0.2} \times q_{wall}^{(0.9-0.3 P_r^{0.3})}$	Nucleation boiling
Jung (2003) [18]	$Nu = \frac{hD}{\lambda_l} = 10 (\frac{q_{wall} \phi}{A \lambda_l T_{sat}})^{c_1} (1 - T_r)^{-1.4} \mathrm{Pr}_l^{-0.25}$ $\phi = 0.0146 \sqrt{2\sigma / g(\rho_l - \rho_v)}, \quad T_r = T_{sat} / T_{crt}$ $c_1 = 0.855 (\frac{\rho_v}{\rho_l})^{0.309} \mathrm{Pr}^{-0.437}$	Nucleation boiling
Rohsenow (1962)[15]	$q_{wall} = \mu_l h_{lv} [\frac{g(\rho_l - \rho_v)}{\sigma}]^{0.5} [\frac{Cp_v (T_{wall} - T_{sat})}{C_{sf} h_{lv} \mathrm{Pr}_l^{1.0}}]^3$	Nucleation boiling
Stephan and Abdelsalam (1980) [19]	$Nu = \frac{hD}{\lambda_l} = 0.0546 [(\frac{\rho_v}{\rho_l})^{0.5} \frac{q_{wall} d_w}{\lambda_l T_{sat}}]^{0.67} [\frac{h_{lv} d_w}{a_L^2}]^{0.248} [\frac{\rho_l - \rho_v}{\rho_l}]^{-4.33}$ $a_L = \text{experimental parameter}$	Nucleation boiling
Bromley (1950)[15]	$q_{wall} = 0.62 [\frac{g \lambda_l^3 \rho_v (\rho_l - \rho_v)[h_{lv} + 0.4 Cp_v (T_{wall} - T_{sat})]}{\mu_v D (T_{wall} - T_{sat})}]^{0.25} (T_{wall} - T_{sat})$	Film boiling

2.1.1.2 Flow boiling

Flow boiling combines pool boiling with flow convection and is classified into two categories: internal flow and external flow. External flow is similar to pool boiling with additional heat flux due to flow motion. However, in internal flow, vapor and liquid are forced to move together and there is no path for vapor to escape to free surface. Forced convection boiling is commonly referred to as two-phase flow and characterized by rapid changes from liquid to vapor in the flow direction (Figure 2-2).

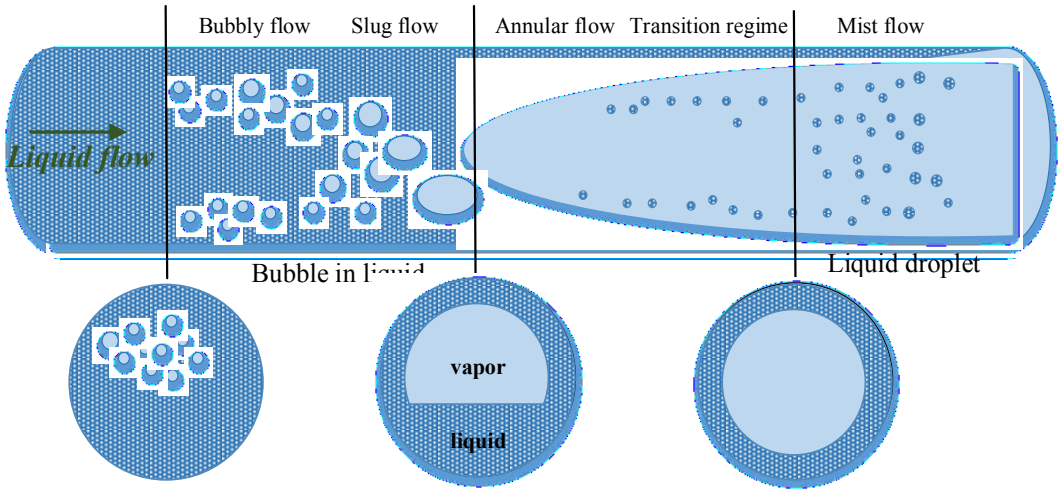

Figure 2-2: Flow boiling regime from stratified to annular regime- adapted figure from [9]

Internal flow regimes can be divided into bubbly, slug, annular, transition and mist flow [20]. In bubbly flow, the bubbles grow and rise from the heated surface. Along the tube, bubble grow in size and eventually coalesce into slug of vapor. Up to half of the volume of the tube can be occupied by the vapor. Later along the tube, an annular flow can be reached and characterized by a liquid that is confined on the walls while the core of the tube is filled with vapor. Such a situation leads to an increase of the heat transfer coefficient. When the annular liquid layer gets thinner, dry spots appear on the surface and decrease the heat transfer because there is no liquid locally; this is transition flow. In the last flow regime, the surface is dried and liquid droplets are suspended in the vapor core until it is vanished; this is the mist flow regime (Figure 2-2). The appearance of dry spots is accompanied by a sharp decrease in the heat transfer coefficient [14]. As described in following table, there are some available correlations in the open literatures for the determination of heat transfer coefficient of flow boiling.

TABLE 2-2: Proposed correlation for flow boiling regime

Reference	Model	Regime
Shah (1983) [21]	$h = h_l(230 \times Bo^{0.5} + \frac{T_{wall} - T_{sat}}{T_{sat} - T_l})$ $h_l = 0.023 \frac{\lambda_l}{D}(\frac{GD}{\mu})^{0.8} \mathrm{Pr}^{0.4}, Bo = \frac{q_{wall}}{Gh_{lv}}$	General

Phase change concepts

Wojtan et al. (2006) [22]	$q_{wall} = 0.437(\frac{\rho_v}{\rho_l})^{0.073} We_{lo}^{-0.24} Gh_{lv} (\frac{L}{D})^{-0.72}$ $We_{lo} = \frac{G^2 D}{\rho\sigma}$	General
Zhang et al. (2006) [23]	$q_{wall} = 0.0352[\mathrm{We}_{lo} + 0.0119(\frac{L}{D})^{2.31}(\frac{\rho_v}{\rho_l})^{0.361}]^{-0.295}(\frac{L}{D})^{-0.311}$ $Gh_{lv}[2.05(\frac{\rho_v}{\rho_l})^{0.17} - \mathrm{x}_{in}]$	General
Fang(2013) [24]	$Nu = \frac{hD}{\lambda_l} = \frac{.00061(S+F)\,\mathrm{Re}_l\,\mathrm{Pr}_l^{0.4}(\mathrm{Fa})^{0.11}}{Ln(1.023\mu_{l,f}/\mu_{l,w})}$ $Fa = \frac{(\rho_l - \rho_v)\sigma}{G^2 D}, \quad F = (\frac{x}{1-x})^{0.95}(\frac{\rho_l}{\rho_v})^{0.4}$ $S = \begin{cases} 30000 Bo^{1.13}, & Bo < 0.0026 \\ 36 & Bo \geq 0.0026 \end{cases}, Bo = \frac{q_{wall}}{Gh_{lv}}$	General
Chen (1966)[25]	$h = S.h_{nb} + F.h_{sp}, \quad h_{sp} = 0.023\,\mathrm{Re}_l^{0.8}\,\mathrm{Pr}_l^{0.4}\,\lambda_l/D$ $h_{nb} = 0.00122\{\frac{\lambda_l^{0.79} Cp_l^{0.45} \rho_l^{0.49}}{\sigma^{0.5}\mu_l^{0.29} h_{lv}^{0.24} \rho_v^{0.24}}\}\Delta \mathrm{T}_{sat}^{0.24}\,\Delta P_{sat}^{0.75}$ $S = 1/(1 + 2.53\times10^{-6}\,\mathrm{Re}_l^{1.17}, \mathrm{Re}_l = (1-x)GD/\mu_l$ $F = \begin{cases} 2.35(1/(X_{tt} + 0.213))^{0.736} & 1/X_{tt} > 0.1 \\ 1 & 1/X_{tt} > 0.1 \end{cases}$ $\mathrm{X}_{tt} = (\frac{\rho_v}{\rho_l})^{0.5}(\frac{\mu_v}{\mu_l})^{-0.1}(\frac{1-x}{x})^{0.9}$	Vapor quality between 0.0-0.7
Gungor-Winterton (1987) [26]	$h_{tp} = (SS_2 + FF_2)h_{sp}, S = 1 + 3000(\frac{q_{wall}}{Gh_{lv}})^{0.86}$ $F = 1.12(\frac{x}{1-x})^{0.75}(\frac{\rho_l}{\rho_v})^{0.41}$ $S_2 = \begin{cases} (G^2/gD\rho_l^2)^{(0.1-2(G^2/gD\rho_l^2)} & (G^2/gD\rho_l^2) < 0.05 \\ 1 & otherwise \end{cases}$ $F_2 = \begin{cases} (G^2/gD\rho_l^2)^{(0.5)} & (G^2/gD\rho_l^2) < 0.05 \\ 1 & otherwise \end{cases}$	Both vertical and horizontal flows

Sun-Mishima (2009)[27]	$h = \frac{6\,\mathrm{Re}_{lo}^{1.05}\,Bo^{0.54}}{We_{lo}^{0.191}(\rho_l/\rho_v)^{0.142}}\frac{\lambda_l}{D}$ $We_{lo} = \frac{G^2 D}{\sigma\rho_l}, Bo = \frac{q_{wall}}{Gh_{lv}}, \mathrm{Re}_{lo} = \frac{GD}{\mu_l}$	General –mini channel
Kandlikar (1990)[28]	$h = [0.6683\,\mathrm{Co}^{-0.2}\mathrm{f}(\mathrm{Fr}_{lo}) + 1058Bo^{0.7} \times 1.63](1-\mathrm{x})^{0.8} h_{lo}$ $\mathrm{f}(\mathrm{Fr}_{lo}) = \begin{cases} 1 & \mathrm{Fr}_{lo} \geq 0.4 \\ (25Fr_{lo})^{0.3} & \mathrm{Fr}_{lo} < 0.4 \end{cases}$ $Co = (\frac{1-x}{x})^{0.8}(\frac{\rho_v}{\rho_l})^{0.5}, Fr_{lo} = G^2/gD\rho_l^2$ $h_{lo} = \frac{(f_{lo}/8)(\mathrm{Re}_{lo}-1000)\,\mathrm{Pr}_l(\lambda/\mathrm{D})}{1+12.7(\mathrm{f}_{lo}/8)^{0.5}(\mathrm{Pr}_l^{0.667}-1)}, f_{lo} = [0.79Ln(\mathrm{Re}_{lo}) - 1.64]^{-2}$	Both vertical and horizontal flow-general

Since there is no forced flow and thus only natural convection is dominant inside of heat pipe studied in this thesis, a focus is put on pool boiling regimes, especially nucleation boiling.

2.1.2 Condensation concepts

When the temperature of the vapor is less than T_{sat}, vapor condenses into liquid. The latent heat of vaporization, h_{lv}, is released and transferred through the film to the wall surface. Condensation is divided into two categories: (a) pool condensation, and (b) flow condensation [14].

2.1.2.1 Pool condensation

Pool condensation happens when fluid is stationary and is classified into two regimes: filmwise and dropwise condensation (see Figure 2-3). In filmwise condensation, the liquid droplets wet and cover the whole surface area and create a film layer, which slides down due to the gravity effect. With time, the thickness of this layer which acts a thermal resistance, is increased and the heat transfer rate is thus reduced. Adding as promotor like a chemical coating on the surface, the heat transfer rate can be enhanced and the dropwise regime can be achieved. In dropwise condensation, the small droplets that form at the nucleation sites grow. With time, they coalesce into large droplets, slide down when they reach a certain size and exposing the surface again to vapor. In this case, there is no liquid film that hinders heat transfer. As a result,

the heat transfer coefficients in dropwise condensation can become 10 times larger than that associated to filmwise condensation.

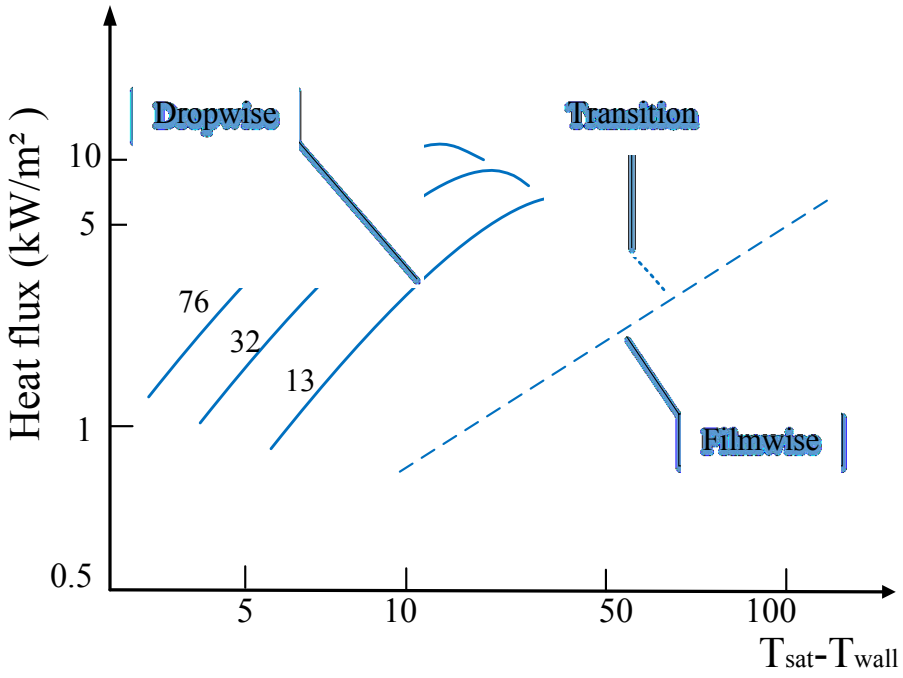

Figure 2-3: Pool condensation regime dropwise and filmwise- adapted figure from [29]

In TABLE 2-3, some proposed relations for the calculation of heat transfer coefficients representing pool condensation are presented.

TABLE 2-3: Proposed correlations for film condensation and dropwise regime

Reference	Model	Regime
Chato (1960) [30]	$h = 0.555[\frac{g\rho_l(\rho_l-\rho_v)\lambda_l^3}{\mu_l(T_{sat}-T_w)D}\{h_{lv}+\frac{3}{8}Cp_l(T_{sat}-T_w)\}]^{0.25}$ $Re_v = \frac{\rho_v U_v D}{\mu_v} < 35000$	Filmwise condensation-inside horizontal tube
Nusselt (1960) [31]	$h = 0.729[\frac{g\rho_l(\rho_l-\rho_v)\lambda_l^3}{\mu_l(T_{sat}-T_w)D}\{h_{lv}+\frac{3}{8}Cp_l(T_{sat}-T_w)\}]^{0.25}$ $Re_l = \frac{\rho_l U_l D}{\mu_l} < 1800$	Filmwise condensation-outside horizontal tube

Cooper P. Griffith (1965) [31]	$h = \begin{cases} 51104 + 2044T_{sat} & 22^{o}C < T_{sat} < 100^{o}C \\ 255310 & T_{sat} > 100^{o}C \end{cases}$	Dropwise condensation steam on copper surface

2.1.2.2 Flow condensation

For flow condensation inside a horizontal tube, gravity and inertial forces are the two primary driving forces influencing the flow regime, which can be classified into four categories: stratified, stratified-wavy, transient and annular regime. In stratified and stratified-wavy flow regime, the gravitational force is more dominant than the inertial force, causes liquid film accumulates at the bottom of tube. The liquid film then acts as a thermal resistance and decreases the heat transfer coefficient. At higher velocities as the flow is entering annular regime, the shear stress forces control the flow, the liquid film thickness is diminished, and the heat transfer coefficient is increased [32]. Other types of flow regime, like slug or mist flow, can be possible but are less frequent than stratified and annular regimes (see Figure 2-4).

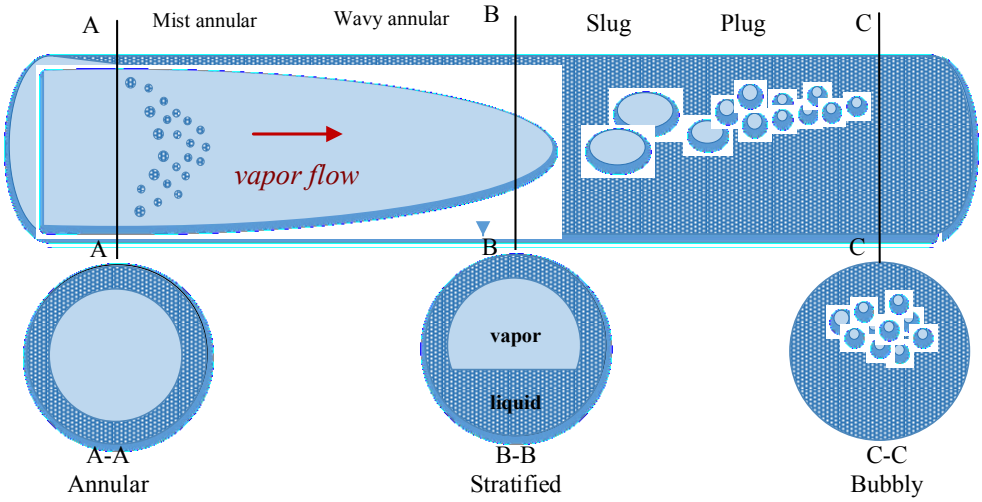

Figure 2-4: Flow condensation regime- adapted figure from [29]

Some suggested correlations for different flow regime of flow condensation is presented in TABLE 2-4.

TABLE 2-4: Proposed correlation for flow condensation regime

Reference	Model	Regime
Shah (1979) [33]	$Nu = \frac{hD}{\lambda_l} = Nu_l[(1-\mathrm{x})^{0.8} + \frac{3.8x^{0.76}(1-x)^{0.04}}{(P_{sat}/P_{cr})^{0.39}}]$ $\mathrm{Nu}_l = 0.023\,\mathrm{Re}_{lo}^{0.8}\,\mathrm{Pr}_l^{0.4}, \mathrm{Re}_{lo} = \frac{GD}{\mu_l}, 10.8 \le G \le 1600(kg/m^2.s)$ $0.2 \le P_{cr} \le 0.53, 7 \le D \le 40mm,\ \mathrm{Re}_{lo} \ge 350$	Annular and stratified flow
Akers at al. (1960) [34]	$G_e = G[(1-\mathrm{x}) + \mathrm{x}\left(\frac{\rho_l}{\rho_v}\right)^{0.5}],\quad \mathrm{Re}_e = \frac{G_e D}{\mu_l}, \mathrm{Nu} = \frac{hD}{\lambda_l} = C\,\mathrm{Re}_e^n\,\mathrm{Pr}_l^{1/3}$ $C = 0.0265,\quad n = 0.8, \text{for}\quad \mathrm{Re}_e > 50000$ $C = 5.03,\quad n = 1/3, \text{for}\quad \mathrm{Re}_e < 50000$	Stratified and annular flow
Dobson and Chato (1998) [35]	$Nu = \frac{hD}{\lambda_l} = 0.023\,\mathrm{Re}_{lo}^{0.8}\,\mathrm{Pr}_l^{0.4}[1 + \frac{2.22}{X_{tt}^{0.89}}]$ $\mathrm{X}_{tt} = (\frac{\rho_v}{\rho_l})^{0.5}(\frac{\mu_v}{\mu_l})^{-0.1}(\frac{1-x}{x})^{0.9},\quad \mathrm{Re}_{lo} = \frac{GD}{\mu_l}$	Stratified flow
Cavallini (1974) [36]	$\mathrm{Re}_{lo} = \frac{G(1-x)\mathrm{D}}{\mu_l}, \mathrm{Re}_{vo} = \frac{G(\mathrm{x})\mathrm{D}}{\mu_v}$ $\mathrm{Re}_{equ} = \mathrm{Re}_{vo}(\frac{\mu_v}{\mu_l})(\frac{\rho_l}{\rho_v})^{0.5} + \mathrm{Re}_{lo}$ $Nu = \frac{hD}{\lambda_l} = 0.05\,\mathrm{Re}_{equ}^{0.8}\,\mathrm{Pr}_l^{0.33},\quad 7000 < \mathrm{Re}_{equ} < 53000$	Annular flow
Travis (1973) [37]	$Nu = \frac{hD}{\lambda_l} = \mathrm{Pr}_l\,\mathrm{Re}_{lo}^{0.9}\frac{F_1}{F_2},\quad F_1 = 0.15[\frac{1}{X_{tt}} + \frac{2.83}{X_{tt}^{0.476}}]$ $\mathrm{F}_2 = 5\,\mathrm{Pr}_l + 5Ln(1 + 5\,\mathrm{Pr}_l) + 2.5\,\mathrm{Ln}(0.00313\,\mathrm{Re}_{lo}^{0.812}), \mathrm{Re}_l > 1125$	Stratified flow

2.2 Numerical, experimental and analytical modeling of heat pipes

In TABLE 2-5, a review of additional related works on heat pipes modeling including numerical, analytical and experimental are briefly presented. Cited works are divided into four main sections: works that are focused on boiling regime individually, investigations on condensation, external flow convection and studies on boiling and condensation coupling when

both are present. Some of the mentioned works will be explained in details in the following sections.

TABLE 2-5: Reference works for modeling heat pipes

Author	Model	Geometry, specifications	Fluid regime
Boiling			
Kandlikar,1991, [38]	Analytical solution	2-D, Horizontal augmented tube (internal fins), open system → evaporator, wick structure	Subcooled nucleate boiling
Michta (2011) [9]	Analytical solution	2-D, open system, evaporator, code developed in OpenFoam	Pool boiling
Ghione (2012) [10]	Analytical solution	2-D, open system, evaporator, code developed in OpenFoam	Pool boiling
Wen-Tao (2015) [39]	Experimental work	R134a, evaporator with different types of grooves, open system	Pool boiling
Tripathi (2015) [40]	Numerical work	3-D channel, open system, R12, using OpenFoam based on model [9] & [10]	Flow boiling
Shademan (2014) [41]	Numerical work	3-D channel, water as working fluid, open system, using OpenFoam based on model [9] & [10]	Flow boiling
Rocha, (2013), [42]	Experimental work	Plain and micro finned tube, open system, evaporator, R134a	Pool boiling
Rooyen, (2013) [43]	Experimental work	Two-enhanced tube, R-134a, R-236fa and R-1234ze(E).	Pool boiling
Yin et al. [44] (2000)	Experimental work	R134 through annular channel, open system, evaporator	Flow boiling
Condensation			
Cavalini et al. (2001) [45]	Numerical and experimental works	Open system, using R22, R134a, R32, R125, R410a and R407c, horizontal tube, propose new correlation for heat transfer coefficient	Flow condensation
Suliman et al. (2009) [46]	Numerical and experimental works	Smooth horizontal tube, using R134a, open system, propose new correlation for heat transfer coefficient	Flow condensation

Hossain et al. (2012) [47]	Experimental work	Smooth horizontal tube, using R22, R1234ze and R410a, open system	Flow condensation
Panitapu (2015) [48]	Experimental work	Open system, comparing experimental with existing correlations	Flow condensation
Bassi, (2003)[49]	Experimental	Smooth tube, open system, condenser using R134a	Pool condensation
External flow convection			
Brahim [50] (2014)	Numerical model	2-D, 10 cylindrical heat pipes, heat transfer of exterior surface, OpenFOAM	Steady state, laminar, incompressible
Coupling boiling and condensation			
Naresh (2018) [7]	Numerical and experimental works	R134a, acetone and water, added fins on condenser, closed system	Thermosyphons
Fadhl et al. (2013) [51]	Numerical and experimental works	Using VOF in Fluent, 2-D model	Thermosyphons
Naresh et al. (2018) [52]	Experimental work	Horizontal wickless heat pipe, using self-rewetting fluid as working fluid, closed system	heat pipe, combing boiling and condensation
Mahdavi et al. (2018) [8]	Experimental and numerical works	Cylindrical copper heat pipe, water as working fluid, CFD model in ANSYS, closed system	Heat pipe with different inclination angle
Abadi et al. (2018) [53]	Numerical model	3-D model developed in FLUENT, conjugated heat transfer problem, R134a and water	Submerged tube → flow condensation Water pool → pool boiling
Wang (2014) [54]	Experimental work	Comparing performance of U-type and L-type heat pipe, closed system	Horizontal heat pipe
Khalili et al. (2015) [55]	Experimental work	Water as working fluid, different geometry of wick structure, helical grooves, closed system	Horizontal heat pipe
Coberan et al. (1998) [56]	Numerical model	R134a plate finned tube heat exchanger, model outflow using natural convection, compare *h* and pressure drop with existing correlations, open system	Plate finned tube, evaporator and condenser separately
Marengo et al. (2009) [57]	Numerical model	Using openFOAM and lumped equation based on Faghri [3] model	Rotating heat pipe

- Closed system means that the whole system is sealed and there is no inlet and outlet, open system means that there is a flow stream with an outlet and an inlet.

2.3 Modeling phase change

In two-phase flow simulation, one phase is called dispersed and the other one is considered as the continuous phase. For example, in evaporation, the vapor is the dispersed phase because the volume fraction is small compared to the liquid one. On the other hand, when condensation is studied, the liquid is the dispersed phase because its volume fraction is small. At the interface of each phase, a thin region exists that is referred to as "*free-surface*" [58].

There are three methods for modeling multi-phase flow: Direct numerical simulation (DNS), Euler-Lagrangian or Disperse Phase Element (DPE) method and Euler-Eulerian or Two-Fluid method.

1) **Direct numerical simulation** (**DNS)**: only Navier-Stokes equations are employed and the interface topology between the two phases is determined as a part of the solution (in macroscopic level). This method needs high-resolution mesh and depends on size of dispersed phase or fluid motion. The basic approach of this method consists of modeling the interface between the two phases. It can be subdivided into three methods: surface-tracking, moving mesh and volume tracking method (VoF) (see Figure 2-5). In surface tracking and moving mesh methods, it is necessary to re-mesh and even move the mesh to capture the changes in the position of the interface, which adds complexity to the solution. However, it is possible to estimate the exact position of the interfaces between phases [58]. In volume tracking methods, an indicator like phase fraction is used to represent the interfaces between two phases. However, it causes some troubles in bounding phase fraction between zero and one. In addition, the exact position of interface is unknown and the estimation of surface tension in Navier-Stokes Equation is difficult [58].

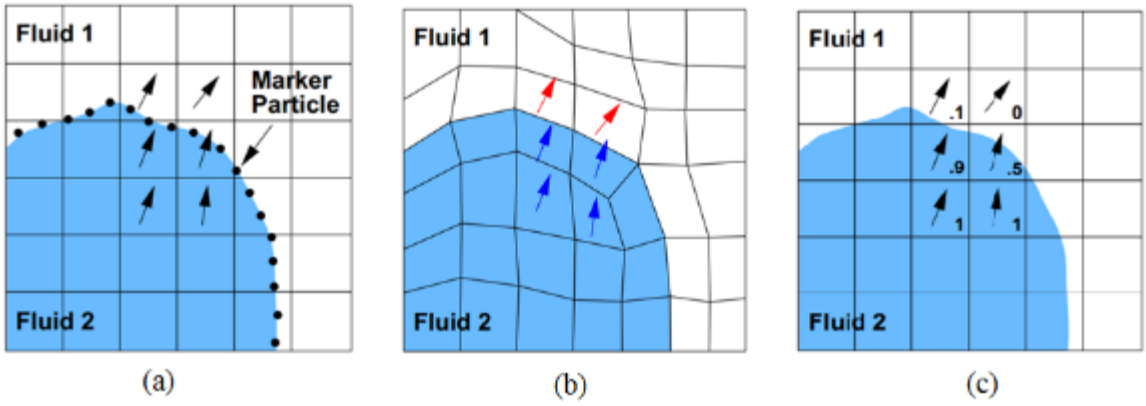

Figure 2-5: (a) Surface-tracking method, (b) moving mesh method (c) volume-tracking method -[58]

2) **Euler-Lagrangian Method or Dispersed Phase Element (DPE) model**: this method is suitable for low phase fraction flow (<0.1). A macroscopic description of the dispersed phase is replaced by microscopic conservation equations. Dispersed flow is tracked by individual DPE momentum equation in the Lagrangian form. But, for the continuous phase, the conservation equations in the Eulerian frame is used where the fluid properties are considered as functions of space and time in an absolute frame of reference. Because combination of the two approaches, the DPE model is called the Euler-Lagrange model [58]. (Figure 2-6).

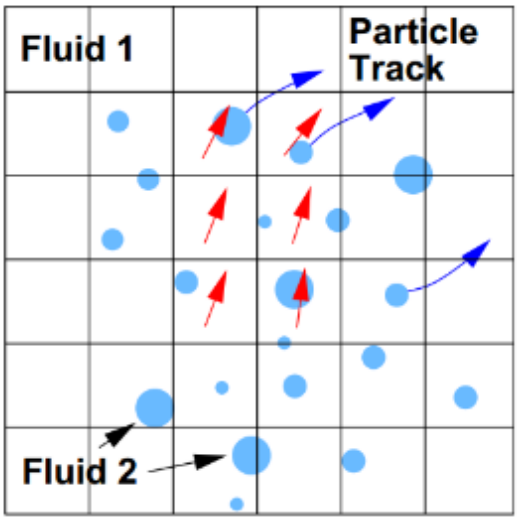

Figure 2-6: Averaged modelling approaches for two-phase flow → (Euler-Lagrange) model-[58]

In this method, an exact and accurate solution is obtained because the properties of the dispersed phase such as size, shape, velocity, heat and mass transfer are separately stored

for each DPE. Nevertheless, if the phase fraction is high, the number of equations needed increases which causes high computation costs.

3) **Euler-Euler method or Two-Fluid method**: This last approach is suitable for all regimes from dispersed to intermediate regime (from low to high phase fraction value). It considers two continuous phases and an Eulerian equation is applied for both phases. An additional parameter, the phase fraction, is used in the conservation equations to distinct phase change characteristics (Figure 2-7). Additional terms that represent momentum and energy exchanges between two phases are also added to the conservation equation.

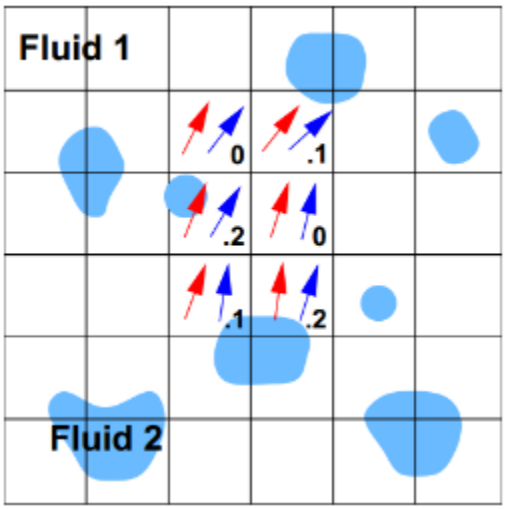

Figure 2-7: Averaged modeling approaches for two-phase flow→Two-Fluid (Euler-Euler) model-[58]

In this model, it is not possible to calculate size, shape and properties of dispersed flow due to the averaging methodology and the omission of extra terms. It should be mentioned that the calculation of the dispersed phase size is important because the interphase transport phenomena depend on that critical parameter [58].

2.3.1 Advantages of Two-Fluid model

In this project, the Two-Fluid model is adapted to simulate the phase change between liquid and vapor. Each phase acts as a separated fluid, with its own set of governing equations. In other words, each phase has its own density, velocity and temperature. However, in most of two-phase model, a unique pressure for both phases is considered. In reality, the two phases can have two different pressures but for simplicity of model, it is necessary to make some

assumption like having locally the same pressure for vapor and liquid and also considering the thermodynamic equilibrium between the phases.

Generally, the advantages of Two-Fluid model are:

- It is suitable to model a wide range of flow regimes where a high phase fraction exists.
- Each phase has its own characteristics like velocity, temperature etc.
- Convergence problems are experienced with the Lagrangian approach when particle loading is high, a situation that is not seen with the Eulerian approach.
- The main advantage of Two-Fluid model is its ability in simulating the turbulent mixing process of the particles. It means that this model is capable of modeling turbulent regime in each phase [59].

Beside the advantages of this method, it has some weak points like its complexity and its high computational cost and effort. Each phase has its own conservative governing equations; its interfacial effects and phase fraction also need to be added to these equations. Another problem is that it does not predict the size of the dispersed phase.

2.3.2 Governing equations of Two-Fluid Model

In Two-Fluid method, each phase is considered as a continuous phase and the governing equations including continuity, momentum and energy are separately solved for each phase. The continuity equation is re-written in the following form:

$$\frac{\partial \rho_a \alpha_a}{\partial t} + \nabla.(\rho_a \alpha_a \vec{U}_a) = \Gamma_{ab} - \Gamma_{ba}^{+} \qquad (2.1)$$

In this equation, α_a is the phase fraction of phase a, ρ_a and $\vec{U}_a$ are the density and velocity of phase a (vapor or liquid). Γ_{ab}^{+} and Γ_{ba}^{+} describe mass transfer due to phase change. If a is the vapor and b the liquid phase, Γ_{ab}^{+} represents the evaporation volumetric source term and Γ_{ba}^{+} is the condensation volumetric source term. One must note that evaporation and condensation cannot physically occur at the exact same location but in numerical solution, it is possible to have a control volume near wall contains two phases in which both condensation of vapor phase and evaporation of liquid happened. This equation is manipulated to satisfy the boundedness of phase fraction [10].

$$\frac{\partial \alpha_a}{\partial t} + \nabla.(\alpha_a \vec{U}) + \nabla.(\alpha_a \alpha_b \vec{U}_r) + (\frac{}{\rho_a}) \frac{^{a}}{Dt} = \frac{\Gamma^{+}_{ab} - \Gamma^{+}_{ba}}{\rho_a} \qquad (2.2)$$

$$\frac{D\rho}{Dt} = \frac{d\rho}{dt} + \rho.\nabla\vec{U}$$

The relative velocity $\vec{U}_r$ and the average velocity $\vec{U}$ are defined as below:

$$\vec{U}_r = \vec{U}_a - \vec{U}_b, \quad \vec{U} = \alpha_a \vec{U}_a + \alpha_b \vec{U}_b, \quad \alpha_a + \alpha_b = 1 \quad (2.3)$$

Similarly, the momentum equation is solved for each phase:

$$\frac{\partial(\rho_a \alpha_a \vec{U}_a)}{\partial t} + \nabla.(\rho_a \alpha_a \vec{U}_a \vec{U}_a) = -\alpha_a \nabla P + \alpha_a \rho_a \vec{g} \quad .[\alpha_a(\tau_a + \tau_a)] + \vec{M}_a + (\Gamma^{+}_{ab}\vec{U}_b - \Gamma^{+}_{ba}\vec{U}_a) \quad (2.4)$$

∇P is gradient of pressure, $(\tau_a + \tau_a^t)$ is the combined laminar and Reynolds stress. The last term $(\Gamma^{+}_{ab}\vec{U}_b - \Gamma^{+}_{ba}\vec{U}_a)$ is added to the momentum equation because of the momentum transfer between the vapor and liquid due to phase changes.

$$\tau_a + \tau_a^t = -\rho_a(\upsilon_a + \upsilon_a^t)[\nabla\vec{U}_a + (\nabla\vec{U}_a)^T] - \frac{2}{3}I(\nabla.\vec{U}_a)] + \frac{2}{3}\rho_a k_a I^t \qquad (2.5)$$

Where I^t is identity matrix, υ^t is the turbulent kinematic viscosity and k^t is kinetic energy of turbulence [9]. If the *k-ε* model is used, two more equations will be added to the governing equations (more explanations in Appendix section 9.2.6). An additional term is added in the momentum equation to represent the interfacial momentum per unit volume, $\vec{M}_a$. This term is generated by the reacting forces between the two phases i.e. dispersed phase and continuous phase. The dispersed phase is subjected to different forces such as drag M_a^d, lift M_a^l, wall lubrication M_a^{wl}, turbulent dispersion M_a^{td} and a virtual mass M_a^{vm} [10].

- The wall lubrication force drives away the dispersed phase from the walls.
- The lift forces push dispersed phase towards walls or centerline depending on the size of the bubble or droplet.
- The turbulent dispersion force related to turbulent fluctuation of continuous velocity and its effects on dispersed phase motion
- The virtual mass comes from relative acceleration of one phase to another phase

- The drag force resists against motion of dispersed phase and depends on the size and relative velocity between the two phases.

The lift, wall lubrication and turbulent dispersion are calculated explicitly and a semi-implicit method is used to evaluate the virtual mass and the drag term. [See Appendix section 9.2.1-9.2.5]

The energy equation for two-phase flow is:

$$\frac{\partial(\rho_a\alpha_a i_a)}{\partial t}+\nabla.(\rho_a\alpha_a i_a \vec{U}_a) = -\nabla.[\alpha_a(\vec{q}_a + \vec{q}_{ta})] + \alpha_a \frac{DP}{Dt}+(\Gamma^+_{ab} i_b - \Gamma^+_{ba} i_a)+Q_i + q''_{wall} A''_{wall} \quad (2.6)$$

Where i_a stands for the specific enthalpy of phase *a*, $\vec{q}_a + \vec{q}_{ta}$ represents the molecular and turbulent heat flux inside phase *a* and $(\Gamma^+_{ab} i_b - \Gamma^+_{ba} i_a)$ is the source term added to the energy equation due to the mass transfer between phases [10]. Q_i is called the interfacial heat transfer between phases and is calculated based on Ranz-Marshall method (additional explanations are found in Appendix 9.3.1). The last term in the energy equation includes A''_{wall}, which is the contact area with the wall per unit volume and q''_{wall} the wall heat flux. This term only appeared at the boundary but plays an important role during the phase change process. Using the Fourier's law of conduction inside phase *a*, the molecular and turbulent heat flux can be transformed into:

$$\vec{q}_a = Cp_a \lambda_a \nabla T_a, \quad \vec{q}_{ta} = Cp_a \frac{\lambda_t}{Pr_t} \nabla T_a \quad (2.7)$$

Where λ, C_p and λ_t are the thermal conductivity, specific heat and turbulent thermal conductivity, respectively. If one assumes *a* is vapor and *b* is in liquid phase, for the calculation of the evaporation volumetric source term, Γ^+_{ab}, which occurs due to nucleation at the heated wall, the following relation is used.

$$\Gamma^+_{ab} = \frac{q''^{e}_{wall}}{h_{lv}} A''_{wall} \quad (2.8)$$

The term q''^{e}_{wall} is called the evaporation heat flux and will be explained in chapter 3. When generated bubble moves inside the bulk of liquid, it is surrounded by subcooled liquid and may

condense in appropriate conditions. The condensation volumetric source term Γ_{ba}^{+} can be calculated following an expression based on Wolfert et al. [9]:

$$\Gamma_{ba}^{+} = \frac{h_{\text{int}}(T_{sat} - T_b)a_{\text{int}}}{h_{lv}} \qquad (2.9)$$

Where a_{int} represents the interfacial area and h_{int} is interfacial heat transfer coefficient for condensation as described by Wolfert et al. [9]. In OpenFOAM, another way is proposed for the calculation of this source term based on the Ranz-Marshall method (see appendix 9.3.2).

The important term in the energy equation, that are main concern of this thesis, is the wall heat flux q''_{wall} which must be precisely calculated for boiling or condensation regimes. This term will be explained in details in chapters 3 and 4.

3 CHAPTER THREE: Boiling Model

3.1 Literature review

There are several studies such as Michta [9], Ghione [10], Tripathi [40] and Shademan [41], have led to the development of Euler-Euler models for the prediction of flow boiling within OpenFOAM platform. In Michta [9] and Ghione [10], a two-phase flow model including subcooled boiling CFD code written in OpenFOAM, is developed and validated. Their work became the reference of other researchers for completing pool and flow boiling models. Their results show that heat transfer is independent of the saturation temperature and of the type of tube. However, the type of refrigerants, heat flux level and geometry all have strong effects on the heat transfer coefficient.

In the experimental work of Rooyen et al. [43], phase change studies were investigated covering different refrigerants such as R134a, R236, R1234, conducted on two types of enhanced-tubes. The tests were performed for saturation temperatures between 5 and 25 ^{o}C and heat fluxes in the range 15-70 kWm^{-2}. They concluded that heat flux and the type of refrigerant have a dominant effect on the heat transfer. Finally, they proposed new correlations for enhanced-tube pool boiling based on prevailing mechanisms in the wall region.

The paper of Rocha [42] presented their experimental work on pool boiling of R134a inside plain and micro-finned tubes at pressures between 6.1 and 12.2 bar and heat flux of 1-100 kW/m^2. They measured the heat transfer coefficient and compared it with correlations of Cooper [16] and Jobrado [17]. They concluded that the correlation of Jobardo is much better for the prediction of the heat transfer coefficient for micro-finned tube. Also, using a micro-finned tube instead of a plain tube can increase the heat transfer rate by about 85%.

The effect of the heat input, inlet mass flux and saturation temperature of R134a on the heat transfer coefficient of subcooled flow boiling were studied by the experimental works of Yin et al. [44]. They concluded that the boiling heat transfer is not affected by the mass flux and saturation temperature. Moreover, they used flow visualization and revealed that at higher heat flux, the wall surface is covered with small bubbles with a higher detachment frequency, but with no change in their size.

3.2 Wall heat flux

In OpenFOAM version 4.0 and newer, a solver called "*reactingTwoPhaseEulerFoam*" existes in which boiling model is already implemented. It is thoroughly described in this section as a background for the next section. However, in chapter 4 and 5, it is partially repeated in order to respect regulation of writing a thesis based on articles. As mentioned before, when applying the energy equation at the boundaries for the boiling or condensation cases, the most important term in the conservation equation is the wall heat flux q''_{wall} that must be correctly modeled. There are several empirical correlations that connect wall heat flux to global parameter like pressure. However, these correlations are not useful in CFD application because they do not give any information about local parameters such evaporation rate or diameter of dispersed phase. Kurul et Podowki [60] suggested that the heat transfer between the heated wall and the liquid originates from three different mechanisms as described below:

$$q''_{wall} = q^{c''}_{wall} + q^{e''}_{wall} + q^{q''}_{wall} \quad (3.1)$$

Where $q^{c''}_{wall}$ represents the single-phase convection, $q^{e''}_{wall}$ is the evaporation flux and $q^{q''}_{wall}$ stands for the quenching heat flux as shown in Figure 3-1. At wall, bubbles are formed at the nucleation sites due to evaporation of liquid representing the part of the wall heat flux that is directly used to transform the liquid into vapor. This heat flux is called evaporation $q^{e''}_{wall}$. When bubbles grow and reach a critical size, they detach from the wall. Then cooler liquid occupy their space and received heat from wall. This heat is related to quenching heat flux $q^{q''}_{wall}$. The rest of wall used for single-phase convection of liquid phase [9].

Wall heat flux

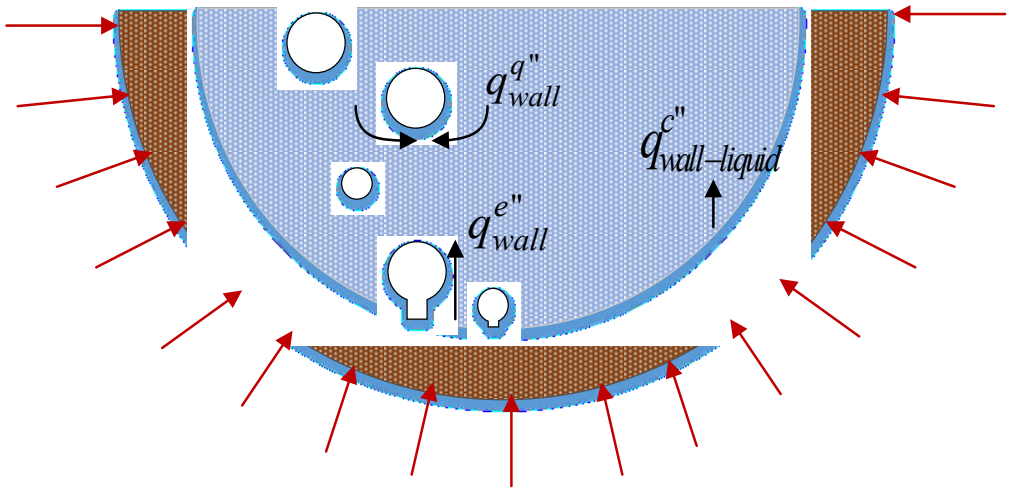

Figure 3-1: Wall boiling model consisting of evaporation, quenching and single-phase convection

The evaporation heat flux is calculated based on key parameters such as density, latent heat of vaporization, velocity of vapor and boiling area fraction A_b.

$$q^{e''}_{wall} = \dot{\imath} \qquad \cdot \qquad ,) \quad (3.2)$$

Where $\dot{\imath}$ and h_{lv} are the mass flux generated by evaporation and the latent heat of vaporization, respectively. $U_{adj.v}$ is the velocity of vapor near the wall, a function of the frequency of detachment f and the diameter of the detached bubble d_w [9].

$$U_{adj.v} = f \times d_w \qquad (3.3)$$

Rohsenow [61] developed a correlation to represent the quenching heat flux as following:

$$q^{q''}_{wall} = A_b \frac{2\lambda_l (T_{wall} - T_l)}{\sqrt{\frac{\pi \lambda_l}{f \rho_l C_{p,l}}}} \qquad (3.4)$$

The single-phase convection heat flux is calculated as:

$$q^{c''}_{wall} = (1 - A_b) H_{c,l} (T_{wall} - T_l) \qquad (3.5)$$

Where $H_{c,l}$ is the Stanton heat transfer coefficient for the single-phase convection of liquid and calculated based on the Stanton number [9]. This coefficient is calculated empirically, based on the liquid Stanton number, $C_{h,l}$, in a similar approach as CFX software:

$$H_{c,l} = C_{h,l}\rho_l Cp_l \left\|\vec{U}_l\right\|, \quad C_{h,l} = \frac{C_f^2}{1-1.783C_f} \quad (3.6)$$

C_f is called Fanning friction factor and is calculated as below:

$$C_f = \frac{1}{Ln(\frac{\tilde{}}{0.435}) + 5.05}, \quad \tilde{} \quad \frac{36\times10^{-4}\left\|U_l^{Bulk}\right\|}{\vartheta_l} \quad (3.7)$$

The following expression of Tolubinsky is used for the calculation of the diameter of detached bubble [62]:

$$d_w = 6\times10^{-4}\times\exp[-\frac{(T_{sat}-T_l)}{45}] \quad (3.8)$$

In the above equations, A_b is a non-dimensional number called the boiling area fraction. It represents the ratio of the wall area wetted by bubbles to the total area. Most known references like [63] and [64] proposed different models for the calculation of the boiling area fraction, and frequency of detachment. In Lemmert [63], the following correlation is suggested for the boiling area fraction as a function of the diameter of the detached bubble and nucleation site density:

$$A_b = \pi d_w^2 \times N'' \quad (3.9)$$

The nucleation site density act as a nest for bubble formation and it mostly depends on the temperature difference between the wall and the saturation temperature. The following correlation of Egorov and Menter [65] is proposed for the estimation of nucleation site density:

$$N'' = 7.937\times10^5[\frac{T_{wall}-T_{sat}}{10}]^{1.805}(m^{-2}) \quad (3.10)$$

The constant numbers in mentioned equations, such as *7.937×10^5 (m^{-2}), 6×10^{-4} (m), 10 (^{o}C)* and *45 (^{o}C)*, have dimensional units and directly come from empirical data, based on [62] and [65]. Based on the Cole's study [64], the frequency of detachment is function of waiting time between departure of bubble and appearance of subsequent one at the same nucleation site.

Wall heat flux

A description of waiting time t_{wait} and contact time $t_{contact}$ for a bubble with the heat wall is presented in Figure 3-2.

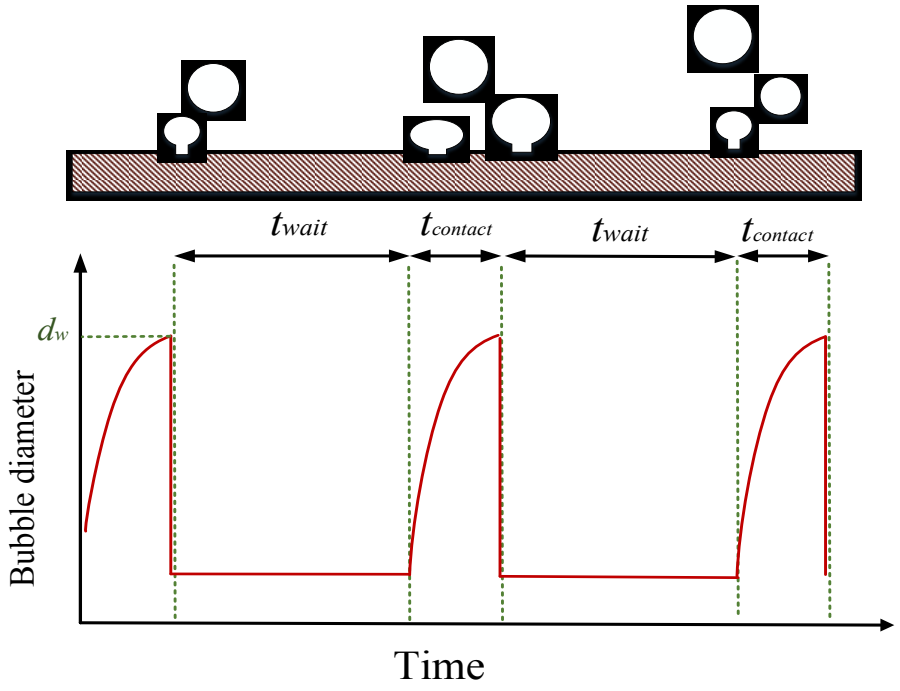

Figure 3-2: Waiting time and contact time for departed bubble when detaches at nucleation site- adapted figure from [64]

Since frequency of detachment is inversely proportional to the cycle time, then one can calculate frequency based on following relation:

$$f = \frac{1}{t_{wait} + t_{grow}} \simeq \frac{1}{t_{wait}} \sqrt{\frac{3(\rho_l - \rho_v)g}{4\rho_l d_w}} \quad (3.11)$$

The algorithm for the calculation of the wall heat flux partitioning model implemented in OpenFOAM is described in following flowchart Figure 3-3. If one assumes that heat flux is applied at boundary condition, first, an initial value is guessed for the wall superheat assuming that the total wall heat flux is devoted to single-phase heat transfer. If the wall superheat is greater than zero, an iterative loop will start with the calculation of the bubble properties like diameter, frequency, nucleation site density and area fraction.

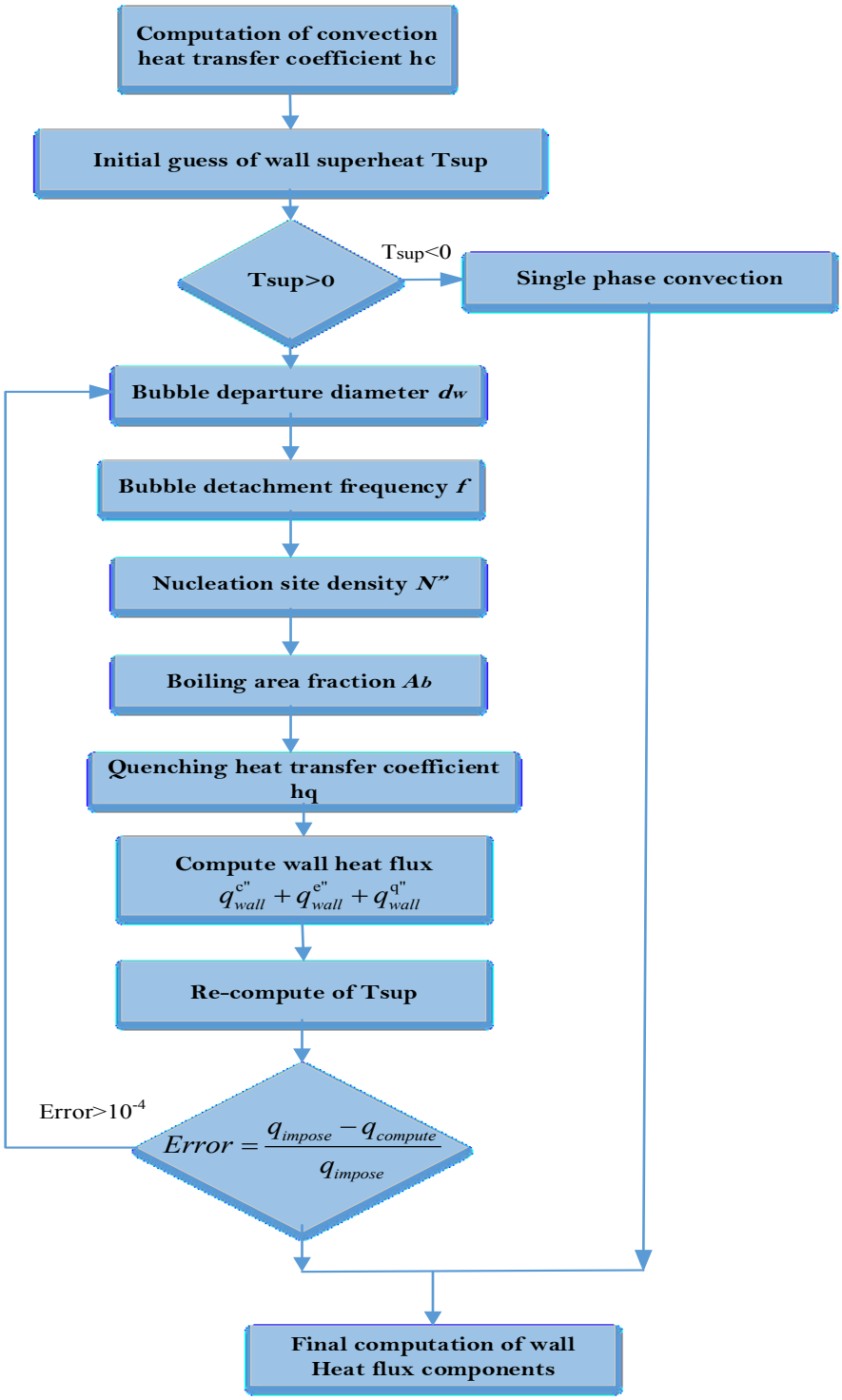

Figure 3-3: Algorithm of wall heat flux portioning model in OpenFOAM

CHAPITRE FOUR : Determination of Heat Transfer for Flow Condensation inside of Horizontal Smooth Tube

AVANT-PROPOS

Auteurs et affiliation:

- Roshanak Rabiee: étudiante au doctorat, Université de Sherbrooke, Faculté de génie, Département de génie chimique et de génie biotechnologique.
- Martin Désilets: professeur, Université de Sherbrooke, Faculté de génie, Département de génie chimique et de génie biotechnologique.
- Pierre Proulx, professeur, Université de Sherbrooke, Faculté de génie, Département de génie chimique et de génie biotechnologique
- M. Ariana, étudiant postdoctoral, Université de Sherbrooke, Faculté de génie, Département de génie chimique et de génie biotechnologique
- M. Julien, chercheur chez Venmar Ventilation Inc.

Date d'acceptation: April 2018
État de l'acceptation: version finale publiée
Revue: International journal of Heat and Mass transfer

Référence: [11]

Titre français: Détermination du transfert de chaleur par condensation à l'intérieur d'un tube lisse horizontal

Contribution au document:

Cet article étudie la condensation à l'intérieur d'un tuyau d'horizontal à l'aide d'un modèle numérique. Un nouveau modèle de transfert de chaleur par condensation est proposé sur la base du méthode de partitionnement chaleur.

Résumé français:

Un modèle numérique a été développé avec OpenFOAM, une boîte à outils open source, pour simuler le processus de transfert de chaleur lors de la condensation dans un tube horizontal lisse. Le modèle

proposé reprend certaines des idées d'un modèle récent représentant l'ébullition sur une surface chauffée, déjà développé dans OpenFOAM version 4.x. Des modifications ont été apportées à ce modèle afin de prendre en compte la nature spécifique de la condensation. Un nouveau coefficient appelé «fraction de surface de condensation» est introduit et un nouveau code est ajouté au solveur pour simuler le flux de chaleur de la paroi pendant le processus de condensation. Afin d'évaluer les performances du nouveau modèle, des simulations numériques sont effectuées pour des flux de masse allant de 100 à 750 kg/m^2, avec une température de saturation nominale de 40 °C et un diamètre hydraulique compris entre 7 et 12 mm. Les prédictions numériques sont comparées aux résultats de deux travaux expérimentaux et un bon accord a été trouvé entre les mesures et les prédictions du modèle. Il montre la validité de la solution numérique suggérée pour la modélisation de la condensation en écoulement à l'intérieur d'un tube lisse horizontal. De plus, l'effet de certains paramètres tels que le flux de masse, le diamètre hydraulique du tube, la qualité de la vapeur et la différence de température sur le coefficient de transfert de chaleur est étudié. Enfin, une nouvelle relation pour la prévision du coefficient de transfert de chaleur total de la condensation est proposée.

4 CHAPTER FOUR: Determination of Heat Transfer for Flow Condensation inside of Horizontal Smooth Tube

4.1 Abstract

A numerical model has been developed with the open source toolbox OpenFOAM to simulate the heat transfer process during flow condensation inside a smooth horizontal tube. The proposed model borrows some of the ideas of a recent boiling model, already developed in OpenFOAM version 4.x. Modifications have been brought to this model to take into account the specific nature of flow condensation. A new coefficient called the "condensation area fraction" is introduced and a new library is added to the solver to simulate the wall heat flux during the condensation process. In order to assess the performance of the new model, numerical simulations are conducted for mass fluxes ranging from 100 to 750 kg/m^2.s, with a nominal saturation temperature of 40 ^{o}C and a hydraulic diameter between 7 and 12 mm. The numerical predictions are compared to the results of two experimental works and good agreement has been found between measurements and model's predictions. It shows the validity of the suggested numerical solution for modeling of flow condensation inside of a horizontal smooth tube. Moreover, the effect of some parameters such as mass flux, tube hydraulic diameter, vapor quality and temperature difference between the wall and saturation on the heat transfer coefficient are investigated. Finally, a new relationship for the prediction of the total heat transfer coefficient of flow condensation is proposed.

4.2 Literature review

Two-phase flow studies on boiling and condensation have attracted attention of researchers due to the high heat fluxes found during these processes. The condensers and evaporators are regularly used in air conditioning systems, ventilation systems, heat sinks and heat pipes. Lower service costs, higher thermal efficiency, less occupied space and easier monitoring, manufacturing and maintenance are some of the advantages of using these systems which explain the increasing use of such equipment in the industry. The ultimate goal of designing a cooling system is to get high heat transfer coefficients with a negligible pressure drop.

Mechanisms of heat and momentum transfer for in-tube condensation or boiling (called flow condensation and flow boiling) are strongly dependent on the prevailing two-phase flow regime.

For flow condensation inside a horizontal smooth tube, gravity and inertial forces are the two primary driving forces influencing the flow regime, which can be classified into stratified, stratified-wavy, transient and annular regime, depending on the flow conditions. In stratified and stratified-wavy flow regime, the gravitational force is more dominant than the inertial force and causes accumulation of the liquid film at the bottom of the tube. The liquid film then acts as a thermal resistance and decreases the heat transfer coefficient. At higher velocities, as the flow is entering the so-called annular regime, the shear stress forces control the flow, the liquid film thickness is diminished, and the heat transfer coefficient is increased [32]. Other types of flow regime like slug or mist flow are less frequent than stratified and annular regimes. Since heat transfer is strongly dependent on the interaction between gravity and inertial forces, suggested correlations for the calculation of heat transfer coefficients must be based on the prevailing flow pattern.

Studies on flow pattern map applied to condensation applications started with the work of Palen et al. [66]. Thome et al. [32] proposed a flow pattern map for flow condensation based on correlations established for different refrigerants taken from the literature and also studied the effects of interfacial roughness and mixtures of refrigerants on the heat transfer coefficient. Their suggested model predicted acceptable results for low-reduced pressure conditions. However, it shows significant discrepancy with experimental results at high-reduced pressure. Dobson et al.[35] conducted an experimental study on the impact of the flow regime on the heat transfer coefficient for condensation inside horizontal tubes with diameter ranging from 3 to 7 mm using various refrigerants including R-12, R-22 and R134a. Simulated flow pattern map was compared with the experimental observations. Moreover, the heat transfer coefficients for different flow regimes have been compared with the proposed correlations with noticeable discrepancies. Several correlations have been proposed to estimate the heat transfer coefficients of flow condensation. Each correlation is restricted to specific regimes with a validity range for parameters such as mass flux, Reynolds number etc. However, a few correlations, like Thome [32], Dobson and Chato [35], Shah [33], Cavallini [36], Travis [37] and Akers [34], can cover the entire range of flow regimes including stratified and annular regimes. However, using such correlations in a wide range of flow conditions necessarily leads to inevitable errors beyond acceptable range (±25%).

Numerous experimental studies have been performed to investigate the heat transfer

coefficient and pressure drop in flow condensation and compare experimental measurements with the estimations obtained from suggested correlations. Cavallini et al. [45] measured the heat transfer coefficients using different refrigerants such as R22, R134a, R32, R125, R410a and R407c in a horizontal 8 mm diameter tube for various ranges of mass flux, saturation temperature, vapor quality and temperature difference between saturation and wall (T_s-T_{wall}). They concluded that in stratified regime, the heat transfer is considerably affected by the temperature difference, T_{sat}-T_{wall}. However, in annular regime, the effect of parameters like mass flux, vapor quality and saturation temperature on the heat transfer coefficient is more significant than the temperature difference.

Suliman et al. [46] performed an analysis on the heat transfer coefficient of R-134a inside a smooth horizontal tube for a nominal saturation temperature of 40^{o}C and mass fluxes of 75-300 kg/m^2.s. Their experimental results showed a deviation of 15% and 18% when compared to Thome's [32] and Cavallini's [36] correlations, respectively. In addition, a new improved flow pattern map and a revised correlation for the calculation of the heat transfer coefficient were suggested. Hossain et al. [47] measured the heat transfer coefficient and pressure drop of different working fluids like R22, R1234ze and R410a inside a horizontal smooth tube having a diameter of 4.33 mm and a length of 3.6 m. They analyzed their experimental data to determine which fluid conducts higher heat transfer coefficients. They finally concluded that, at the same conditions, R32 produces a heat transfer coefficient of 70% and 20-45% higher than R410a and R1234ze, respectively. Panitapu [48] compared experimentally determined heat transfer coefficients and pressure drops with existing correlations. It is concluded that Shah's correlation [33] is more suitable for annular regime and Dobson's relation [35] leads to better predictions for the stratified regime.

Although there are many experimental works for the estimation of heat transfer coefficients in flow condensation regimes, only a few investigations are presented on the development of numerical models. In commercial software, there are available models that can be applied for boiling and condensation. Typically, the implemented models take into account the interfacial heat transfer between two phases, in the bulk of the working fluid, while the wall heat flux can only be represented with simplified boundary conditions like constant temperature or convection conditions.

Several studies, such as Michta [9], Ghione [10], Tripathi [40] and Shademan [41] have led

to the development of Euler-Euler models for the prediction of flow boiling with OpenFOAM platform. In Michta [9] and Chione [10], a two-phase flow model and subcooled boiling CFD code written in OpenFOAM is developed and validated. Their works became the reference of other researchers for completing pool and flow boiling models. Tripathi et al. [40] developed a computational model based on OpenFOAM to simulate a vapor-liquid flow boiling. They used a wall heat flux partitioning model, as proposed by Kurul and Podowsky [60] and applied it into the OpenFOAM solver. The dispersed phase fraction profile, liquid, and vapor temperature distribution were compared with experimental results. The purpose of this work is to show the performance of a new Euler-Eulerian model built in OpenFOAM for the simulation of flow condensation inside a horizontal smooth tube.

4.3 Governing equations

The OpenFOAM solver used in this study is based on an Euler-Eulerian method for compressible-incompressible, turbulent-laminar flow and is capable of modeling phase change in boiling and condensation. In this model, each phase is considered as a continuous phase and the governing equations including continuity, momentum and energy are separately solved for each phase. The continuity equation is re-written in the following form:

$$\frac{\partial \rho_a \alpha_a}{\partial t} + \nabla.(\rho_a \alpha_a \vec{U}_a) = \Gamma_{ab}^{+} - \Gamma_{ba}^{+} \qquad (4.1)$$

In this equation, α_a is the volume fraction of phase a, ρ_a and $\vec{U}_a$ are the density and velocity of phase *a* (vapor or liquid). Γ_{ab}^{+} describes mass transfer due to phase change. If *a* is the vapor and *b* is the liquid phase, Γ_{ba}^{+} represents the evaporation volumetric source term and Γ_{ab}^{+} is the condensation volumetric source term. This equation is manipulated to satisfy the boundedness of volume fraction [10].

$$\frac{\partial \alpha_a}{\partial t} + \nabla.(\alpha_a \vec{U}) + \nabla.(\alpha_a \alpha_b \vec{U}_r) + \left(\frac{\alpha_a}{\rho_a}\right)\frac{D p_a}{Dt} = \frac{\Gamma_{ab}^{+} - \Gamma_{ba}^{+}}{\rho_a} \quad (4.2)$$

The relative velocity $\vec{U}_r$ and the average velocity $\vec{U}$ are defined as below:

$$\vec{U}_r = \vec{U}_a - \vec{U}_b, \quad \vec{U} = \alpha_a \vec{U}_a + \alpha_b \vec{U}_b, \quad \alpha_a + \alpha_b = 1 \quad (4.3)$$

Similarly, the momentum equation is solved for each phase:

$$\frac{\partial(\rho_a \alpha_a \vec{U}_a)}{\partial t} + \nabla.(\rho_a \alpha_a \vec{U}_a \vec{U}_a) = -\alpha_a \nabla P + \alpha_a \rho_a \vec{g} \quad \cdot.[\alpha_a (R_a + R_a)] + \vec{M}_a + (\Gamma_{ab}^{+} \vec{U}_b - \Gamma_{ba}^{+} \vec{U}_a)$$

(4.4)

∇P is gradient of pressure, $(R_a + R_a^t)$ is the combined Reynolds viscous stress and turbulent stress. $\vec{M}_a$ represents the interfacial momentum exchange between the two phases including lift, drag, virtual mass, wall lubrication and turbulent dispersion forces [9]. The last term $(\Gamma_{ab}^{+} \vec{U}_b - \Gamma_{ba}^{+} \vec{U}_a)$ is added to the momentum equation because of the momentum transfer between the vapor and liquid due to phase changes. The energy equation for two-phase flow is:

$$\frac{\partial(\rho_a \alpha_a i_a)}{\partial t} + \nabla.(\rho_a \alpha_a i_a \vec{U}_a) = -\nabla.[\alpha_a (q_a + q_a^t)] + (\Gamma_{ab}^{+} i_b - \Gamma_{ba}^{+} i_a) + q_{wall}^{"} A_{wall}^{"} \quad (4.5)$$

Where i_a stands for the specific enthalpy of phase a, $(q_a + q_a^t)$ represents the molecular and turbulent heat flux inside phase *a* and $(\Gamma_{ab}^{+} i_b - \Gamma_{ba}^{+} i_a)$ is the source term added to the energy equation due to the mass transfer between phases [10]. The last terms in the energy equation include $A_{wall}^{"}$ and $q_{wall}^{"}$. $A_{wall}^{"}$ is the contact area with the wall per unit volume and $q_{wall}^{"}$ is the wall heat flux that is the main concern of this paper.

4.4 Boiling Wall heat flux

The boiling model is already implemented in the OpenFOAM solver called "reactingTwoPhaseEuler-Foam" available in versions 4.0 and newer; it is described in this section as a background for the next section. When applying the energy equation at the boundaries in boiling or condensation case, the most important term is the wall heat flux and it must be correctly modeled. Based on the proposed model of Kurul et al. [60], the heat transfer between the heated wall and the liquid originates from three different mechanisms as described below:

$$q_{wall}^{"} = q_{wall}^{c"} + q_{wall}^{e"} + q_{wall}^{q"} \quad (4.6)$$

Where q''_{wall} represents the single-phase convection heat flux, q''_{wall} is the evaporation heat flux and q''_{wall} is the quenching heat flux (Figure 4-1). Bubbles form at the wall nucleation sites leading to the vaporization of liquid; this part of the heat flux is directly related to the evaporation flux. When a bubble detaches from the wall, the colder surrounding liquid replaces the volume occupied by the bubble which creates a heat flux called quenching. The rest of the wall area that is not covered by any bubbles is used for single-phase convection heat transfer [60].

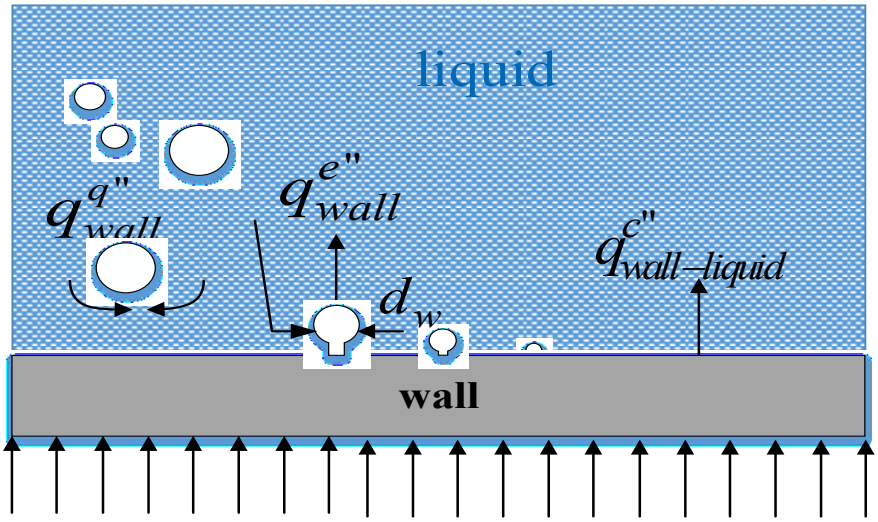

Figure 4-1: Wall boiling model consisting of evaporation, quenching and single-phase convection

The evaporation heat flux is a function of some important parameters such as the boiling area fraction A_b, latent heat of vaporization, density and velocity of the vapor.

$$q''_{wall} = \dot{r} \qquad ,) \quad (4.7)$$

Where $\dot{r}$ and h_{lv} are the mass flux generated by evaporation and the latent heat of vaporization, respectively. $U_{adj.v}$ is the velocity of vapor or bubble near the wall, a function of the frequency of detachment and the diameter of the detached bubble [9].

$$U_{adj.v} = f \times d_w \quad (4.8)$$

A correlation developed by Rohsenow [61] is used to represent the quenching heat flux:

$$q''_{wall} = A_b \frac{2\lambda_l (T_{wall} - T_{sat})}{\sqrt{\frac{\pi\lambda_l}{f \rho_l C_{p,l}}}} \quad (4.9)$$

The single-phase convective heat flux is calculated as:

$$q''_{wall} = (1 - A_b) H_{c,l} (T_{wall} - T_{sat}) \quad (4.10)$$

Where $H_{c,l}$ is the Stanton heat transfer coefficient for the single-phase convection of liquid and is calculated based on the Stanton number [9]. In the above equations, A_b is a non-dimensional number called the boiling area fraction. It represents the ratio of the wall area wetted by bubbles to the total area. Different models are proposed for the calculation of the boiling area fraction, diameter of the detached bubbles and frequency of detachment, but the most known references are [63], [62] and [64]. In Lemmert [63], the following correlation is suggested for the boiling area fraction as a function of the diameter of detached bubble and temperature difference between the wall and the liquid:

$$A_b = \pi d_w^2 \times 7.937 \times 10^5 [\frac{T_{wall} - T_{sat}}{10}]^{1.805} \quad (4.11)$$

The following expression is used for the calculation of the diameter of detached bubble [62]:

$$d_w = 6 \times 10^{-4} \times \exp[-\frac{(T_{sat,r} - T_l)}{45}] \quad (4.12)$$

Constant numbers, such as *7.937×10^5 (m^{-2}), 6×10^{-4} (m), 10 (^{o}C) and 45 (^{o}C)*, used in the previous correlations, have dimensional units and directly come from empirical data [63], [62]. Based on Cole's study [64], the frequency of detachment is calculated as below:

$$f = \sqrt{\frac{3(\rho_l - \rho_v)\,g}{4\rho_l d_w}} \quad (4.13)$$

4.5 Condensation wall heat flux

The main purpose of this paper is to propose a new model that is compatible with the OpenFOAM solver (*reactingTwoPhaseEulerFoam*) in order to simulate the condensation process occurring inside a heat exchanger. As a starting point, we propose to build upon from the previously described boiling model and adapt it to the physic of condensation. Condensation wall heat flux can be divided into two main contributions called the single-phase convection of vapor, q''_{wall} and the condensation heat flux, q''_{wall} as shown in Figure 4-2. Concept of quenching heat flux is not applicable in the condensation case. When a vapor at saturation condition gets in contact with a colder wall at a temperature below the saturation, a portion of the wall gets

wetted when some condensing droplets form. The rest of the wall is affected by the single-phase convection of vapor.

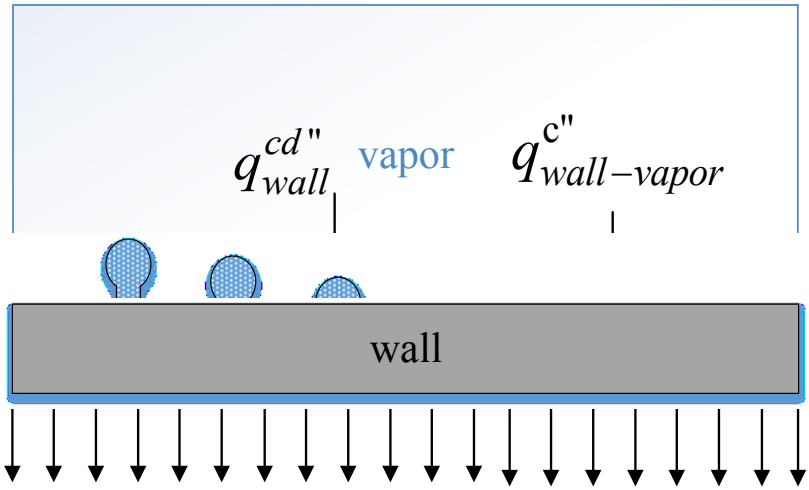

Figure 4-2: Wall condensation model consists of condensation heat flux and single-phase convection

The single-phase convection is represented by an equation similar to (4.10):

$$q''_{c,wall} = (1 - A_{cd}) H_{c,v} (T_{wall} - T_{sat}), \quad (W/m^2) \quad (4.14)$$

where $H_{c,v}$ is the Stanton heat transfer coefficient of single-phase convection that is calculated based on the Stanton Number [9] using the vapor properties.

The condensation heat flux can be presented in a form similar to the boiling heat flux:

$$q''_{cd,wall} = \rho \cdot \quad \cdot \quad U_{adj,l}) \quad (4.15)$$

In the above equations, A_{cd} is a non-dimensional parameter called the condensation area fraction, which represents the fraction of the wall area wetted by liquid droplets of condensing vapor to the total area ($0 < A_{cd} < 1$). Finally, $U_{adj,l}$ is the velocity of the liquid adjacent to the wall, a flow variable with the same order of magnitude of vapor velocity Eq. (4.8).

In order to estimate the condensation area fraction, one needs an estimation of the heat flux or heat transfer coefficient. Therefore, in the next section, some of the most known and well-validated correlations for the calculation of Nusselt number and heat transfer coefficient will be introduced.

4.5.1 Proposed Correlation for Heat Transfer Coefficient in Condensation

In the literature, there are many suggested correlations for the calculation of the heat transfer coefficient in different regimes of flow condensation, from stratified to stratified-wavy and

annular regimes [35]. As mentioned before, in flow condensation, the gravity and inertial forces are the two dominant drivers that determine the flow regime. In the stratified regime, mostly found when the mass flux G is < 500 (kg/m^2.s), the gravity force is more important than the inertial force. However, at higher mass flux, such as G > 500 (kg/m^2.s), high inertial and shear stresses lead to the annular flow regime resulting to a higher condensation heat flux [35]. Since recent studies indicate that the flow regime severely influences the heat and momentum transfer, the suggested correlations in the literature are based on the analysis of the prevailing flow patterns and given validity ranges of parameters, which are presented in TABLE 4-1. Both correlations can predict entire flow regimes including stratified to annular regime. However, as mentioned in [48] and [67], Shah's relation [33] better predicts behavior of annular regime and Akers's relation [34] is more suitable for modeling of stratified, stratified wavy regime.

TABLE 4-1: reference correlation used for calculation of condensation area fraction

Reference	Model	Regime
Shah (1979) [33]	$Nu = \frac{h_{corr} D}{\lambda_l} = Nu_l[(1-\mathrm{x})^{0.8} + \frac{3.8x^{0.76}(1-x)^{0.04}}{(P_{sat}/P_{cr})^{0.39}}]$ $\mathrm{Nu}_l = 0.023\,\mathrm{Re}_{lo}^{0.8}\,\mathrm{Pr}_l^{0.4}, \mathrm{Re}_{lo} = \frac{GD}{\mu_l}, 10.8 \le G \le 1600(kg/m^2.s)$ $0.2 \le P_{cr} \le 0.53, 7 \le D \le 40mm,\ \ \mathrm{Re}_{lo} \ge 350$	Annular and stratified flow
Akers at al. (1960) [34]	$G_e = G[(1-\mathrm{x}) + \mathrm{x}\left(\frac{\rho_l}{\rho_v}\right)^{0.5}], \quad \mathrm{Re}_e = \frac{G_e D}{\mu_l}, \mathrm{Nu} = \frac{h_{corr} D}{\lambda_l} = C\,\mathrm{Re}_e^n\,\mathrm{Pr}_l^{1/3}$ $C = 0.0265, \quad n = 0.8, \text{for} \quad \mathrm{Re}_e > 50000$ $C = 5.03, \quad n = 1/3, \text{for} \quad \mathrm{Re}_e < 50000$	Stratified and annular flow

4.5.2 Condensation area fraction

In the boiling model, the area fraction is a function of the diameter of detached bubbles and temperature difference between the wall and saturation Eq (4.11). However, in the case of condensation, there is no known relationship to estimate the condensation area fraction, A_{cd}. In this paper, a model is proposed for the calculation of such parameter, which is compatible with the OpenFOAM solver. In order to have an approximation for this important variable, first, it is necessary to calculate the heat flux for each control volume close to the wall. The following equation is used, assuming that the wall heat flux is equally distributed all over the wall surface:

$$q''^{cd}_{wall} = h_{corr}(T_{sat} - T_{wall}) \quad (W/m^2) \quad (4.16)$$

Where ($T_{sat} - T_{wall}$) is the sub-cooled temperature. The most known correlations such as Shah [33] and Akers et al. [34] presented in TABLE 4-1 are used to estimate h_{corr}. Hence, by using Eq.(4.15), A_{cd} is directly calculated.

$$A_{cd} = \frac{6q''^{cd}_{w}}{\rho_l(U_{adj,l})h_{lv}} \qquad (4.17)$$

By performing a sensitivity analysis using the chosen correlations in TABLE 4-1, it is found that A_{cd} is dependent on the aspect ratio of the tube (D/L), inlet mass flux G, temperature of wall and saturation temperature. The proposed relationship for the estimation of the condensation area fraction is presented as below:

$$A_{cd}(D/L, dT_{sub}, G, T_{sat}) = m \times e^{(n\mathrm{Re}_{lo})} + c \qquad (4.18)$$

where m and n are functions of the aspect ratio of the tube (D/L), sub-cooled temperature $T_{sat} - T_{wall}$ and saturation temperature T_{sat} (Eq. 4.19 & 4.20). Also, Reynold number of liquid is calculated as $\mathrm{Re}_{lo} = GD/\mu_l$. In this work, the working fluid is R134a thus m and n functions are estimated for this refrigerant by conducting a regression analysis. If the refrigerant is changed, the constants in Eq.(4.19) and (4.20) have to be recalculated with a regression analysis based on the refrigerant's specific data.

$$\begin{aligned} m(\frac{D}{L}, \frac{dT_{sub}}{T_{ref}}) &= 0.018 - (15.19 \times \frac{D}{L}) + (0.687 \frac{dT_{sub}}{T_{ref}}) \\ &+ (3671 \times (\frac{D}{L})^2) - (151 \times \frac{D}{L} \times \frac{dT_{sub}}{T_{ref}}) \\ &+ (-262100 \times (\frac{D}{L})^3) + (10980 \times (\frac{D}{L})^2 \times \frac{dT_{sub}}{T_{ref}}) \end{aligned} \qquad (4.19)$$

$$n = \frac{1.24 \times 10^{-7}}{(D/L)}, c = 0.04(\frac{T_{sat}}{T_{ref}} - 1) + 0.001 \qquad (4.20)$$

Where dT_{sub} is the sub-cooled temperature, (D/L) is the aspect ratio of the tube. Finally $T_{ref} = 40^o C$ and T_{sat} are the reference and saturation temperatures respectively. The Eq. (4.19) and (4.20) are bounded to generate a value between zero and one for A_{cd}.

4.6 Validation of condensation model

In order to validate the proposed condensation model, the experimental results of Suliman et

al. [46] and Cavallini et al. [45] have been selected and simulated with our OpenFOAM model. The first simulation case (*Case I*) simulates the Suliman's study [46] while the second one (*Case II*) is based on the Cavallini's study [45]. The geometry is illustrated in Figure 4-3 a uniform 3D hexahedral mesh is selected for the simulation of the flow and mass fraction fields (Figure 4-4). The result of grid sensitivity based on the mean error (see Eq.4.25), calculated between the experimental and numerical results are shown in TABLE 4-2. The number of cells in different directions is chosen in order to get the best compromise between the lowest mean error, less computational time and best convergence for each case. The details of the boundary conditions of references [46] and [45] are presented in TABLE 4-3 and TABLE 4-4.

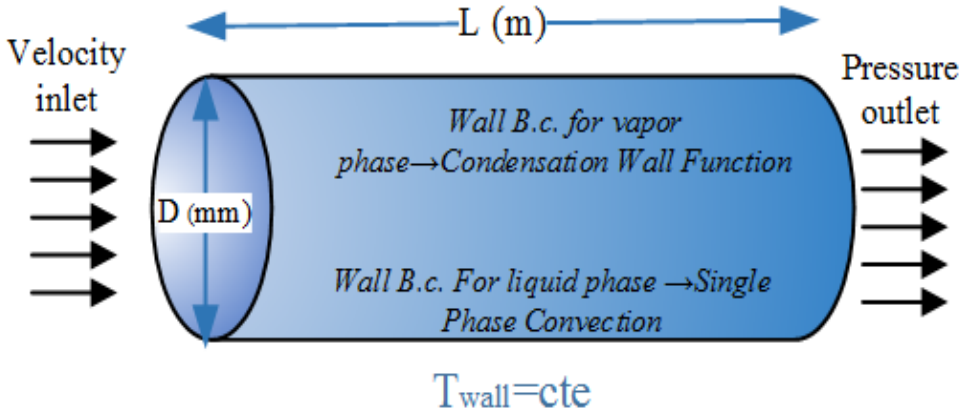

Figure 4-3: Geometry and boundary condition of tube

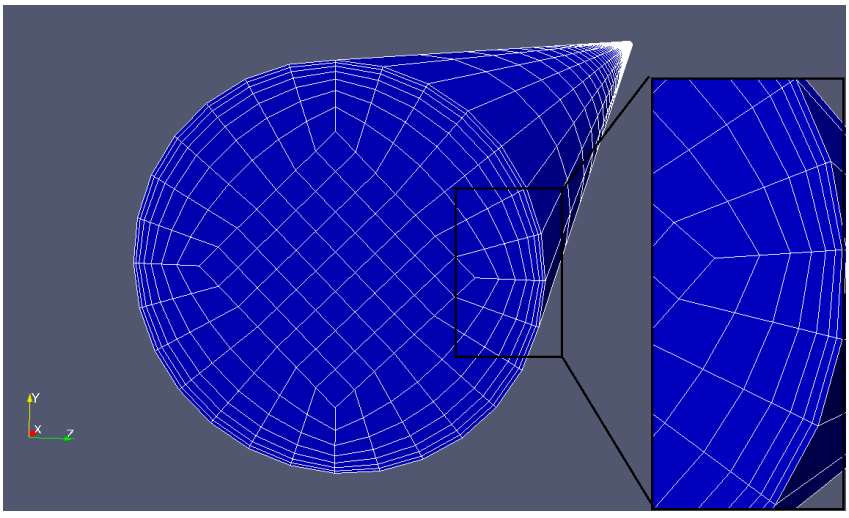

Figure 4-4: 3D-hexahedral mesh and gravity direction

TABLE 4-2: Grid sensitivity analysis

Grid number	Mean error value %
16×80	17.593
24×110	9.154
28×154	1.707
32×180	1.550

4.7 Numerical Solution

The new OpenFOAM solver is enthalpy-based and uses an Euler-Eulerian approach in which each phase is considered as a continuous phase and boundary conditions are applied for each phase, separately. In other words, each variable such as velocity, pressure, temperature, and phase fraction is considered for both phases. Interfacial momentum transfer terms (described in chapter 2.1.3) can be added to the solver by the user. In this study, we only add drag and virtual mass forces to the momentum equations, which have considerable effect than the other forces. In addition, a constant diameter model is considered for the dispersed phase. The variation of the saturation pressure with temperature has been taken into account by using a constant approximation. The mixture κ-ε turbulence model is used to simulate the turbulence effects on both continuous and dispersed phases. The PISO algorithm is used to take into account the coupling between velocity and pressure. A combination of Gauss-upwind, Gauss linear and Gauss limited linear schemes is selected for the discretization of the spatial derivatives. For the time derivative, the first order Euler implicit method is applied. We develop and add a new wall heat flux library called "*WallCondensation*" to the basic solver for modeling condensation problems.

The initial and boundary conditions are selected to have the best match with the experimental conditions. The velocity, phase fraction and temperature are set based on inlet conditions mentioned in TABLE 4-3 and TABLE 4-4. In this study, for the liquid and vapor phases, no slip boundary condition at the wall is used. For the outlet, a pressure boundary condition for avoiding reverse flow is applied. The condensation wall function is added to the vapor phase. For the liquid phase, a conventional convection boundary condition is applied (Figure 4-3). We perform the simulations using a very small time step (approximately 10^{-6} s) and continue

calculations until minor changes are observed in the most important variables like temperature, pressure and enthalpy.

TABLE 4-3: Properties and geometry of Ref [46]–case I

Parameters	Value
Refrigerant	R-134a
Hydraulic diameter, D	9 mm
Length of tube, L	1.54 m
Inlet temperature	40 ^{o}C
Inlet pressure	101660 Pa
Mass flux, G	125-300 kg/m^2.s
Sub-cooled temperature	
For G=125 (kg/m^2.s)	ΔT_{sub}= 4.68 ^{o}C→ T_{wall}=35.32 ^{o}C
For G=175 (kg/m^2.s)	ΔT_{sub}= 4.22^{o}C→ T_{wall}=35.78 ^{o}C
For G=200 (kg/m^2.s)	ΔT_{sub}=2.81 ^{o}C→ T_{wall}=37.19 ^{o}C
For G=250 (kg/m^2.s)	ΔT_{sub}= 4.15^{o}C→ T_{wall}=35.84 ^{o}C
For G=300 (kg/m^2.s)	ΔT_{sub}=3.98 ^{o}C→ T_{wall}=36.02 ^{o}C
Vapor quality at inlet	0.6-0.7
Vapor phase fraction at inlet	0.92-0.95

TABLE 4-4: Properties and geometry of Ref [45]–case II

Parameters	Value
Refrigerant	R-134a
Hydraulic diameter, D	8 mm
Length of tube, L	1.0 m
Inlet temperature	40 ^{o}C
Inlet pressure	101660 Pa
Mass flux, G	65-750 kg/m^2.s
Sub-cooled temperature	
For G=65 (kg/m^2.s)	ΔT_{sub}= 3 ^{o}C→ T_{wall}=37 ^{o}C
For G=100 (kg/m^2.s)	ΔT_{sub}= 4 ^{o}C→ T_{wall}=36 ^{o}C
For G=200 (kg/m^2.s)	ΔT_{sub}= 8 ^{o}C→ T_{wall}=32 ^{o}C
For G=300 (kg/m^2.s)	ΔT_{sub}= 9 ^{o}C→ T_{wall}=31 ^{o}C
For G=400 (kg/m^2.s)	ΔT_{sub}= 8 ^{o}C→ T_{wall}=32 ^{o}C
For G=750 (kg/m^2.s)	ΔT_{sub}= 10 ^{o}C→ T_{wall}=30 ^{o}C
Vapor quality at inlet	0.6-0.7
Vapor phase fraction at inlet	0.92-0.95

Instead of using the flow pattern map of Dobson et al. [35], the simulated results were overlaid

into the improved flow pattern map of Suliman [46], in which the transition line (dotted line) is going upward on the left (see Figure 4-5). It clearly shows that the majority of the simulation data can be categorized into the stratified and stratified wavy regimes. Consequently, both aforementioned correlations in TABLE 4-1 can be used. The simulation case that relates to G=750 (kg/m^2.s) can be characterized as intermittent and annular regimes and higher discrepancy is expected for this case.

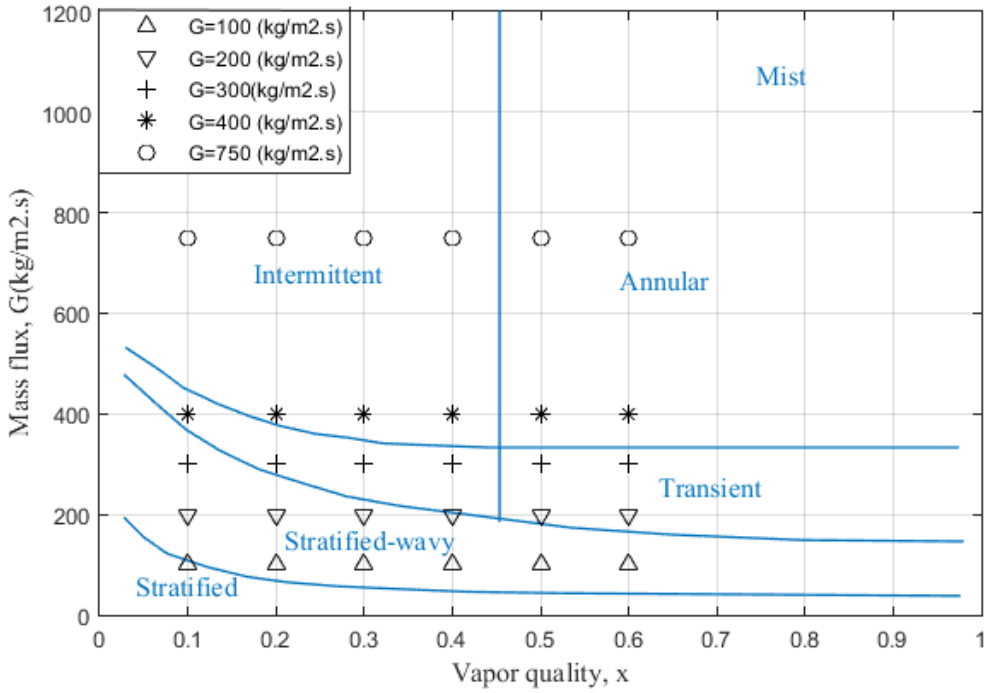

Figure 4-5. Simulation results into flow pattern map of Suliman -[46]

4.7.1 Results and Discussion

The tube is divided into small sub-sections where the vapor quality is approximately constant. The heat flux on the wall's control volume of each sub-section are summed and a local heat transfer coefficient is calculated based on following relations:

$$q_{local} = (\sum_{i=1}^{j} q_{w,i}^{cd"}) \times A_{elem} + (\sum_{i=1}^{j} q_{w,i}^{c"}) \times A_{elem}$$
$$h_{local} = \frac{q_{local}}{\pi D L_j (T_{sat} - T_{wall})} \quad (4.21)$$

Where j is number of wall's control volume for one sub-section and L_j is the length of one sub-section. For *case II*, as mentioned in [45], a log-mean temperature is used for the calculation of

the local heat transfer coefficient. The same approach is adapted in the treatment of the modeling results for *case II*.

$$\Delta T_{\ln} = \frac{(T_{in} - T_{wall}) - (T_{out} - T_{wall})}{\ln[\frac{(T_{in} - T_{wall})}{(T_{out} - T_{wall})}]} \quad (4.22)$$

The total heat transfer coefficient is also calculated for the whole length of the tube using a total heat flux as the combination of all heat fluxes at the wall's control volumes.

$$\begin{aligned} Q_{total} &= (\sum_{i=1}^{k} q_{w,i}^{cd"}) \times \mathrm{A}_{elem} + (\sum_{i=1}^{k} q_{w,i}^{c"}) \times \mathrm{A}_{elem} \\ h_{Total} &= \frac{Q_{tot}}{\pi DL(T_{sat} - T_{wall})}, h_{Total} = \frac{1}{L}\sum_{i=1}^{k} h_{local,i} \times L_i \end{aligned} \quad (4.23)$$

Where k is the number of all wall's control volumes. Again, instead of using temperature differences, log-mean temperature differences are used for *case II*. The temperature of the wall used in the equations (4.21), (4.22) and (4.23) is the inner sidewall temperature. The results of reference papers were presented as the heat transfer coefficients versus vapor quality, so the relationship of Zivi [68] is used to convert vapor phase fraction to vapor quality:

$$x = \left[(\frac{1-\alpha_v}{\alpha_v})(\frac{\rho_v}{\rho_l})^{-0.6667} + 1 \right]^{-1} \quad (4.24)$$

Mass flux, hydraulic diameter, vapor quality, and sub-cooled temperature all play an important role on the heat transfer coefficient. Other parameters like the saturation temperature, reduced pressure and inlet condition (saturated vapor or superheated vapor) can also influence the heat transfer coefficient. However, the saturation condition is kept constant in this study and saturated vapor is considered at the entrance of the tube.

4.7.2 Validation of Simulation Results

In order to validate the proposed condensation model, the total heat transfer coefficient is calculated based on Eq.(4.23) and compared to the measured values taken from the works of Suliman et al. [46] and Cavallini et al. [45].This comparison is presented in TABLE 4-5 and TABLE 4-6. The mean error reported in these tables is calculated as follows:

$$Error_{mean} = \frac{(h_{sim} - h_{\exp})}{0.5 \times (h_{sim} + h_{\exp})} \times 100 \quad (4.25)$$

The obtained results show a satisfactory agreement between the predicted heat transfer coefficients and the experimentally determined values. Simulation results indicate a mean error of 11% for *case I & II*, which is acceptable for the calculation of heat transfer coefficients as applied to different flow regimes, geometries and conditions. The source of error can be related to the temperature boundary condition applied at the wall. More precisely, the authors of experimental study (*case II*) [45] installed thermal sensors at the external surface of the tube. They estimated the inner sidewall temperatures based on the measured external temperatures and wall heat flux taken by the water cooling system. Then, they have computed the sub-cooled temperature and used it to show the relation between the heat transfer coefficient and dT_{sub}. However, no inner sidewall temperatures were reported in their paper. In our numerical simulation, a Dirichlet boundary condition has been estimated based on mean value of this interior wall temperature shown in reference's results. Therefore, a hard-to-estimate discrepancy between the estimated boundary condition and the real experimental values probably affects the comparison between model predictions and experimental data.

In *case II* at a mass flux of G=750 (kg/m^2.s), when the flow is entering in the intermittent and annular flow regime, the precision of the reference correlations and consequently the accuracy of the proposed model are degraded and the error becomes higher than 25%.

TABLE 4-5: Total heat transfer coefficient for case I

G (kg/m^2.s)	h-experimental (kW/m^2.K)	h-simulation (kW/m^2.K)	Mean Error %
125	1.500	1.288	15.206
175	1.682	1.545	8.484
200	1.808	1.709	4.017
250	1.832	1.758	4.112
300	1.849	1.931	4.343

TABLE 4-6: Total heat transfer coefficient for case II

G (kg/m^2.s)	h-experimental (kW/m^2.K)	h-simulation (kW/m^2.K)	Mean Error %
65	1.709	1.597	6.773
100	1.965	1.550	23.611
200	2.235	1.842	19.316
300	2.690	2.417	10.678
400	3.413	3.214	6.002
750	5.331	4.027	27.873

The results are also presented in Figure 4-6 with a different perspective, using deviation bands put at ±25%. Since most of the obtained results are within 11% of error, it is concluded that the proposed model leads to acceptable estimation of the heat transfer coefficients. Accordingly, the proposed model for condensation is confirmed with the experimental results of [46], [45] and it is capable of modeling flow condensation in stratified and stratified-wavy regimes. However, when the flow regime is entering annular flow, the accuracy of the condensation model is degraded.

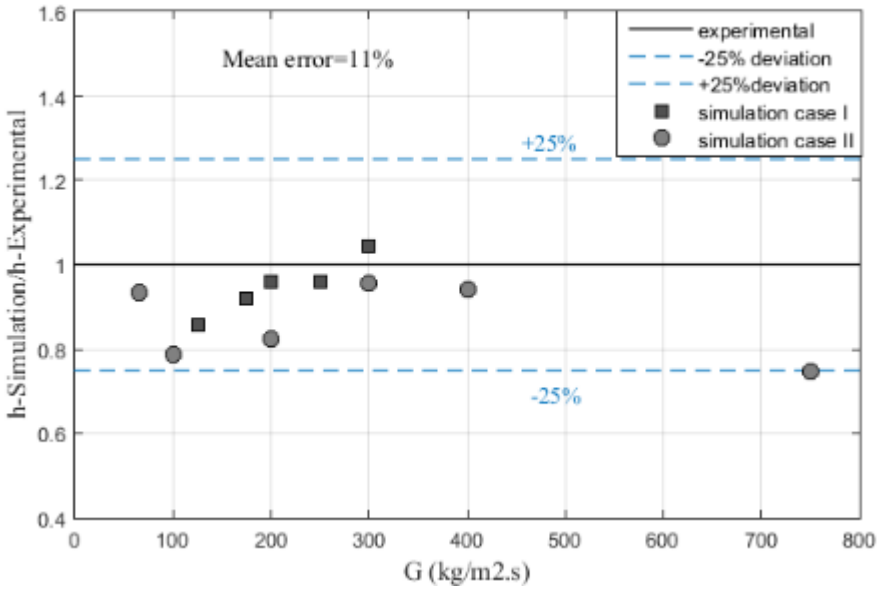

Figure 4-6: Deviation graph for total heat transfer coefficients of case I & case II

In Figure 4-7, the local heat transfer coefficients predicted by the model for *case I* with three different mass fluxes are compared with the experimental results. These three mass fluxes are chosen to be representative of the whole range of mass fluxes studied in reference [46]. Again, the simulation results show a good agreement with the experimental data since they mostly have an error of less than 25%. The mean error is approximately 12% while the simulation cases systematically underestimate the local heat transfer coefficient. The errors can also be explained by the calculation of the condensation area fraction. This study proposes a general equation for the calculation of this variable based on parametric estimations. Inevitable discrepancies in the calculation of the condensation area fraction for different geometries and different boundary conditions are expected in the simulation results. The local heat transfer coefficients predicted by the model for *case II* associated with four different mass fluxes are depicted against the

experimental results in Figure 4-8. The indicated mean error of 13% is higher in this case. The simulation results also demonstrate that the proposed model for condensation gives acceptable results and has errors of less than 25%, which is acceptable for the calculation of heat transfer coefficients.

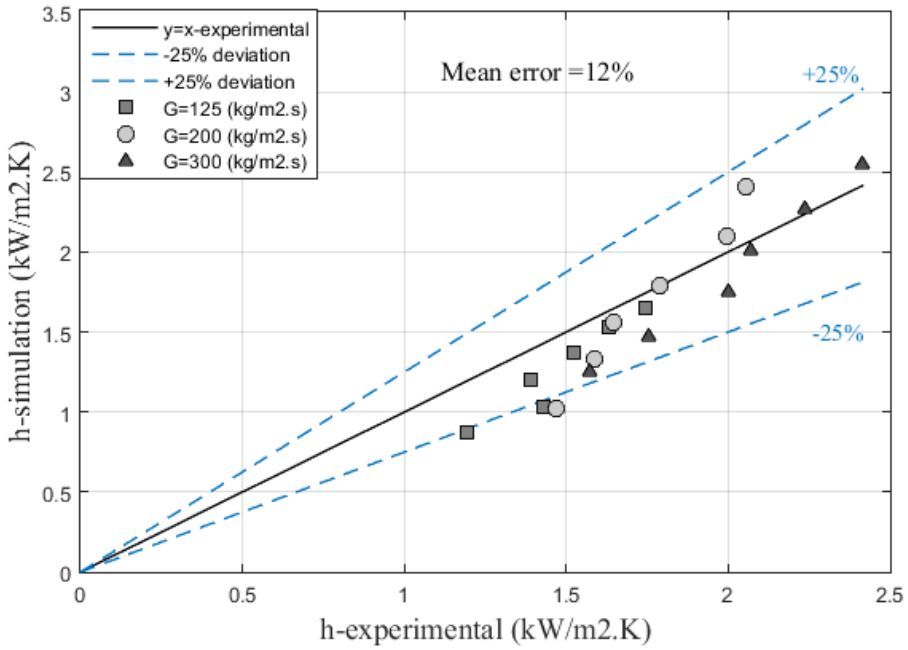

Figure 4-7: Local heat transfer coefficients versus experimental results for different mass fluxes-case I

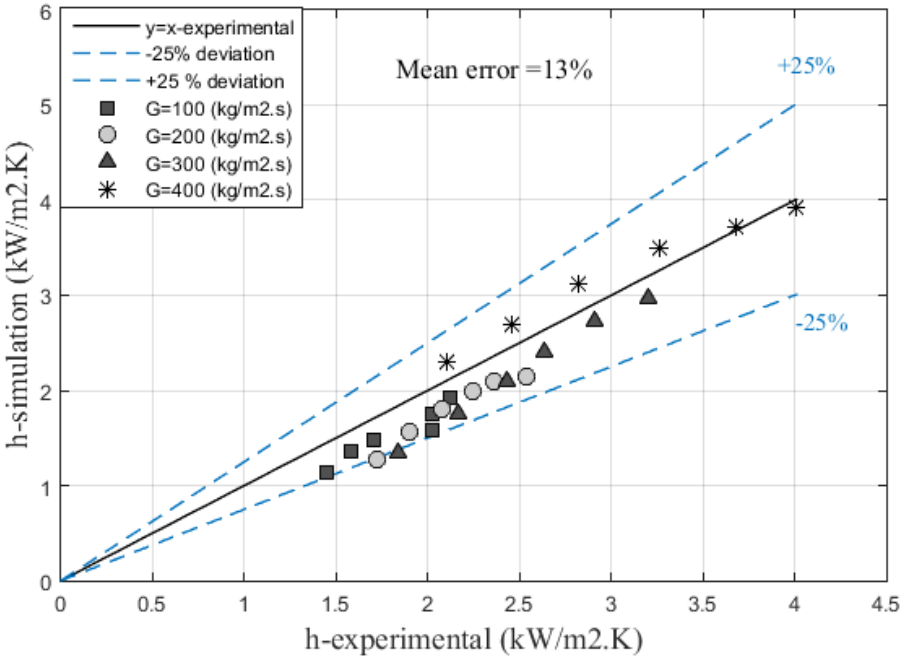

Figure 4-8: Local heat transfer coefficients versus experimental results for different mass fluxes-case II

The behavior of the local heat transfer coefficient with the vapor quality and mass fluxes can also be extracted from the simulation results. The local heat transfer coefficients for cases *I* and *II* are plotted versus the vapor quality for various mass fluxes. They are compared with the experimental data and the reference correlations introduced in TABLE 4-1. As illustrated in Figure 4-9 the simulation results have under predicted experimental data but within a deviation band of less than ±25%. Moreover, Shah's correlation [33] under predicted heat transfer coefficients for lower mass fluxes and over predicted them at higher mass fluxes. A reverse trend can be observed for Akers'correlation [34] as mentioned in [48].

Unexpectedly, at lower mass fluxes, the simulated results have a higher discrepancy when compared to experimental results. As mentioned before, it could be attributed to the difference between the calculation of the inner sidewall temperature in experimental works and the boundary condition considered in the numerical simulation. As expected, the local heat transfer coefficient increases by increasing the vapor quality, since, at higher vapor quality, the condensation rate is higher. Also, when the vapor quality is decreased, the liquid proportion becomes thicker than that of vapor, and hence, the condensation rate is slowed down. The same behavior has been seen for the effect of the mass flux. When the mass flux is increased, the local heat transfer coefficient is also increased. As expected, at higher mass flux, the shear force is more dominant than the gravitational force and the liquid film thickness becomes thinner. Therefore, a convective condensation regime with higher heat transfer coefficient is achieved.

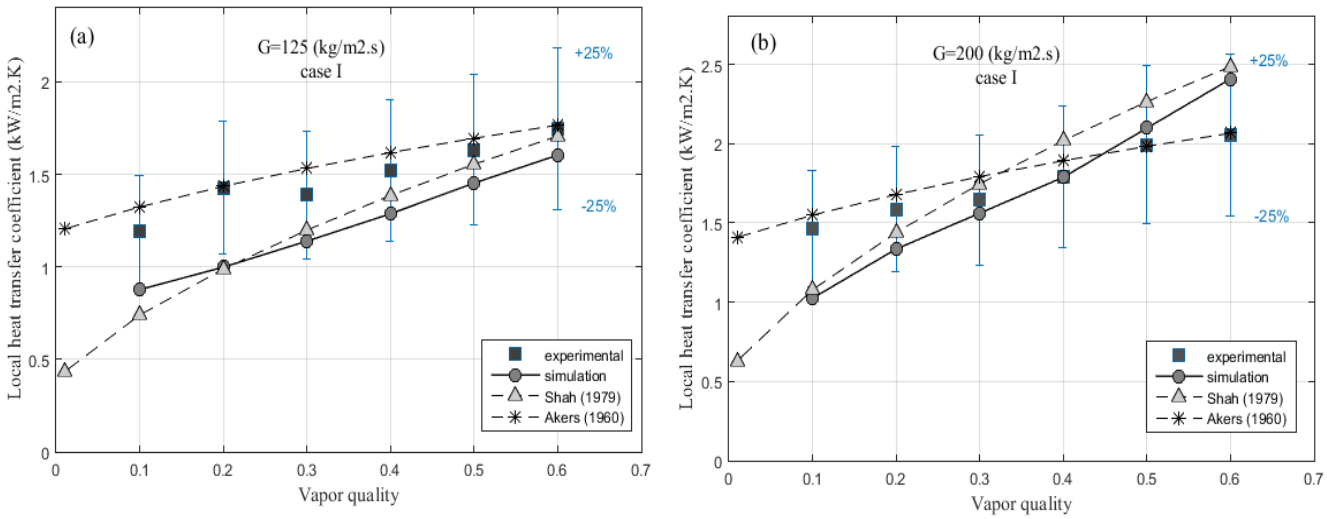

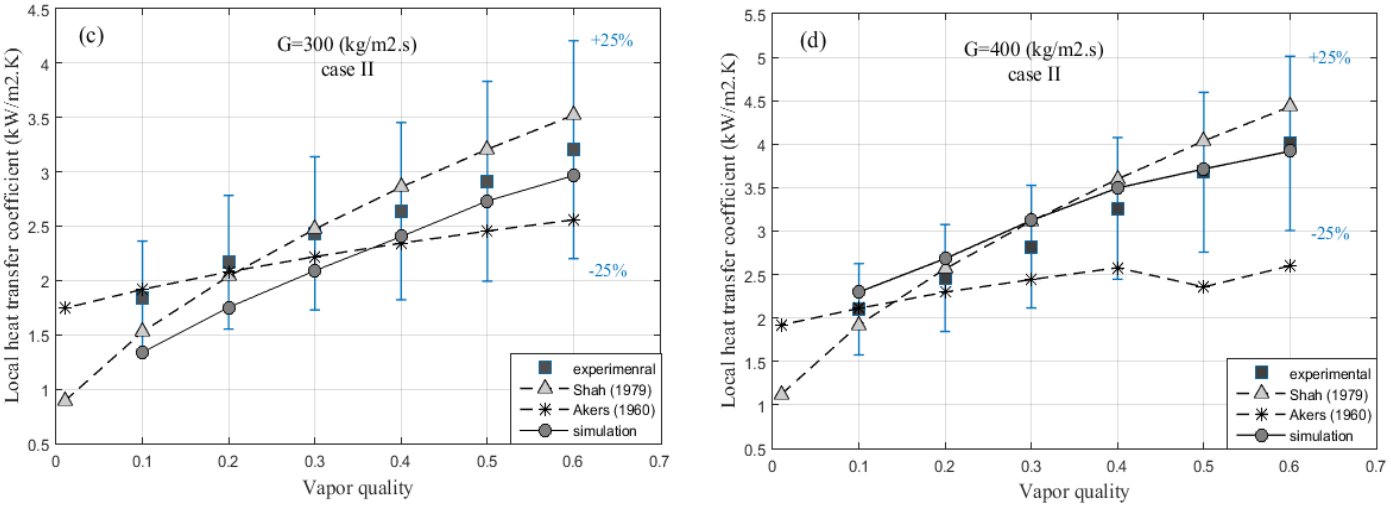

Figure 4-9: (a), (b)- Local heat transfer coefficients versus vapor quality- at three mass fluxes G=125, 200 kg/m2.s for case I & Fig. 9 (c), (d) G=300, 400 (kg/m2.s) for case II, compared with experimental result and correlations data

4.7.3 Effect of Mass Flux, Diameter and Sub-Cooled Temperature

After having validated the proposed condensation model, a sensitivity analysis is performed to investigate the effect of the main variables on the flow condensation. As mentioned before, a constant saturated condition at the entrance and a constant length of the tube are maintained. The remaining significant parameters affecting the flow field and the heat transfer coefficient are classified into inlet mass flux, hydraulic diameter and sub-cooled temperature.

Figure 4-10 shows the local heat transfer coefficients versus the vapor quality for different mass fluxes. At low mass fluxes, the gravitational force is dominant and a liquid film accumulates at the bottom of the tube, creating a liquid layer with low conductivity and decreasing the condensation heat flux. In addition, the slopes of the curves at low mass fluxes are nearly flat. When the mass flux is increased, the vapor shear stress becomes more important than the gravitational force. The liquid film then becomes thinner, leading to an increase in the local heat transfer coefficient. In this case, the variation or slope of heat transfer coefficient with vapor quality is enhanced.

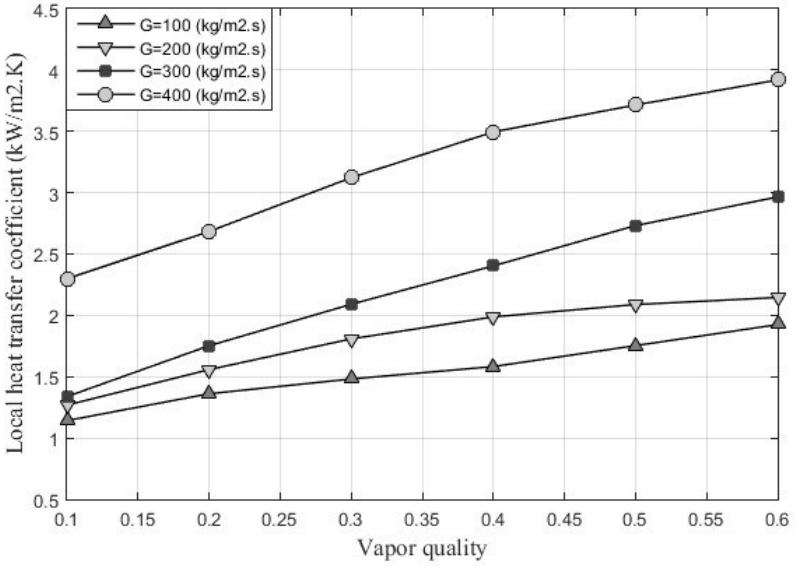

Figure 4-10: Local heat transfer coefficient versus vapor quality at different mass fluxes, *D=9 mm, L=1 m, dT_{sub}=3°C, T_{sat}=40 °C*

In order to investigate the effect of the temperature difference on the heat transfer coefficient, the simulation data are first overlaid on the flow pattern map developed by Palen [66] and Cavallini [69] with the Martinelli parameter on the *x-axis* and the dimensionless vapor velocity on the *y-axis*, see Figure 4-11. The blue dotted line that shows the corrected transition line was proposed by Sulimen [46] to improve the transition line of this flow pattern map. The Martinelli parameter and the dimensionless vapor velocity are calculated from following relations :

$$X_{tt} = \left(\frac{\mu_l}{\mu_v}\right)^{0.1}\left(\frac{\rho_v}{\rho_l}\right)^{0.5}\left[\frac{1-x}{x}\right]^{0.9} \qquad (4.26)$$

$$J_v = \frac{xG}{\sqrt{gD\rho_v(\rho_l-\rho_v)}}$$

As indicated in Figure 4-11, the majority of the simulated test cases are inside of the temperature difference (dT_{sub}) dependent regime. It means that the effect of sub-cooled temperature on the heat transfer coefficient is considerable. However, as the mass flux increases (G>750 kg/m^2.s), the flow is entering into dT_{sub}-independent regime where the effects of other parameters like mass flux and vapor quality become more significant than the sub-cooled temperature.

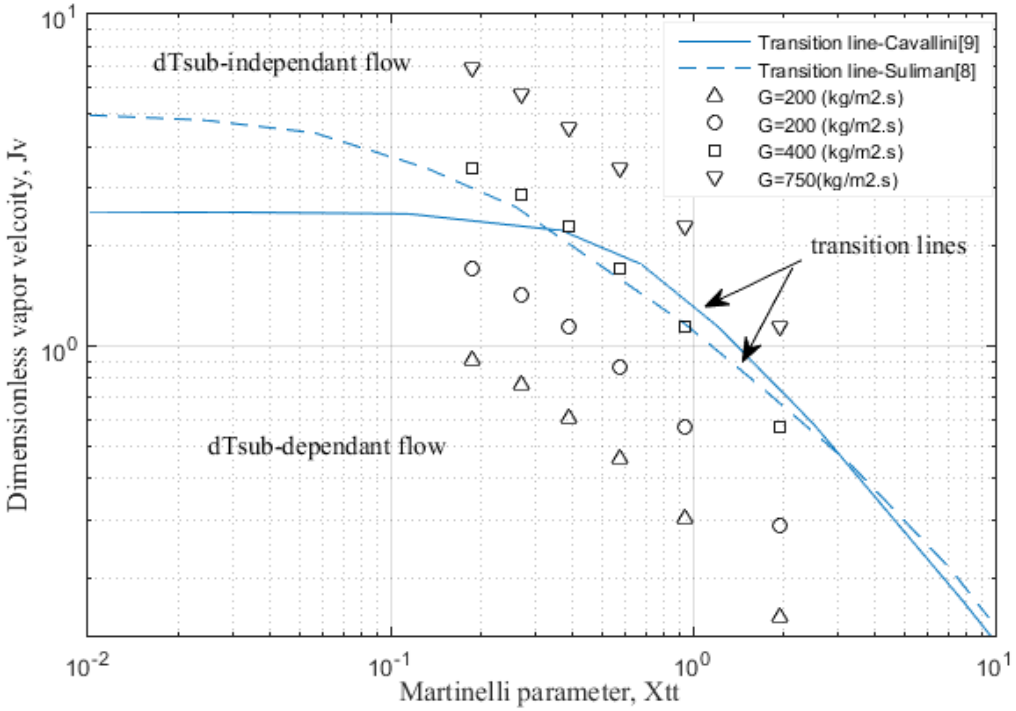

Figure 4-11: Flow pattern map to identify the temperature dependency

In TABLE 4-7 the total heat transfer coefficient is presented in function of the temperature difference, at different mass fluxes. It is found that, as the sub-cooled temperature is increased, the thickness of the condensing liquid is more important and the heat transfer coefficient is consequently decreased. Moreover, a new variable called the slope percentage, which shows the variation of the heat transfer coefficient with temperature difference, is used to assess the impact of dT_{sub} on h_{tot}. As illustrated in TABLE 4-7, when the mass flux increases from 200 to 750 (kg/m^2.s), the value of the slope or the dependency of the total heat transfer coefficient on the temperature difference is slightly decreased. However, these changes are not significant and it is concluded that simulation cases are in dT_{sub}-dependent regime. It is worth mentionning that in stratified or stratified-wavy regime, the total heat transfer coefficient is only dependent on the sub-cooled temperature and in the annular regime, the total heat transfer coefficient changes with mass flux [70].

TABLE 4-7: effect of sub-cooled temperature on heat transfer coefficient

	dT_{sub},K	h_{total} (kW/m^2.K)		dT_{sub},K	h_{total} (kW/m^2.K)
Diameter = 8 mm , T_{sat}=40 ^{o}C					
G=200 (kg/m^2.s)	2	2.011	G=750 (kg/m^2.s)	2	4.382
	3	1.720		3	4.327
	4	1.768		4	4.155
	5	1.564		5	3.874
	6	1.529		6	3.559
slope %		6.861%	slope %		5.198 %

The effect of the hydraulic diameter on the total heat transfer coefficent is presented in TABLE 4-8. As expected, it demonstrates that a tube with a lower diameter has a higher heat transfer coefficient when the mass flux is kept constant. At lower diameters, the flow regime is faster shifting from stratified to annular regime. Consequently, a higher condensation heat flux is achieved.

TABLE 4-8: effect of hydraulic dimeter on heat transfer coefficient

	Diameter (mm)	dT_{sub}	T_{sat} (^{o}C)	h_{total} (kW/m^2.K)
G= 200 (kg/m^2.s)	7	3	40.0	1.798
	8	3	40.0	1.720
	9	3	40.0	1.707
	10	3	40.0	1.679
	12	3	40.0	1.592

4.7.4 Condensation Number

A new and simple relation for the total heat transfer coefficient of horizontal smooth tubes is now proposed in this section. Based on the reference correlations in TABLE 4-1, the total heat transfer coefficient is a function of mass flux, hydraulic diameter, density of the vapor and liquid, liquid thermal conductivity, dynamic viscosity of the liquid and saturation temperature. Holman [71] introduced a new dimensionless variable called the condensation number (*Co*) as below:

$$Co = h_{tot}[\frac{\mu_l^2}{\lambda_l^3 \rho_l (\rho_l - \rho_v) \mathrm{g}}]^{1/3} \quad (4.27)$$

This parameter has been found to be a function of Reynolds number of liquid, saturation temperature and flow regime by performing a sensitivity analysis on the calibrated model. In Figure 4-12, the condensation number is depicted versus the liquid Reynold number. The following equation (Eq.4.28) is representing the data shown in this figure.

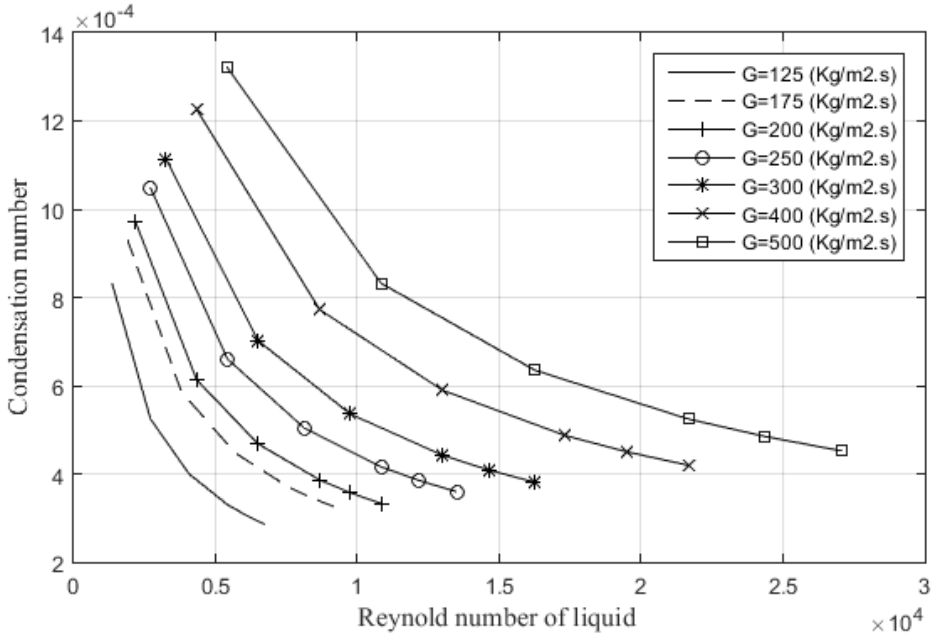

Figure 4-12: Relation between the condensation number and the liquid Reynolds number for different mass fluxes

$$\begin{aligned} Co &= m \times \mathrm{Re}_{lo}^{n}, \quad , n = -0.667 \\ m &= -0.01993 + 0.0005007(T_{sat} / T_{ref}) \end{aligned} \quad (4.28)$$

Consequently, the total heat transfer coefficient can be estimated as below:

$$h_{total} = Co \times [\frac{\lambda_l^3 \rho_l (\rho_l - \rho_v) \mathrm{g}}{\mu_l^2}]^{1/3} \quad (4.29)$$

In the following TABLE 4-9 , the total heat transfer coefficient as calculated by Akers, Shah and the new correlation (Eq. 4.29) are compared with the experimental data for *case I*. It shows that the suggested correlation has the same accuracy as Akers' correlation [34] for the prediction of the heat transfer coefficient.

TABLE 4-9: Validation of suggested correlation for condensation heat transfer

G (kg/m².s)	h-exp. (kW/m².K)	h-pred. (kW/m².K)	h-Akers (kW/m².K)	h-Shah (kW/m².K)
Diameter = 9 mm , dT_{sub} =3, T_{sat}=40 °C				
125	1.500	1.674	1.6722	1.4894
175	1.682	1.872	1.870	1.949
200	1.780	1.957	1.955	2.119
250	1.832	2.108	2.106	2.593
300	1.849	2.240	2.238	3.005

The value of the total heat transfer coefficient in Eq.(4.29) is also compared to the experimental data in Figure 4-13. This figure shows that the suggested correlation has an error of less than 25%.

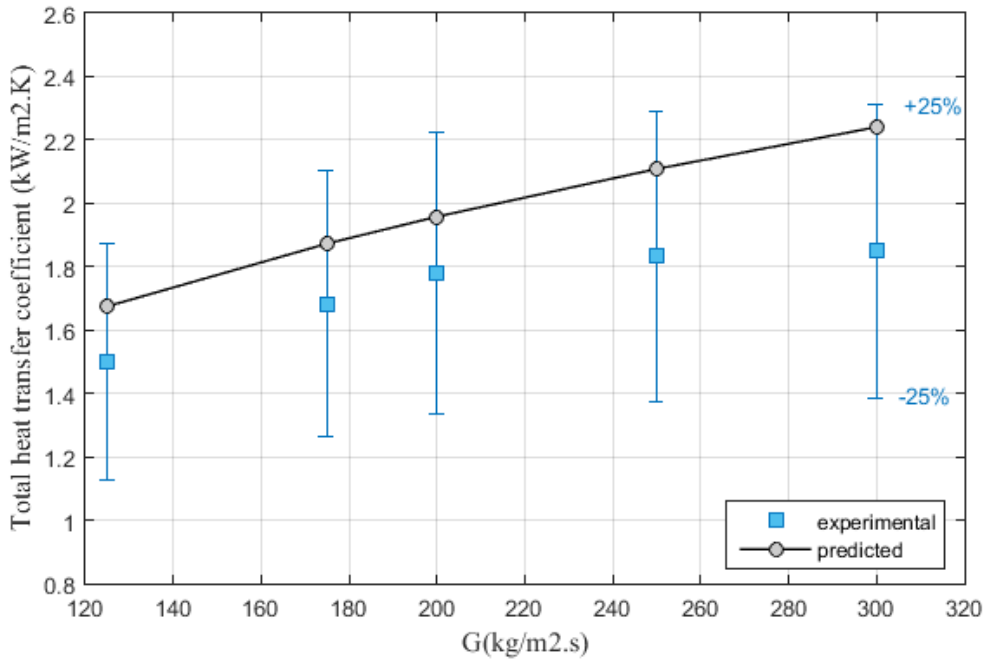

Figure 4-13: Comparison between total heat transfers calculated by new suggested correlation and the experimental data

4.8 Conclusion

A new Euler-Eulerian method has been proposed to simulate the flow condensation inside a horizontal smooth tube. The default OpenFOAM solver called "reactingTwo-PhaseEuler-Foam" has been modified and a new library called "WallCondensation" has been added to this solver in order to represent the wall heat flux during condensation. The proposed model applied

the ideas of the partition functions used in recent boiling models. It split the condensing wall heat flux into two categories: the condensation heat flux and the single-phase convection. The condensation wall heat flux was considered to be a function of parameters such as the liquid density, liquid velocity adjacent to the wall, latent heat of vaporization and condensation area fraction. This last variable is a non-dimensional parameter that represents the fraction of the total wall area affected by the condensing vapor. By using reliable correlations and experimental data from the literature, a new relationship was proposed to estimate the condensation area fraction. The local and total heat transfer coefficient were calculated and numerical results were compared to experimental reference data taken from the works of Cavallini et al. [45] and of Suliman[46] . The performance of the suggested model was dependent on the flow regime and on the use of accurate correlations. Based on the sensitivity analyses performed with the numerical model, it was found that the condensation area fraction was dependent on the inlet mass flux, vapor quality, aspect ratio of the tube, saturation temperature and sub-cooled temperature. The effects of these parameters on the heat transfer coefficient was investigated and the following conclusions were drawn:

- Local heat transfer coefficient was enhanced by increasing the inlet mass flux and vapor quality.
- When the tube length and mass flux were constant, the total heat transfer coefficient was enhanced with a decrease of the hydraulic diameter.
- In stratified and stratified-wavy regime, the effect of the sub-cooled temperature on the total heat transfer coefficient was considerable. However, in annular flow, the mass flux was the main driving force influencing the heat transfer process.

Finally, a new and yet simple reliable relationship for the calculation of the total heat transfer coefficient was proposed by introducing a new variable called the condensation number. This simple relation, which is based on dimensionless numbers, had the same accuracy as Akers' correlation and produced reasonable results with errors of less than ±25%.

CHAPTER FIVE: Heat Transfer Analysis of Boiling and Condensation in Horizontal Heat Pipe

AVANT-PROPOS

Auteurs et affiliation:

- Roshanak Rabiee: étudiante au doctorat, Université de Sherbrooke, Faculté de génie, Département de génie chimique et de génie biotechnologique.
- B. Rajabloo, étudiant postdoctoral, Université de Sherbrooke, Faculté de génie, Département de génie chimique et de génie biotechnologique
- Martin Désilets: professeur, Université de Sherbrooke, Faculté de génie, Département de génie chimique et de génie biotechnologique.
- Pierre Proulx, professeur, Université de Sherbrooke, Faculté de génie, Département de génie chimique et de génie biotechnologique

Date d'acceptation:
État de l'acceptation: version finale publiée
Revue: International Journal of Heat and Mass transfer

Référence: Rabiee, R., B. Rajabloo, M. Désilets, M., Proulx, 2019. "Heat transfer analysis of boiling and condensation inside a horizontal heat pipe". International Journal of Heat and Mass Transfer, Volume 139, August 2019, Pages 526-536 [12].

Titre français: Analyse du transfert de chaleur en ébullition et en condensation à l'intérieur d'un caloduc horizontal

Contribution au document:

Cet article présente les résultats d'une combinaison de modèle d'ébullition et de condensation dans une étude de transfert de chaleur d'un caloduc. En outre, en effectuant une analyse de sensibilité, les performances de ce caloduc sont évaluées.

Une analyse du transfert de chaleur avec changement de phase, combinant ébullition et condensation, a été appliquée à un caloduc fermé. Des tests expérimentaux et une modélisation numérique ont été effectués sur des caloducs lisses horizontaux de type U, utilisant le R134a comme fluide de travail. Le caloduc consiste en un évaporateur de 180 mm, une section adiabatique de 280 mm et un condenseur de 180 mm de long. Le caloduc est fabriqué à partir d'un alliage d'aluminium et présente un rayon intérieur de 25,5 mm et un rayon extérieur de 33,6 mm. Des tests ont été effectués avec un taux de remplissage de 50% et en exposant l'évaporateur à différentes puissances, allant de 24 à 80 W. Un modèle numérique a été développé avec OpenFOAM pour évaluer les processus de transfert de chaleur lors de l'ébullition et de la condensation. L'un des défis les plus importants du modèle numérique est de prendre en compte l'effet couplé de l'ébullition et de la condensation dans un système fermé. Le travail numérique a été validé par des résultats expérimentaux. On peut en conclure que le modèle prédit de manière adéquate les caractéristiques des changements de phase dans diverses conditions de fonctionnement. En outre, une analyse de sensibilité réalisée à l'aide d'un modèle numérique est utilisée pour étudier l'effet de paramètres indépendants tels que l'apport de chaleur, le taux de remplissage, le diamètre du tube et le type de fluide frigorigène sur la résistance thermique équivalente, utilisée comme paramètre de performance du caloduc.

5 CHAPTER FIVE: Heat Transfer Analysis of Boiling and Condensation in Horizontal Heat Pipe

5.1 Abstract

A heat transfer analysis of phase change processes, combining boiling and condensation has been applied to a closed heat pipe. Experimental tests and numerical modeling have been carried out on U-type horizontal smooth heat pipe using R134a as working fluid. The pipe consists of a 180 mm evaporator, 280 mm adiabatic section and 180 mm long condenser. The heat pipe is fabricated from aluminum alloy and has a cross section of 25.5 mm and an outer radius of 33.6 mm. Tests have been conducted using a filling ratio of 50% and exposing the evaporator to different power inputs, ranging from 24 to 80 W. A numerical model has been developed with OpenFOAM to assess heat transfer processes during boiling and condensation. One of the most important challenges tackled with the numerical model is to consider both the coupled effect of boiling and condensation in a closed system. The numerical work has been validated by experimental results. It can be concluded that the model adequately predicts the phase changes characteristics at various operating conditions. In addition, a sensitivity analysis performed with numerical model is used to investigate the effect of independent parameters like heat input, filling ratio, diameter of tube and type of refrigerant on the equivalent thermal resistance, which is identified as heat pipe performance.

5.2 Literature review

The usage of different types of heat pipe in air conditioning systems, ventilation and heat removal systems has tremendously increased. Heat pipes are two-phase heat transfer devices and generating high heat flux with minimum temperature gradient and pressure drop. Lower service costs, due to the absence of mechanical parts, less occupied space and easier monitoring, manufacturing and maintenance are some of the advantages of using heat pipes. Such heat transfer device generally consists of an evaporator, condenser, adiabatic section and a working fluid, which undergoes a phase change process from liquid to vapor (boiling) in the evaporator and vapor to liquid (condensation) in the condenser. In other words, the working fluid rapidly absorbs large amounts of latent of heat from a heat source and releases it to the cooler side

without any mechanical parts. Heat pipes are highly effective thermal conductors due to the high heat fluxes obtained during boiling and condensation. To illustrate, the effective thermal conductivity of a heat pipe can approach 250 times greater than a copper rod with same dimension [72].

It is necessary to study what happens inside the evaporator and condenser sections in order to optimize the performance of a heat pipe. Various works in literatures concentrate on the analysis of boiling and condensation phenomena individually. For example, the numerical works of Michta [9], Ghione [10] have become known reference in modeling of flow and pool boiling. The experimental analysis of Cavallini [45] and Suliman [46] were performed to measure the heat transfer coefficient of flow condensation in horizontal tubes with different refrigerants like R134a, R32, R125 and R410a. Rabiee et al. [11] developed a new Euler-Euler model in OpenFOAM to simulate the flow condensation using available correlations in literature. The study of pool boiling and film condensation of R134a in an open system was performed by Wen-Tao et al. [39]. They used various enhanced tubes with different types of grooves to study boiling and condensation, separately. Groove types included integral fins, pyramid and re-entrant cavity. Based on their experimental work and on published literature, they mentioned that the re-entrant cavity has the best performance for boiling and condensation.

The combination of boiling and condensation inside the same heat exchanger like heat pipes definitely brings challenging difficulties to solve. This complexity is even more increased when the system is closed because of pressure variations in such applications. Among different types of heat pipes, thermosyphon or vertical wickless heat pipe has attracted the attention of many researchers. Consequently, there are numerous models for simulation of thermosyphon in open or closed systems. In the case of a thermosyphon, evaporator located below the condenser section, when heat is applied to the evaporator, the liquid is vaporized and flows upward to the condenser section. Vapor is then condensed on cooled walls and returns back to the evaporator section along the wall with the help of the gravity force.

Naresh et al. [7] carried out an experimental work to study the heat transfer performance of a thermosyphon in a closed system using R134a, acetone and water as working fluids. Their thermosyphon consisted of an evaporator, adiabatic and condenser sections with rectangular fins. They investigated the effect of condenser fins, mass flow rate of the cooling system, heat input (20-150 W) and filling ratio (20, 35, 50, 65, 80%) on the heat transfer. Their experimental

work showed that the optimum value for the filling ratio was 50%. The fins in the condenser improved the condensation performance by 13% and R134a had the lower thermal resistance compared to acetone and water at same conditions. In addition, they developed a lumped parameter model coupled with mass transfer equation and compared their numerical results with experimental measurements. Finally, they proposed a new correlation for the calculation of the heat transfer coefficient in the evaporator.

Bouhal et al. [73] and Fadhl [51] developed a CFD model for the simulation of phase changes in thermosyphon using the Volume of Fluid (VOF) method. They generated a user-defined function (UDF) in order to represent the phase changes and link it to an available phase change model in FLUENT. They compared their results including the vapor phase fraction, temperature and vertical velocity at different locations with the experimental work of Fadhl [51]. Based on some sensitivity analysis, they concluded that adding tilted fins in the condenser could increase the performance of thermosyphons.

Additional models and experimental works have been applied to other types of heat pipes like horizontal tubes, which is the main concern of this paper. In these heat exchangers, beside the evaporator, condenser and adiabatic sections, a wick structure is usually added to assist the liquid in returning back to the evaporator. When heat is applied, the working fluid absorbs latent heat and vaporizes. Then, the vapor moves to the condenser section driven by the pressure difference where it releases its latent heat to an external cooling system. Liquid then returns to the evaporator helped by capillary forces. Research studies for improving horizontal heat pipes can be generally divided into two categories: studies of different wick structures or type of grooves and studies on various working fluids.

Naresh et al. [52] reported experimental results of wickless heat pipe performance using self-rewetting fluids[4]. Substitution of these materials for water as common working fluids could prevent dry out of heat pipe at high heat input and give a better thermal performance. Kavusi et al. [74] developed a two-dimensional model to simulate the performance of a horizontal heat pipe using different nanofluids[5] (Al2O3, CuO and Ag) as working fluids. They mentioned that the substitution of water with nanofluids could facilitate the backing flow of liquid from condenser and finally reduce the thermal resistance of heat pipe by reducing its temperature.

[4] Dilute aqueous solutions of high carbon alcohols like butanol, pentanol and hexanol
[5] Some chemical particles that are added to the original working fluid

In experimental work of Mahdavi et al. [8], the heat transfer performance of a cylindrical copper heat pipe with water as working fluid was analyzed. Their setup consisted of an evaporator, condenser and adiabatic sections with a wick structure. The effect of filling ratio, inclination angle and applied heat on the equivalent thermal resistance of heat pipe were investigated. They concluded that, when the flow was gravity assisted, the inclination angle had no significant effect on the thermal resistance. However, when gravity was opposed to the system, the thermal resistance was also increased with increasing angle (90-180^o). Besides, high or low filling ratios had negative effects on the heat transfer performance. They also developed a numerical model in ANSYS and compared their results with their experimental measurements.

Abadi et al. [53] developed a numerical model to solve a conjugated problem of boiling and condensation in open system. The domain was a submerged tube inside of a pool filled with water. The fluid inside of submerged tube is R134a steam at saturation condition, which undergoes condensation process while pool boiling of water occurred outside of this tube. Such a system is typically used in passive heat removal applications. A 3-D Euler-Euler multiphase approach considering the effect of turbulent flow was solved using FLUENT. The effect of the tube orientation, steam mass flow rate and inlet steam quality on the heat transfer coefficient of condensation and pool boiling was investigated. They showed that the total heat transfer coefficient was maximum at an angle between 60^o -30^o. In addition, heat transfer coefficient could be improved by increasing the steam mass flow rate and its inlet quality.

Heat performance of U-type and L-type heat pipes were assessed in the experimental work of Wang [54]. A mathematical model was also developed to seek which configurations and geometries had the lowest thermal resistance. He concluded that the U-shaped heat pipe could dissipate 2.5 times more heat than the L-shaped one. The performance of different types of grooves in horizontal heat pipes using water as the working fluid was studied in the work of Khalili et al. [55]. They fabricated and tested two sintered wick heat pipes and compared the results with correlations from the literature. They analyzed the effect of the filling ratio and mode of operation on the thermal resistance of heat pipe. They concluded that gravity had negligible effects on the performance for wick horizontal heat pipes.

As mentioned before, there are several numerical and experimental works looking at the performance of thermosyphons. However, very few numerical works have been carried out on

horizontal heat pipes in a closed system in which boiling and condensation are present simultaneously. Such a situation leads to pressure oscillations that severely affect the stability of numerical models. The purpose of the present work is to show how the combination of experimental measurements and mathematical model developed with open-source CFD tools like OpenFOAM can be used to gain a better understanding of such systems. The experimental results are used to validate the numerical model for both the pool boiling and condensation sections of the U-type heat pipe. Furthermore, a parametric analysis conducted with the mathematical model using variables such as heat input, filling ratio, diameter of tube and type of refrigerants is done to predict their effects on the equivalent thermal resistance of the heat pipe.

5.3 Experimental works

In this study, the heat transfer analysis of boiling and condensation in closed system is performed on U-type smooth horizontal heat pipe consisting of a 180 mm long evaporator, a 180 mm condenser and a 280 mm adiabatic section. The inner and external radius of the tube are 25.5 mm and 33.6 mm, respectively. The test facility as presented in Figure 5-1 consists of heat pipe as test section, data acquisition system, computer, variable transformer as power supply, water tank storage and flowmeter. The evaporator section is heated by an electrical ribbon [75] and power can be adjusted by a variable transformer [76]. The vaporized fluid is transported via an adiabatic section to the condenser where heat is extracted by cooling water.

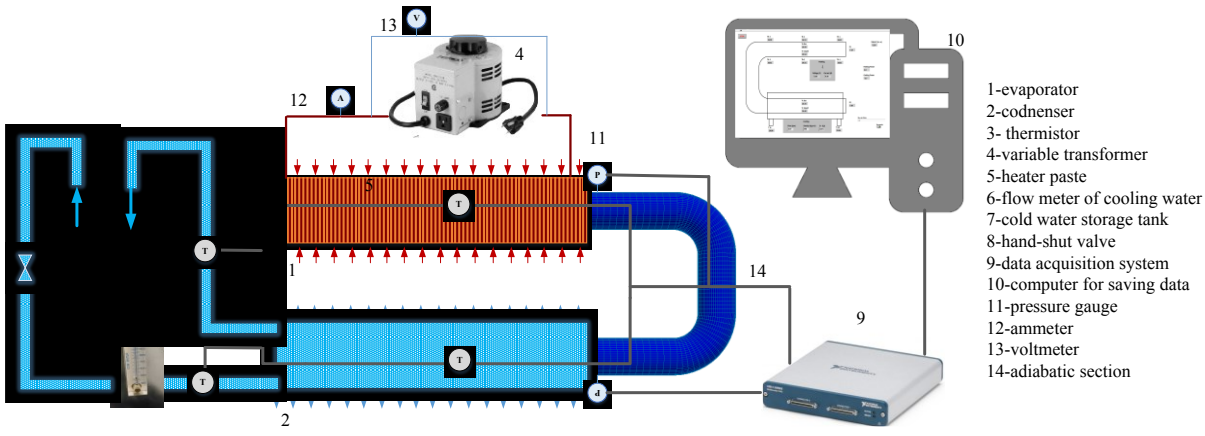

Figure 5-1: Schematic view of experimental test setup

The U-type heat pipe is fabricated from aluminum alloy and the whole structure is covered by multi-layer thermal insulation to minimize the heat losses. At the end of evaporator and

condenser, allowances are used to provide end caps for instrumentation and measurements. In fact, glass windows are mounted on each end to track bubble formation and observe flow and phase change phenomena during tests (see Figure 5-2).

It is necessary to clean heat pipe components because contamination can have negative effects on phase change processes. After cleaning and vacuuming the heat pipe, half of it filled with R134a refrigerant at a constant pressure. Internal pressure of the system is monitored for over 24 hours to be sure that no leakage is occurring. The system is then heated to reach saturated conditions whereby vapor and liquid can be considered in equilibrium conditions in evaporator and condenser. When such a situation is reached, it is time to start the measurements. For smooth heat pipe, the gravity force has a great effect on traversing fluid flow between the different sections of the heat exchanger. Thus, it is important to control the filling ratio and to make sure that the liquid level is uniform. For example, when the filling ratio is 50%, half of the channel must be filled with liquid, the rest being occupied by the vapor. Metal shims are used to equalize the liquid level inside different sections.

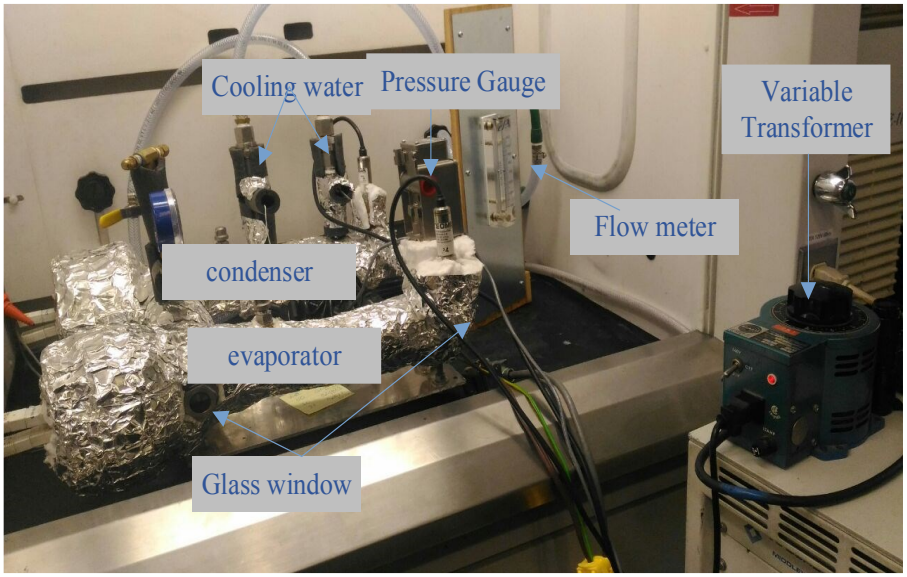

Figure 5-2: View of build-up experimental setup

5.3.1 Position of thermistors and accuracy of measurement data

Twelve calibrated thermistors are used in various positions (see Figure 5-3) for measuring the outside and inside temperatures heat pipe. Six thermistors (TH1, TH2, TH3, TB1, TB2, TB3) are attached to the evaporator's wall and two thermal sensors (TH4, TB4) are installed on

condenser's wall. Thermistors are strongly bounded to the wall surface. Four thermistors ($T_{top\text{-}evap}$, $T_{bottom\text{-}evap}$, $T_{top\text{-}cond}$, $T_{bottom\text{-}cond}$) are inserted inside the evaporator and condenser, far enough from wall, to measure the temperature of liquid and vapor, separately.

The heating ribbon is connected to a variable transformer and is wrapped around the evaporator wall to make sure it generates a uniform heat flux. A thermal paste is installed between the ribbon and the tube to guarantee a good thermal contact [77]. Uncovered space is left where thermistors are installed to avoid any measurement bias.

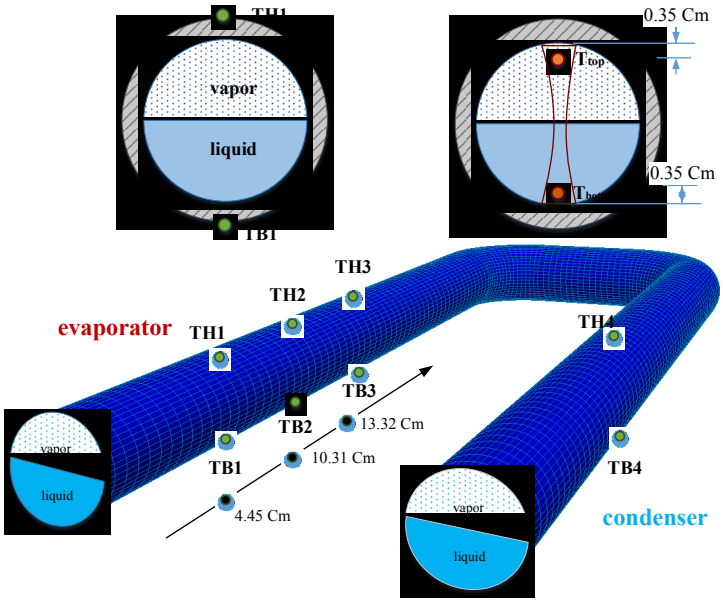

Figure 5-3: Position of thermistors in heat pipe

Cooling system is connected to a water storage tank and pump. Inlet mass flow rate is measured by a flowmeter [78]. The temperature of the water must be lower than the saturation temperature for condensation to happen. The system is designed in such a way that the mass flow rate of cooling water can be controlled by a hand shut valve. The temperature difference, needed for the calculation of heat losses, is measured by two thermistors installed at inlet and outlet. Two pressure gauges (±1000Pa) are inserted near the end of each section in order to measure the pressure inside the evaporator and condenser. The data acquisition system is programmed to prevent exceeding pressure or temperature conditions (Pressure < 8 bar, Temperature < 50 °C). The accuracy and uncertainty analysis of measurements are shown in TABLE 5-1. The uncertainty in electrical power σ_P can be calculated as [7]:

$$\sigma_P = \pm P\sqrt{(\frac{\sigma_v}{V})^2 + (\frac{\sigma_I}{I})^2} \quad (5.1)$$

Where σ_v and σ_I are accuracy of voltmeter and ammeter. Uncertainty in equivalent thermal resistance σ_R (Eq.5.17) is determined by the uncertainty of applied heat and temperature difference between evaporator and condenser [79]. Where σ_P and $\sigma_{\Delta T}$ are accuracy of power measured in Eq.(5.1) and accuracy of thermistor, respectively.

$$\sigma_R = \pm R\sqrt{(\frac{\sigma_P}{P})^2 + (\frac{\sigma_{\Delta T}}{\Delta T})^2} \quad (5.2)$$

TABLE 5-1: Uncertainty of measurement devices

Parameters	Uncertainty	Unit
Temperature (6-50 ^oC), σ_T	±1.0	^oC ,K
Pressure (6-8 bar)	±1000	Pa
Voltage, σ_V	±0.225	V
Current, σ_I	±0.025	A
Mass flow rate	± 25	mL/min
Power (80 W), σ_P	±0.887	W
Thermal resistance , σ_R	±0.031	K/W
σ_R/R (power 80 W)	±15%	---

5.3.2 Test procedure

The test is conducted for power inputs of 24, 60 and 80W. When a specific power is applied to the evaporator, the same energy is extracted by cooling system, a condition needed to obtain the thermal equilibrium and steady state where a balance of energy is satisfied in the whole system. The chosen power supply has the capacity of producing a current of 0-10 A in a voltage range of 0-140 V modulated with variable transformer to apply a uniform heat flux on the evaporator's wall [76].The extracted heat absorbed by the water cooling system varies depending on the mass flow rate, heat capacity of water and temperature difference between inlet and outlet.

Data acquisition system is connected to a computer to log and save test data including power input, temperature, pressure and water mass flow rate. All data is monitored and recorded in LabVIEW after reaching steady state conditions, typically obtained after a stabilization period of about 2 hours. Steady state condition is considered when the temperature change in thermistors is less than ±1.0ºC/hour. This procedure is repeated for all powers.

5.3.3 Results of experimental works

The presented wall temperature for the evaporator and condenser is the average temperature recorded by the thermistors installed at the top and bottom of wall.

$$T_{evap-wall} = \frac{T_{H1} + T_{H2} + \ldots + T_{B3}}{6}$$
$$T_{cond-wall} = \frac{T_{H4} + T_{B4}}{2} \qquad (5.3)$$

Eq. (5.4) shows how the power of evaporator and condenser was estimated.

$$Po_{evap} = V \times I \quad (W)$$
$$Po_{cond} = \dot{} \qquad \mathrm{T}_{w-in} - T_{w-out}) \quad (W) \qquad (5.4)$$

In above equation, V stands for voltage (V), I for current (A), $\dot{v}_w$ for volumetric flow rate of water (m^{-3}/s), ρ_w for water density and Cp_w for heat capacity of water (J/kg.K).Also, $T_{w\text{-}in}$,$T_{w\text{-}out}$ are the temperature of water at inlet and outlet respectively.

The phase change study in evaporator and condenser is investigated using R-134a as a working fluid with a filling ratio of 50%. For the first test case at 24 W, the mass flow rate of cooling water is manually adjusted to satisfy conservation of energy. The properties of R134a at saturation condition and water in cooling condition is shown in TABLE 5-2.

TABLE 5-2: Properties of refrigerant at saturation point and properties of water at cooling conditions

Properties	Value	Unit
Type	**R-134a**	**---**
Saturation temperature	297	K
Saturation pressure	6.38	bar
Density of liquid	1210	kg/m^3
Density of vapor	32.3	kg/m^3
Latent heat of evaporation	1.78	kJ/kg
Specific heat of liquid	1.42	kJ/kg.K
Specific heat of vapor	1.02	kJ/kg.K
Thermal conductivity of liquid	0.083	W/m.K
Thermal conductivity of vapor	0.014	W/m.K
Dynamic viscosity of liquid	1.99×10^{-4}	Pa.s
Dynamic viscosity of vapor	1.21×10^{-5}	Pa.s
Type	**water**	**---**
Temperature	291	K
Specific heat	4186	J/kg.K
volumetric flow rate	1.16×10^{-5} (700)	m^3/s (mL/min)

The temperature vs time graph for the first case (24 W) is shown in Figure 5-4. As the reader can see, the wall temperature is reaching to a steady state after 40 min. When the heat is applied to the evaporator, the saturated liquid vaporizes and the pressure of the evaporator increases due to accumulation of vapor at the top section. Therefore, vapor flows towards the condenser where it condenses to liquid at the contact of the cooled walls maintained at a temperature below saturation point. The liquid film at top section of the condenser falls down to bottom liquid filled section where it returns to the evaporator section. The vapor and liquid circulate continuously between evaporator and condenser due to gravity force and pressure difference, which results in a merely constant filling ratio in the whole system.

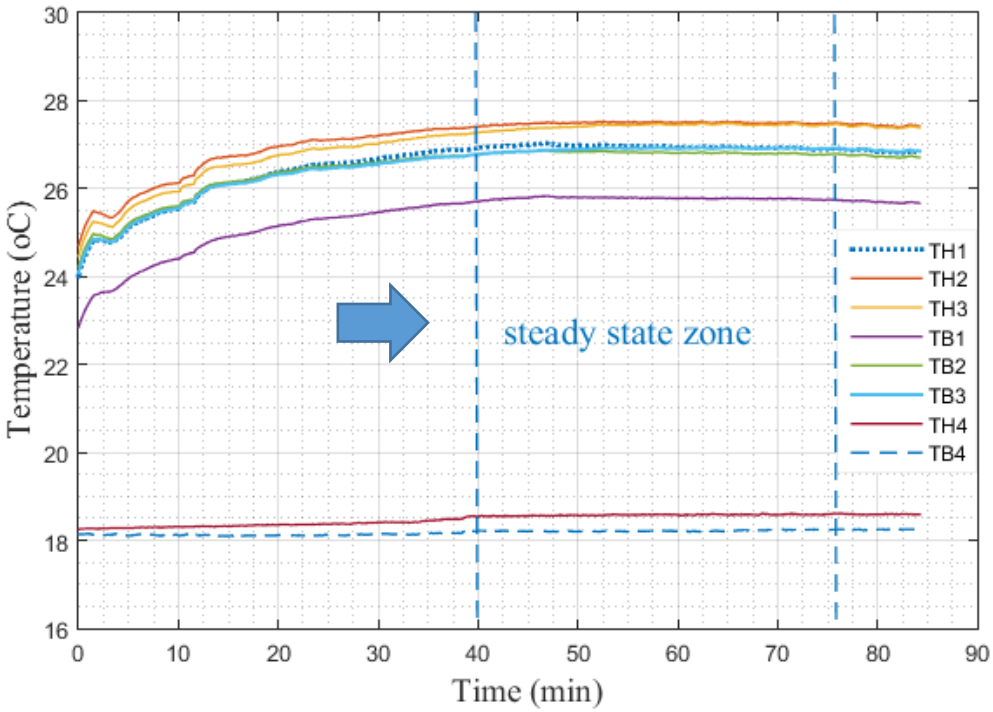

Figure 5-4: Temperature history of wall power 24W- case I

For higher power, like 60 and 80 W, phase change is even more effective and quickly happened at the evaporator and condenser. Also, the liquid level is not considerably influenced by the power. In these cases, the system reaches the steady state sooner and its response time is less than 20 min (Figure 5-5, Figure 5-6).

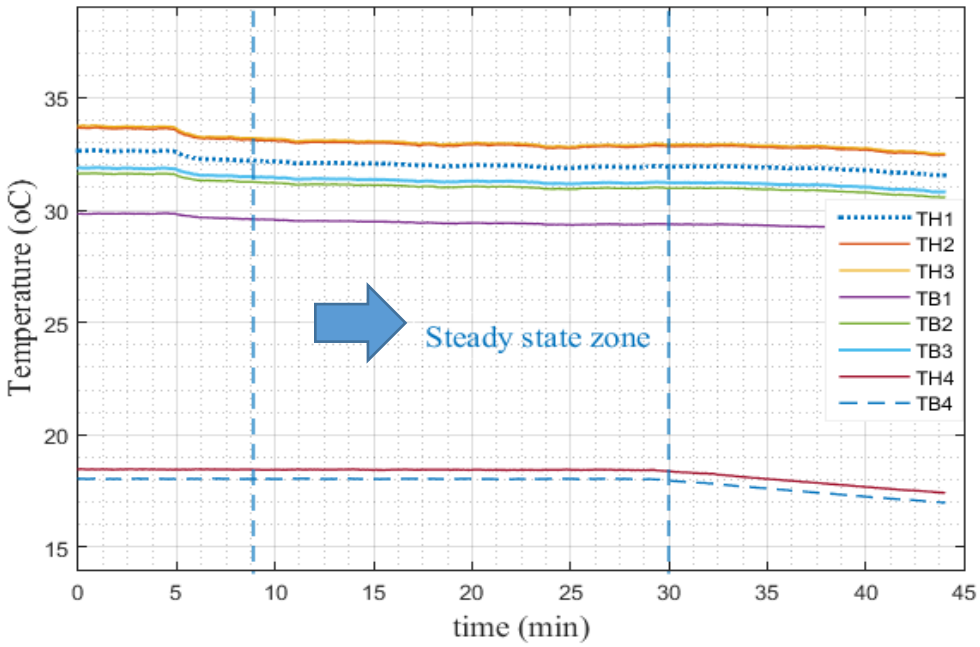

Figure 5-5: Temperature history of wall for case II (power=60W)

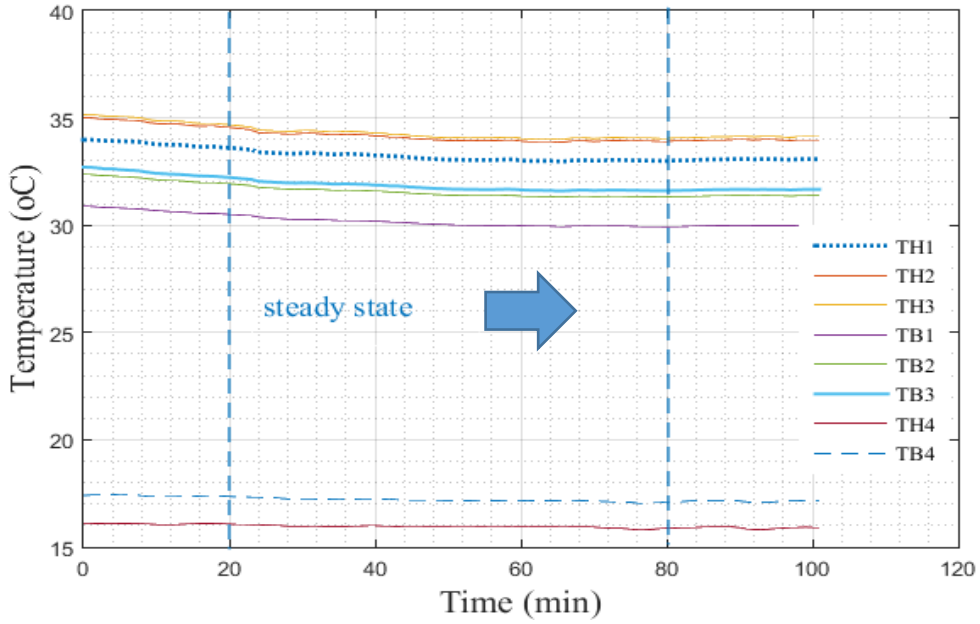

Figure 5-6: Temperature history of wall for case III (power=80W)

5.4 Mathematical formulation

5.4.1 Governing equation

The numerical model based on OpenFOAM solver is chosen to study the various heat transfer processes in the horizontal heat pipe. The solver uses an Euler-Euler method for modeling the compressible, turbulent flow and is capable of modeling phase change in boiling and condensation. A compressible model is chosen because it not only represents low Mach number flow but also gives more stability to numerical model. In Euler-Euler models, each phase is considered as a continuous phase and the governing equations including continuity, momentum and energy are separately solved for each phase. Since the other governing equations are comprehensively introduced in our previous article [11], only the energy equation is described in this paper, with a focus on important parameters for modeling phase changes.

The energy equation for the two-phase model is:

$$\frac{\partial(\rho_a \alpha_a i_a)}{\partial t} + \nabla.(\rho_a \alpha_a i_a \vec{\upsilon}_a) = -\nabla.[\alpha_a (q_a + q_a^t)] + (\Gamma_{ab}^{+} i_b - \Gamma_{ba}^{+} i_a) + q_{wall}^{"} A_{wall}^{"} \quad (5.5)$$

where i_a stands for the specific enthalpy of phase a, α_a for the phase fraction of a, $(q_a + q_a^t)$ for the molecular and turbulent heat flux inside phase a and $\Gamma_{ab}^{+} i_b - \Gamma_{ba}^{+} i_a$ for the source term added to the energy equation due to the mass transfer between phases (phase *a, b*) [10]. The last term in the energy equation describes $A_{wall}^{"}$, the contact area with the wall per unit volume and $q_{wall}^{"}$, the wall heat flux that is the main energy input of the heat pipe.

5.4.2 Boiling Model

In modeling of phase changes processes like boiling and condensation that occur at the boundaries of the domain, the wall heat flux is an important term that must be accurately modeled. The implemented solver based on model of Kurul et al. [60] called "*reactingTwoPhaseEulerFoam*" is used and this solver is available in versions OpenFOAM 4.0 and newer. Based on this proposed model, the heat transfer between the heated wall and the liquid originates from three different mechanisms as described below:

$$q_{wall}^{"} = q_{wall}^{c"} + q_{wall}^{e"} + q_{wall}^{q"} \quad (5.6)$$

Where $q^{c"}_{wall}$ represents the single-phase convection heat flux, $q^{e"}_{wall}$ the evaporation heat flux and $q^{q"}_{wall}$ the quenching heat flux (Figure 5-7). Vaporization of the liquid lead to the formation of bubbles at the wall nucleation sites; this part of the heat flux is directly related to the evaporation flux. When a bubble detaches from the wall, the colder surrounding liquid replaces the volume occupied by the bubble, which creates a heat flux called quenching. The rest of the wall area that is not covered by any bubbles is used for single-phase convection of liquid phase [60]. The focus has been put on the dominant term of evaporation heat flux; modeling of quenching heat flux and single-phase convection was introduced in a previous paper [11] .

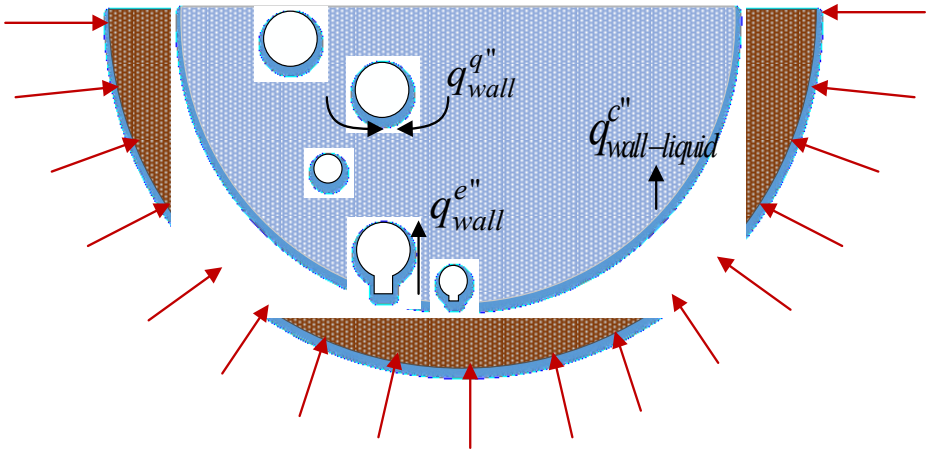

Figure 5-7: Wall boiling model consisting of evaporation, quenching and single-phase convection

The evaporation heat flux is a function of some important parameters such as the boiling area fraction A_b, latent heat of vaporization, density and velocity of the vapor.

$$q^{e"}_{wall} = \dot{\imath} \qquad , \quad) \quad (5.7)$$

where $\dot{\imath}$ and h_{lv} are the mass flux generated by evaporation and the latent heat of vaporization, respectively. $U_{adj.v}$ is the velocity of vapor or bubbles near the wall. It is a function of the frequency of detachment f and diameter of the detached bubble d_w [11].

$$\mathrm{U}_{adj.v} = f \times d_w \qquad (5.8)$$

In the above equations, the important term is A_b, a non-dimensional number called the boiling area fraction. It represents the ratio of the wall area wetted by bubbles to the total area of wall. Different models are proposed for the calculation of the boiling area fraction, but the most

known reference is Lemmert [63] who suggested the following correlation for the boiling area fraction as a function of temperature difference between the wall and the saturation temperature (superheat temperature):

$$A_b = \pi \times 5.18 \times 10^{-2} \times [\frac{T_{wall} - T_{sat}}{10}]^2 \times \exp[-\frac{(T_{sat} - T_l)}{45}]^2 \quad (5.9)$$

Constant numbers, such as 5.18×10^{-2} (m^{-2}), *10 (^oC)* and *45*(^oC) used in the previous equation, are dimensional units and come directly from empirical data in [63] and [62]. As mentioned in these references, these constants are the most suitable for modeling the boiling of R134a.

5.4.3 Condensation Model

In OpenFOAM solver (reactingTwoPhaseEulerFoam), there is no model for the simulation of pool condensation. The idea of previously described boiling model is adapted to the physic of pool condensation with help of experimental results. In our proposed thermal model, the condensation wall heat flux can be divided into two main contributions called the single-phase convection of vapor, $q^{c"}_{wall}$ and the condensation heat flux, $q^{cd"}_{wall}$ as shown in Figure 5-8. The concept of quenching heat flux is not applicable in the condensation case. When a vapor at saturation conditions gets in contact with a colder wall at a temperature below the saturation, a portion of the wall gets wetted by the formation of condensing droplets. The rest of the wall is affected by the single-phase convection of vapor [11], which can be represented by the following equation:

$$q^{c"}_{wall} = (1 - A_{cd}) H_{c,\mathrm{v}} (\mathrm{T}_{wall} - T_v), \quad (\mathrm{W/\,m^2}) \quad (5.10)$$

where $H_{c,\mathrm{v}}$ is the Stanton heat transfer coefficient of single-phase convection, calculated from the Stanton Number [9] using the vapor properties.

The condensation heat flux can be presented in a similar form to the evaporation heat flux:

$$q^{\mathrm{cd"}}_{wall} = i \cdot \qquad \cdot \qquad _{adj,l}) \quad (5.11)$$

In the above equations, A_{cd} is a non-dimensional parameter called the condensation area fraction, which represents the fraction of the wall area wetted by liquid droplets of condensing vapor to the total area of the wall *($0 < A_{cd} < 1$)*. Finally, $\mathrm{U}_{adj,l}$ is the velocity of the liquid droplet

adjacent to the wall, a flow variable with the same order of magnitude of vapor velocity (Eq.5.8).

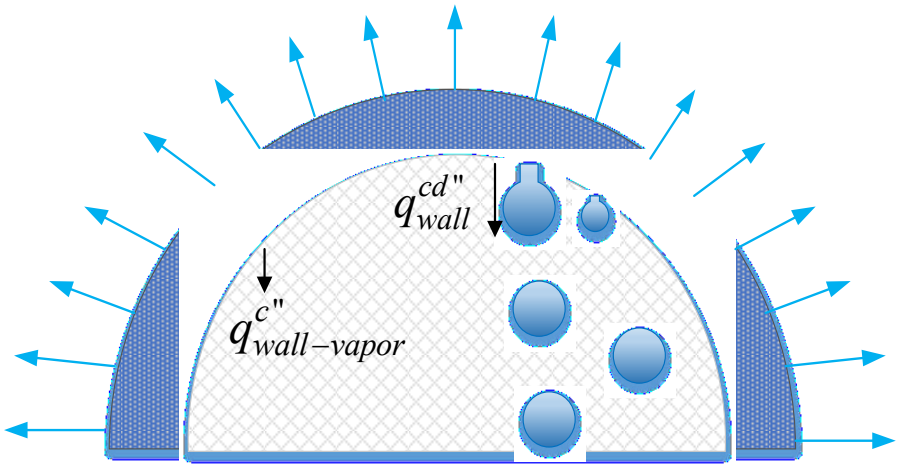

Figure 5-8: Wall condensation model consists of condensation heat flux and single-phase convection

In a previous work [11], flow condensation was studied where A_{cd}, a function of the mass flux, subcooled temperature and Reynolds number, was estimated from reference correlations. In pool condensation however, the physics is different since the flow is stationary and the area fraction is only function of the temperature difference between the wall and saturation (subcooled temperature). There is no known model for the calculation of area fraction in pool condensation. In this paper, the following relation is suggested for the calculation of this parameter:

$$A_{cd} = \pi N''(d_w^c)^2 \qquad (5.12)$$

Where d_w^c is diameter of detached liquid droplet calculated by using vapor properties in reference [62] to represent condensation.

$$d_w^c(T_{sat}, T_v) = 0.0006 \times \exp[-\frac{T_v - T_{sat}}{45}] \qquad (5.13)$$

N'' called nucleation site density, such sites act as a nest for condensing vapor. The Eq.(5.14) is proposed for estimation of nucleation site density:

$$N''(T_{sat}, T_{wall}) = a \times ([\frac{T_{sat} - T_{wall}}{T_{ref}}])^b \qquad (5.14)$$
$$a = 3833.33(m^{-2}), b = 1.805, T_{ref} = 10^o C$$

The optimum value for constant numbers *a* and *b* in Eq.(5.14) are estimated through a parametric analysis conducted to get the lowest mean error between the numerical and experimental results. The final form of the condensation area fraction is presented in Eq. (5.15) and the following constants *1.38×10^{-3} (m^{-2}), 10 (^{o}C) and 45 (^{o}C)* are dimensional units.

$$A_{cd} = \pi \times 1.38 \times 10^{-3} \times [\frac{T_{sat} - T_{wall}}{10}]^{1.805} \times \exp[-\frac{(T_v - T_{sat})}{45}]^2 \quad (5.15)$$

5.5 Validation of Numerical model

The wall domain is not included in the presented analysis to decrease the complexity of the model and avoid treating a conjugate heat transfer problem. The geometry with uniform 3-D hexahedral mesh is illustrated Figure 5-9. A viscosity sublayer is added at the boundary to have a better estimation of wall function parameters. Since the adiabatic section does not affect our numerical work, we decrease its size from 0.28 to 0.2 m.

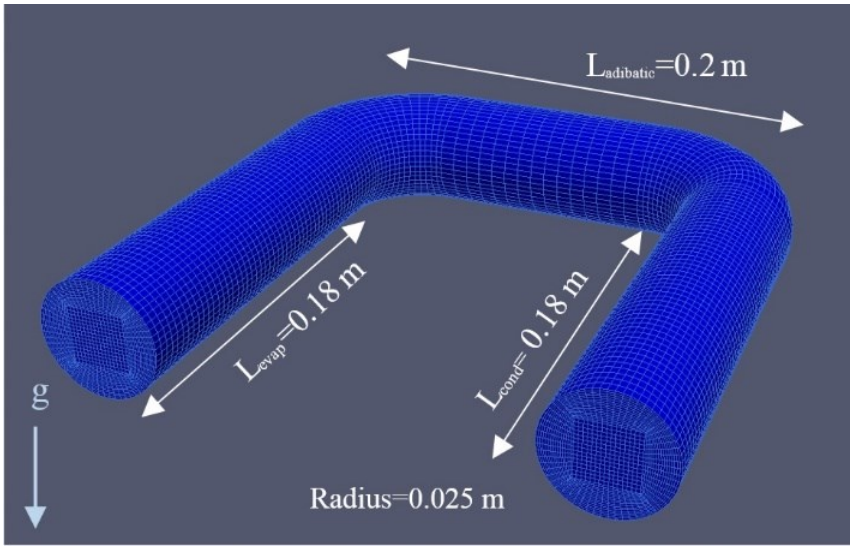

Figure 5-9: 3D-hexahedral mesh and gravity direction

The optimum number of cell in different directions is selected to keep the lowest mean error, computational time and best convergence. The results of grid sensitivity TABLE 5-3 are shown the mean error for equivalent thermal resistance, calculated between the experimental and numerical results (see Eq.5.16).

TABLE 5-3: Grid sensitivity analysis

Cell number	Grid type	Mean error value %
85164	Coarse	5.299
144287	Medium	2.641
221897	Fine	2.409

5.5.1 Boundary conditions and numerical model

The new OpenFOAM solver is enthalpy-based and uses an Euler-Euler approach in which each phase is considered as a continuum phase. Consequently, each variable such as velocity, temperature, and volume fraction is considered for both phases (continuous or dispersed phase). This work is focused on steady state predictions. The developed model is not aiming at predicting the transient behavior of the heat pipe. Since the initial conditions do not affect the final solution but still can influence the convergence speed, they are chosen in such way to reach steady state with a minimum number of iterations. The initial pressure and temperature of the vapor and liquid phases are set close to the final equilibrium condition that is expected to be reached. The boundary conditions and geometry considered in the numerical model are presented in in TABLE 5-4. There is no inlet nor outlet in the heat pipe, the domain's boundary is defined as walls and a no slip boundary condition is applied for the velocity of vapor and liquid. For the pressure at wall, a *fixedFluxPressure* boundary is chosen that acts as a zero gradient condition. In the evaporator, the modified wall function library called "*WallBoiling*" is added to liquid phase. Conventional convection boundary condition is selected for vapor phase. In the condenser, the proposed "*WallCondensation*" library is added to vapor phase while convection is considered as the primary mechanism of heat transfer for liquid phase. Instead of constant temperature, a constant heat flux library called "*fixedMultiPhaseHeatFlux*" is used. With help of this library, a constant heat flux applied at walls and then its temperature is read and compared with experimental results. A zero heat flux is defined as the thermal boundary condition for the adiabatic section The simulations are performed using a very short time-step (approximately 10^{-10} s), to improve the convergence of the model. Calculations are carried on until the steady state is reached.

TABLE 5-4: Properties and geometry of numerical simulation

Parameters		Value
Refrigerant		R-134a
Hydraulic Radius (m)		0.025 m
Length of evaporator condenser		0.18 m
Length of adiabatic section		0.2 m
Surface area (evap. & cond.)		2.87×10^{-2} m^2
Filling ratio		50 %
Wall heat flux		
P_o=±24 W	Case I	q=835W/m^2
Saturation temperature		24 °C
Saturation pressure		6.38 bar
P_o=±60 W	Case II	q=2090 W/m^2
Saturation temperature		27 °C
Saturation pressure		7.01 bar
P_o=±80 W	Case III	q=2787 W/m^2
Saturation temperature		28 °C
Saturation pressure		7.04 bar

In order to consider the effect of interfacial momentum in our model, drag and virtual mass forces are added to the momentum equation since they have higher effects than all other forces like wall lubrication, lift and turbulent dispersion. In addition, a constant diameter model has been chosen for the calculation of dispersed phase's diameter. The variation of the saturation pressure with temperature has been taken into account by using a cubic polynomial approximation (Figure 5-10). The stability of numerical model depends on the precision of this equation. The mixture k-ε turbulence model is used to simulate the turbulence effects on both continuous and dispersed phase.

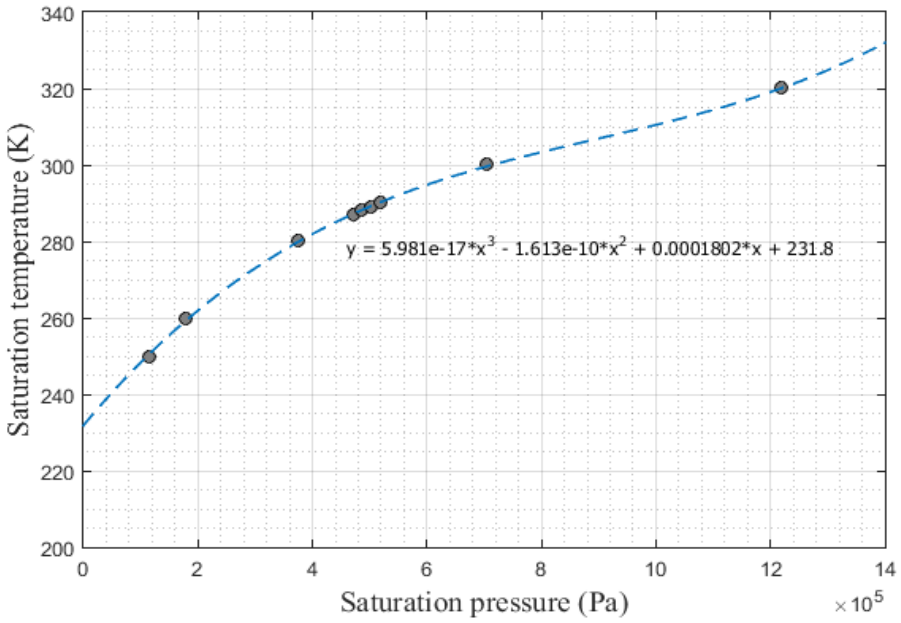

Figure 5-10: Polynomial relation between saturation pressure and temperature for R134a

The algorithm PISO is used to represent the coupling between velocity and pressure. A combination of Gauss-upwind, Gauss linear and Gauss limited linear schemes is selected for the discretization of the spatial derivatives. For the time derivative, the first order Euler implicit method is applied.

5.6 Results and Discussion

In order to validate the numerical model, the predictions are compared with experimental measurements. All quantities in numerical column corresponded to actual simulation results after reaching to steady state. In TABLE 5-5 important parameters such as pressure, power, heat flux, temperature at steady state condition are presented for three cases described in details in section 5.3 and characterized by their input power of 24, 60 and 80 W, respectively. The mean error of each parameters is calculated from a relation similar to the one used for parameter X.

$$Error_{mean} = \frac{(|X_{num} - X_{\exp}|)}{0.5 \times (X_{num} + X_{\exp})} \times 100 \qquad (5.16)$$

In the case of temperature, T_{num} is calculated as the average value of all control volumes at wall and T_{exp} is calculated based on the average value of all thermistors (Eq.5.3). As results of TABLE 5-5 are showing, the balance of energy is satisfied in the numerical model. The lowest errors are found for the prediction of power, heat flux and temperature, and the highest error is

attributed to pressure. It might be due to the oscillation of pressure, which is more important in a closed and coupled system, like in heat pipes where evaporator and condenser are influencing each other. This source of oscillation in numerical answer degrades the accuracy of results, especially at high power. Moreover, in numerical models using Euler-Euler method, the same pressure value for both phases is considered in the whole system which adds some constraints to the resolution.

Another source of error can be related to pressure measurements. In fact, the pressure difference between evaporator and condenser is very low (about less than 1000 Pa).

It is critical to use a high precision pressure transducer to capture this pressure difference. The discrepancy between experimental and simulation results are more obvious at high power when changes in pressure and temperature are considerable. However, an error of less than 3% is still acceptable for pressure. The error in temperature is related to the accuracy of thermistors (T±1.0 K). Therefore, a difference of 1 to 2 degrees between numerical and experimental values is acceptable.

TABLE 5-5: Comparison between numerical estimation with experimental

	Case I			**Case II**			**Case III**		
Parameters	Experimental	Numerical	Mean error %	Experimental	Numerical	Mean error %	Experimental	Numerical	Mean error %
	Evaporator								
Pressure (bar)	6.39	6.33	0.786	6.96	6.94	0.287	7.33	7.11	3.047
Power (W)	24	23.95	0.209	60	59.90	0.166	80	79.85	0.250
Heat flux (W/m^2)	835	834.1	0.108	2090	2086.3	0.177	2787	2781.2	0.208
T_{sat} (K)	297.3	297.1	0.063	300	299.8	0.066	301	300.6	0.133
T_{wall} (K)	300	299.5	0.168	304	303.5	0.164	305	304.8	0.065
	Condenser								
Pressure (bar)	6.38	6.33	0.946	6.96	6.94	0.287	7.32	7.11	2.910
Power- (W)	-24	-23.96	0.418	-60	-59.98	0.166	-80	-79.98	0.125
Heat flux (W/m^2)	-835	-834.7	0.036	-2090	-2088.9	0.052	-2787	-2785.5	0.053
T_{sat} (K)	297	297.1	0.033	300	299.8	0.066	301	300.6	0.133
T_{wall} (K)	291	291.2	0.068	290	288.9	0.380	290	287.4	0.900

5.6.1 Temperature distribution analysis

The variation of predicted temperatures versus heat input is compared with experimental values (at steady state condition) in Figure 5-11. According to these results, it can be concluded that the numerical model satisfyingly predicts the saturation and evaporator temperatures. However, the condenser wall predictions are slightly deviated from experimental value at higher heat inputs. The error might be associated to proposed model for the condensation area fraction. As mentioned before, there is no validated and reliable relation for the prediction of A_{cd} in the open literature. Thus, inevitable errors are expected, especially at higher heat flux when the variation in flow parameters like pressure are significant. The accuracy of the proposed model could be improved by relying on more experimental data.

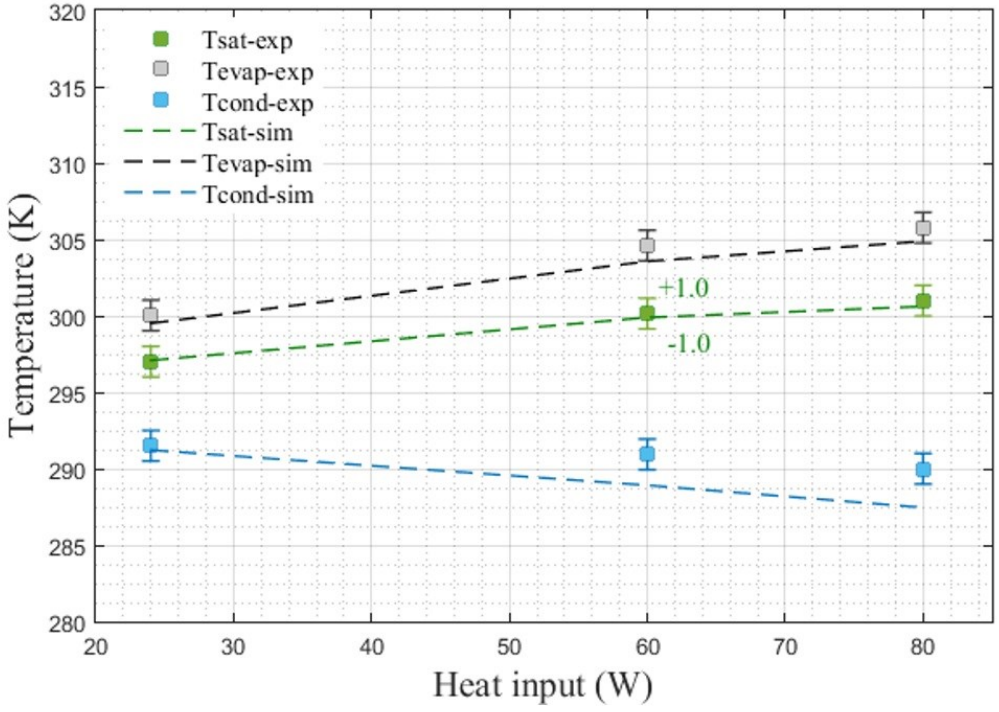

Figure 5-11: Temperature distribution versus heat input, a comparison between numerical model and thermistors measurements

5.6.2 Heat pipe performance analysis

The performance of the heat pipe is typically estimated from the heat transfer coefficient or thermal resistance. The equivalent thermal resistance is characterized by the temperature difference between evaporator and condenser divided by power of evaporator or condenser ([7], [8]). The equivalent thermal resistance is calculated as following equation:

$$R_{equiv} = \frac{(T_{evap-wall} - T_{cond-wall})}{P_{evap} = P_{cond}} \rightarrow R_{equiv} = \frac{1}{(\pi DL_{evap} + \pi DL_{cond})h_{equiv}} \quad (5.17)$$

Beside the equivalent thermal resistance, one can define the thermal resistance of the evaporator and condenser, individually.

$$R_{evap} = \frac{(T_{evap-wall} - T_{sat})}{P_{evap}}$$
$$R_{cond} = \frac{(T_{sat} - T_{cond-wall})}{P_{cond}} \quad (5.18)$$

Where T_{wall} is the average value of all thermistors around wall. In the numerical results, the wall temperature is taken as the average value of all control volumes at the walls. The results of numerical thermal resistance for cases I, II and III are presented in Figure 5-12 using an error band of ±15%. They show a good agreement with experimental data, which confirms the accuracy and reliability of the proposed model. The highest deviation is obtained in case III where an error of about 18% can be observed. As presented the data for evaporator and condenser separately, it is observed that the source of error is related wall temperature distribution in condenser. As mentioned in the previous section, the proposed model for condensation generates inevitable errors due to the lack of experimental data. Moreover, an analysis of the results reveals that the evaporator thermal resistance is lower than condenser. It means that boiling is more effective than the condensation process.

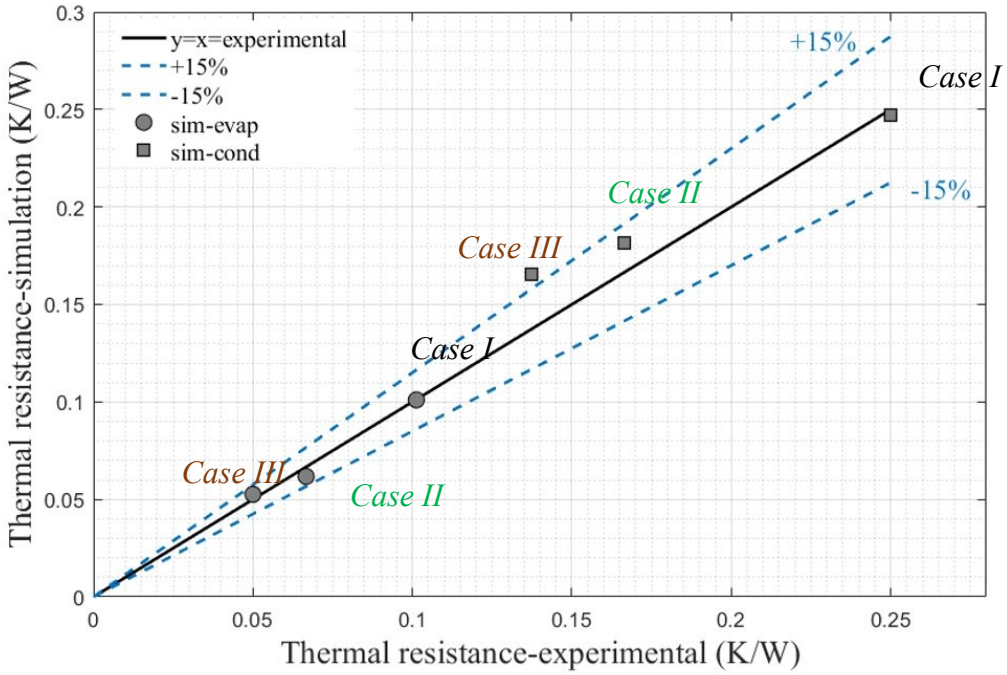

Figure 5-12: Evaporator and condenser thermal resistances: experimental versus numerical values

5.7 Parametric analysis, optimization of model

After the validation of the proposed numerical model, a parametric analysis is performed to investigate the effect of the main independent variables on the heat pipe performance. The important parameters that affect the equivalent thermal resistance are the filling ratio, diameter of tube, length of tube, type of refrigerant and heat input. The cooling mass flow rate has the same effect as the heat input so it is not considered in this work.

5.7.1 Effect of heat input on heat pipe performance

The effect of the heat input on the thermal resistance has first been evaluated and presented in the following graphs. Applied heat at boundary is changed from 10 to 150 W keeping the same geometry, saturation condition and filling ratio at 50 %.

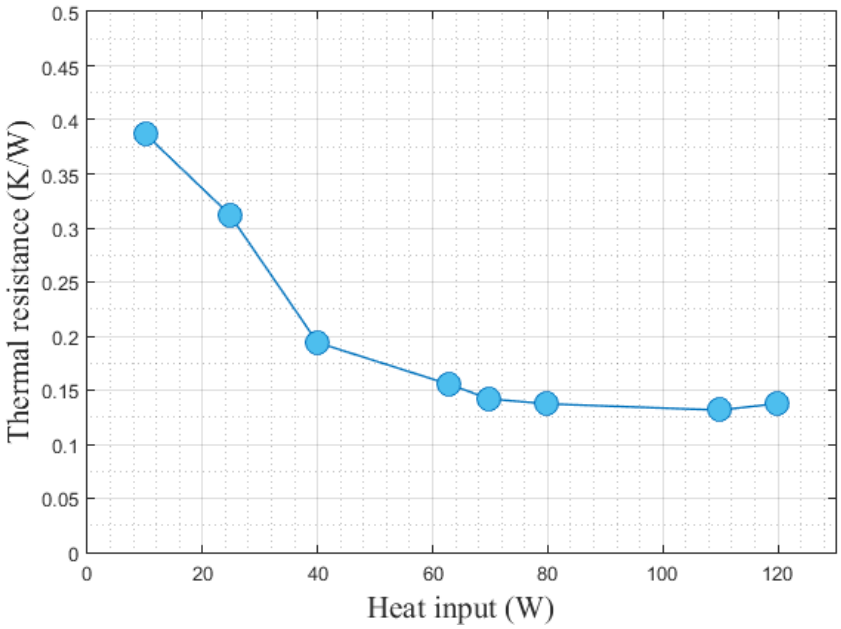

Figure 5-13: Effect of heat input on equivalent thermal resistance

Figure 5-13 shows that the thermal resistance is highest at the lowest heat input and lowest at the highest heat input. Heat transfer in heat pipe is driven by phase change mechanisms and forced convection. Boiling and condensation are the most effective processes since they generate a very high heat flux with minor temperature gradients. In other words, they have high heat transfer coefficients or low thermal resistances. At the lowest heat input, boiling or condensation are weakly expressed with the consequence that thermal resistance is enhanced. When the applied heat is increased, phase change gets more effective resulting in a decrease of the thermal resistance. The same trend is also reported in [8] and [80]. Another observation can be made from Figure 5-13 is that the slope of the thermal resistance is initially sharp up to 60W. Beyond this point, it levels off to an almost constant value of 0.15 K/W. It demonstrates that the heat pipe is best exploited at higher heat input.

5.7.2 Effect of filling ratio on heat pipe performance

The filling ratio is defined as the ratio of liquid volume to the total volume. Previous numerical analysis have been performed for a filling ratio of 50% i.e. when half of the channel is occupied with liquid and the rest filled with vapor. In order to estimate the effect of filling ratio on thermal resistance, five filling ratios of 20, 30, 50, 65, 80% are chosen. All other parameters, like saturation condition, geometry and heat input flux, are kept constant.

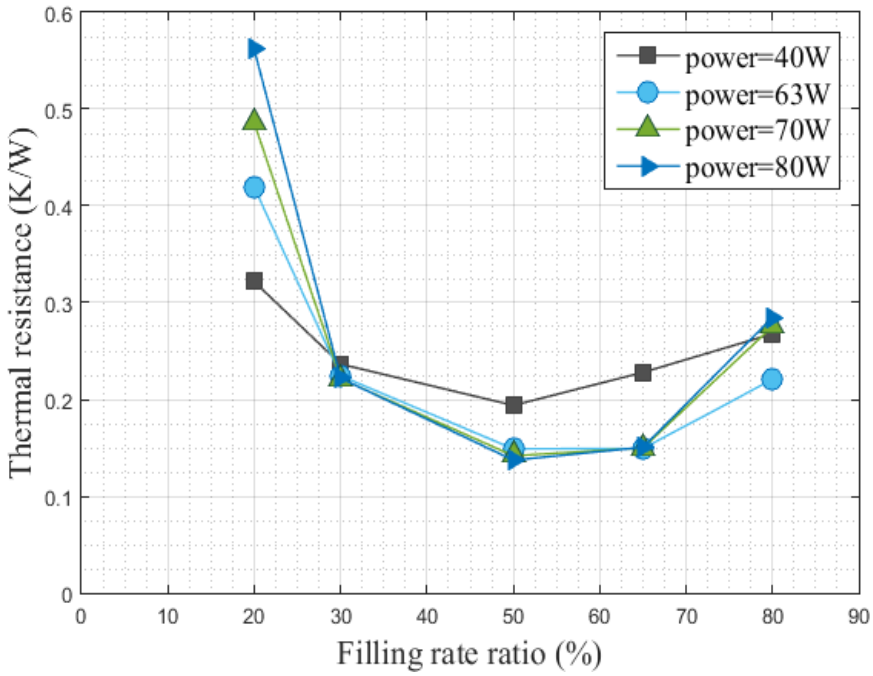

Figure 5-14: Effect of the filling ratio on equivalent thermal resistance

The results show that optimum values for the thermal resistance or heat transfer rate is found around 50%. As seen in Figure 5-14, for a given heat input, the thermal resistance decreased from a filling ratio of 20-50% and subsequently increased in the 50-80% range. At the lowest filling ratio, when the proportion of liquid is less than vapor, the evaporator starves for liquid and boiling is not effective anymore. Therefore, convection becomes the prevailing mechanism for heat transfer resulting in high temperature difference or high thermal resistance. This situation can become critical at the highest heat input where the thermal resistance gets extremely high. When the filling ratio is increased from 50 to 80%, the condenser efficiency is degraded causing an increase in the wall temperature. Highest temperature gradients between wall and saturation lead to higher thermal resistance and lower heat transfer coefficient.

From Figure 5-14, one can also observe that the decrease of thermal resistance is more rapid in the low range of filling ratios (below 50%). As mentioned before, at lowest filling ratio, convection heat transfer is more effective than boiling heat flux. Since vapor has a lower heat capacity (C_p) than liquid, the temperature gradient in the evaporator is raised leading to a higher thermal resistance. The similar behavior is observed in the work of [7] and [79].

5.7.3 Effect of diameter of channel on heat pipe performance

Diameter and length of the tube are two other important parameters, that affect surface area, and consequently may increase or decrease the thermal resistance. In order to simplify the analysis, the length of evaporator and condenser is kept constant and the diameter of the tube is changed from 2 cm to 5 cm, by steps of 1 cm.

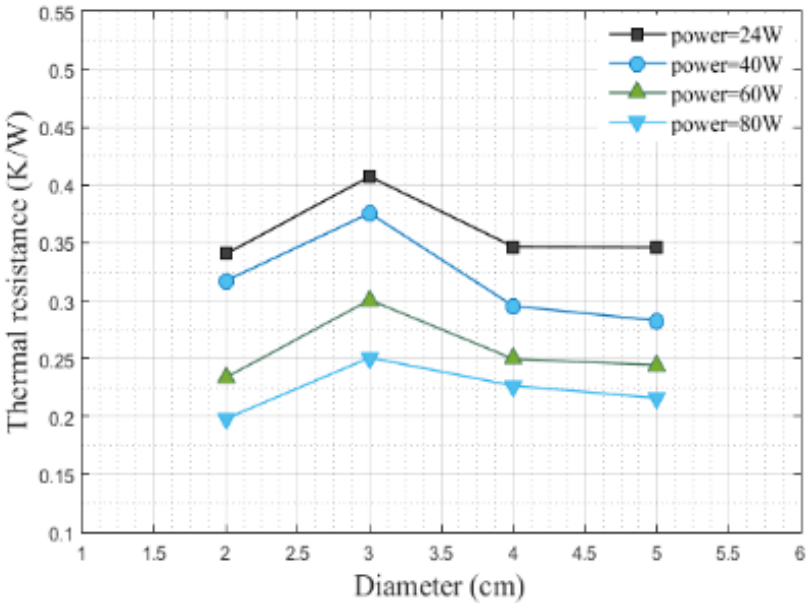

Figure 5-15: Effect of the diameter of tube on the equivalent thermal resistance for filling ratio 50% at different powers

Figure 5-15 shows the variation of the thermal resistance with the diameter of heat pipe at different heat inputs. According to the obtained results, changing merely the diameter or the surface area does not help to increase the heat pipe performance and thus the thermal resistance is almost constant. Two opposing phenomena apparently take place. On one hand, when the diameter of the tube is increased, the effective area for heat transfer is also enhanced, the thermal resistance in the heat pipe is decreased. This aspect might be seen in the evaporator where the thermal resistance is decreased when diameter is increased. On the other hand, the condenser, which is coupled with the evaporator, counteracts the global performance. In fact, the rate of condensation is considerably decreased in the condenser in such a situation. Consequently, equivalent thermal resistance is maintained constant and no improvement are globally seen in the heat pipe performance.

One must remember that the surface augmentation generated for instance by grooves can differently affect heat pipe performance. Grooves or cavities on the surface can act as a nest for bubbles and increase boiling rate. Moreover, they facilitate backing flow from the condenser to the evaporator and consequently they can improve the condenser performance. Therefore, the heat pipe performance can be improved by surface augmentation.

5.7.4 Effect of the type of refrigerant on the heat pipe performance

In this section, the effect of different types of refrigerant on the heat pipe thermal resistance is investigated. Three conventional refrigerants, R22, R410 and R134a, are selected. There are some refrigerant as R11 and R12 which were banned to use in heat pipe application because they have high depleting zone potential [79]. Heat transfer analysis at constant saturation conditions, power and geometry is performed to find which refrigerant brings the best performance.

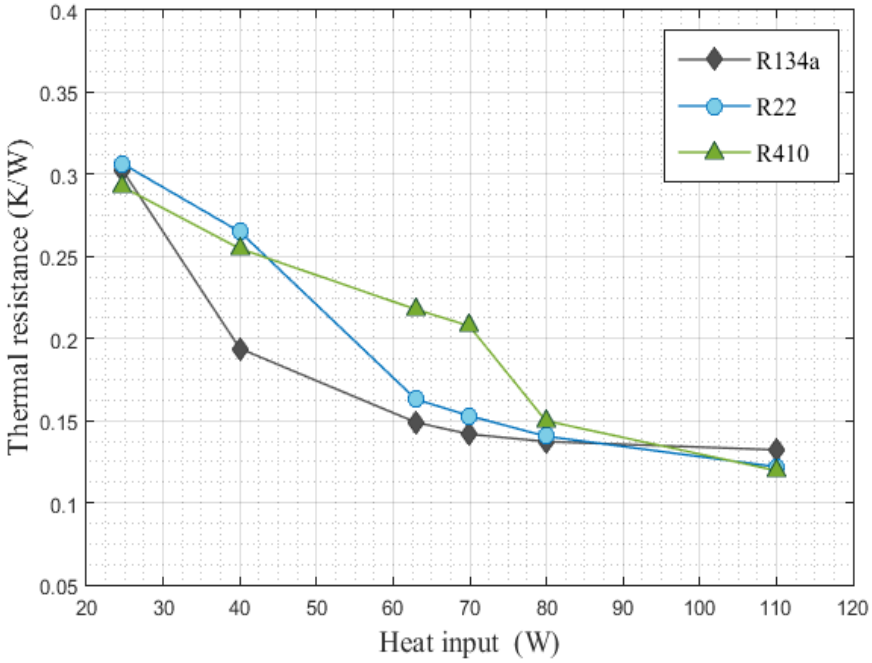

Figure 5-16: Effect of the type of refrigerants on the equivalent thermal resistance

As expected, the thermal resistance is reduced when increasing the heat input, for all working fluids, see Figure 5-16. By comparing the results obtained with three refrigerants in the same conditions, it is concluded that R134a has lowest thermal resistance and it is thus the best choice

in this study. It is observed that at medium heat input, the thermal resistance of R134a is 37% and 9% lower than R410 and R22, respectively.

5.8 Conclusion

The performance of a U-type horizontal smooth heat pipe has been studied both numerically and experimentally. The experimental tests were conducted on custom made setup built at the chemical engineering department of Université de Sherbrooke. Tests were conducted with refrigerant R134a at three powers 24, 60, 80 W and a filling ratio of 50%. Moreover, a new Euler-Euler model has been developed in OpenFOAM to analyze the heat transfer processes inside of this heat pipe, when evaporator and condenser were simultaneously working. The proposed model applies the ideas of the partitioned heat transfer mechanisms developed for boiling based on Kurul's study [60] s and extends it to cover pool condensation. A non-dimensional variable called condensation area fraction was introduced. It represents the fraction of the total wall area affected by the phase change mechanisms. By performing parametric analysis on experimental data, a new relation was proposed for condensation area fraction, which is only a function of subcooled temperature. Moreover, the experimental results such as temperature, pressure, heat flux and thermal resistance were used to validate the proposed numerical model. The numerical predictions show model's reliability and capability to simulate the key characteristics of pool boiling and condensation mechanisms when coupled in a closed system. Based on the parametric analysis performed on independent variables such as filling ratio, heat input, pipe diameter and type of refrigerant, it was found that:

- The optimum value for the filling ratio of a horizontal heat pipe is about 50%.
- The thermal resistance is decreased and heat performance of heat pipe is improved when power is increasing.
- The heat pipes have better efficiency at high power.
- The diameter had no considerable effect on the thermal resistance. It merely increases the surface area but scarcely affects the heat pipe performance.
- At medium power, the thermal resistance of R-134a was lower at 0.148 (K/W) when compared to 0.217 (K/W) for R410 and 0.163 (K/W) for R22.

6 CHAPTER SIX: Effect of groove on heat pipe performance

6.1 Abstract

As mentioned in the previous chapter, based on sensitivity analysis performed using the numerical model, it is found that merely increasing diameter or the surface area cannot affect the performance of this particular heat pipe. However, surface augmentation making use of grooves can have a positive effect on the phase change. By increasing the number of nucleation sites, pool boiling can be enhanced. On the other side, it is recommended to break and reduce the film condensation by using sharp edges on condensing surfaces for improving their performance [7], [39]. In this section, two different types of grooves were designed for the evaporator and some tests using the same conditions were conducted to seek any improvement in the heat pipe performance.

6.2 Literature review

Researchers suggested various groove geometries to improve the pool boiling heat transfer coefficient. There are some commercial enhanced tube available specially designed for nucleation boiling like Thermoexcel-E [81], Turbo-B [82], Gewa-T, B [83] and Everfin-Δ [84] (see Figure 6-1). It is found that having a reentrant cavity on phase change surface can considerably improve the heat transfer coefficient since nucleation sites may occur somewhere inside of cavities and activate bubble formation.

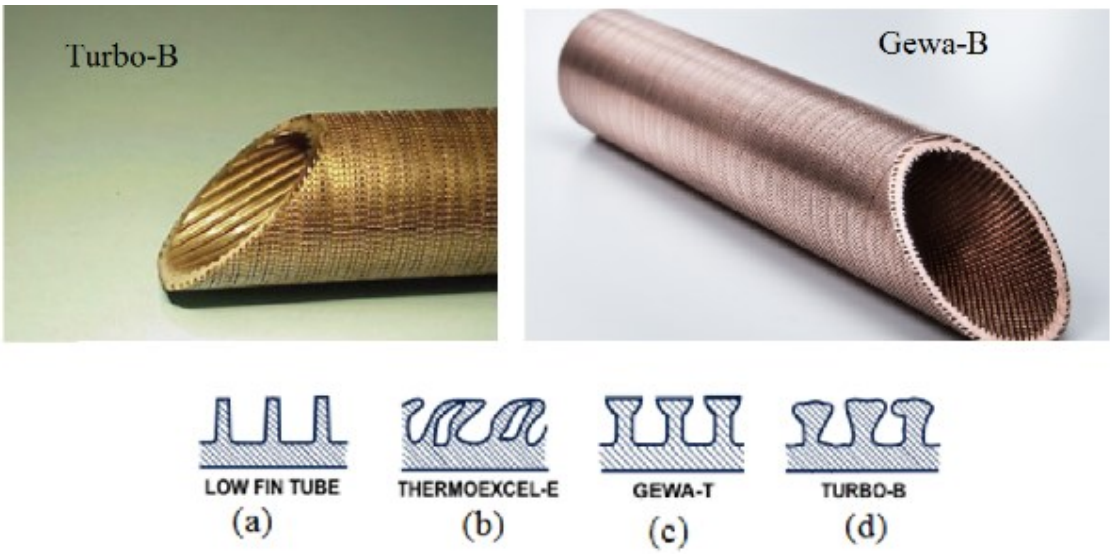

Figure 6-1: Different types of commercial enhanced tube for pool boiling- [85], [86]

Rooyen and Thome [43] used Wilson plot based on experimental data of refrigerant R134a and R236fa for two tubes Turbo-B and Gewa-T. Tests were performed for saturation temperature from 5 to 25 ^{o}C and heat flux between 15-70 kW/m^2. They show that for the same tube, the heat transfer coefficient of R236fa is lower than R134a. Also, Turbo-B tube has a better performance for higher heat flux (more than 40 kW/m^2) while Gewa-T type obtains a high heat transfer coefficient for lower heat flux. Webb and Pais [82] conducted pool boiling tests on five different horizontal tubes including commercial ones as Gewa-T and Turbo-B. They concluded that for R134a, Turbo-B design has a heat transfer coefficient of 2.9-4.7 times greater than a plain tube.

In addition, there are various experimental works for increasing the condensation heat transfer coefficient using enhanced surfaces. Some typical 3-dimensional tubes such as Thermoexcel-C [81], Turbo-C [87] and Gewa-C [88] were shown in Figure 6-2. These tubes usually have a sharp edge and their design is based on low-fin concept to increase the surface tension force and to break film condensation.

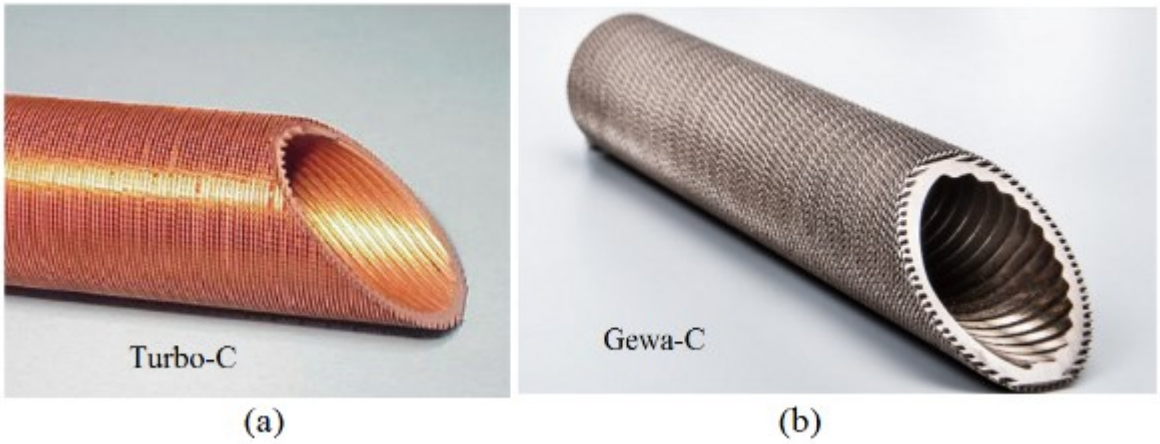

Figure 6-2: Different types of 3-dimensional tubes for condensation-[86]

Thome et al. [89] chose different types of tubes like Turbo-C, Gewa-C and low-fin to study the heat transfer coefficient of condensation for R134a. Their results demonstrated that 3-dimensional enhanced tubes have better performance when compared to low-fin tubes. In experimental work of Naresh et al. [7] the heat transfer performance of thermosyphon with internal finned condenser was investigated. They found that internally finned thermosyphon has superior performance than conventional one because it reinforces condensation and keeps

evaporator at safe temperature by postponing dry out condition. In addition, internal fins at condenser break the film condensation.

Recent studies reveals that the same enhanced profiles found be effective in evaporator were also suitable for condensation. Khalili [55] conducted tests on two partly sintered wick heat pipe with circumferential grooves and showed that using partly wick structure instead of complete one could improve heat transfer coefficient (boiling and condensation) since the liquid could directly contact groove surface. They concluded that a filling ratio of 20% is the optimum value for having the lowest thermal resistance and gravity has a negligible effect on horizontal wick heat pipe. Adding a coating to the surface by using an anodizing process or nanoparticles inside of working fluid has been done in experimental works of Solomon [79] and Liu [90]. They showed that the addition of nanoparticle or anodizing the surfaces creates thin porous coatings on the surface, which act as nucleation sites and enhance heat transfer by about 20% (Figure 6-3).

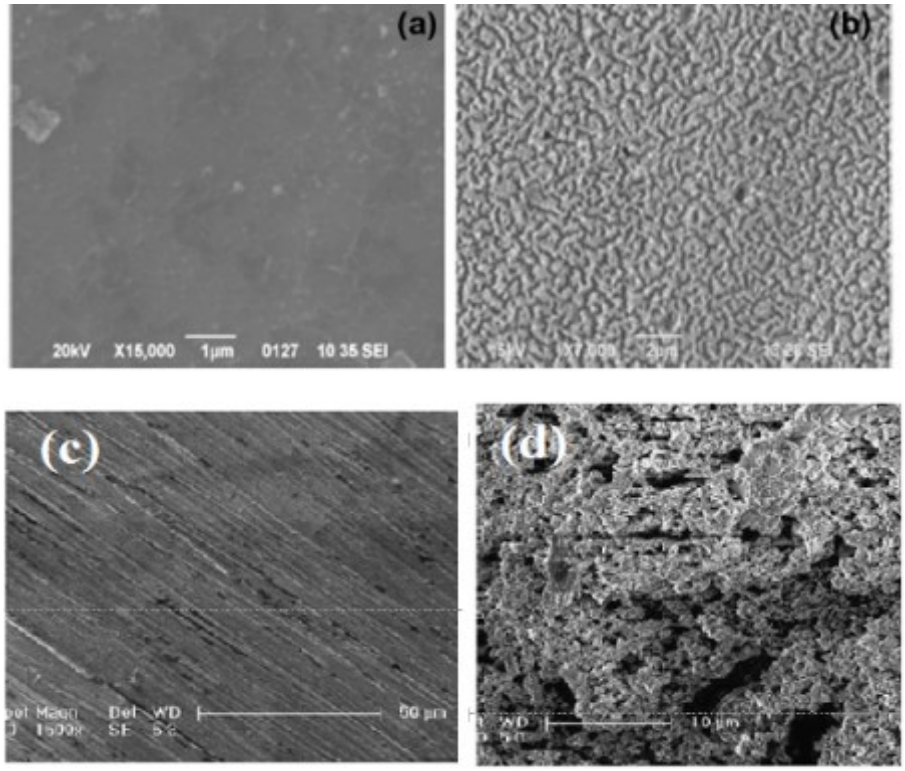

Figure 6-3: (a) Non-anodized surface, (b) anodized surface [79]-(c) surface with pure working fluid water (d) surface after adding nanoparticle to working fluid (40 nm Cu)- [90]

6.3 Experimental works

An analysis of grooved heat pipe performance is conducted on U-type horizontal tube consisting of a 180 mm long evaporator, a 180 mm condenser and a 280 mm adiabatic section. As mentioned before, the groove structure is implemented only for evaporator. The first design is a helicoidal groove with triangle shape while the second design is an axial groove with axial path in the shape of a half circle. The inner and external radius of the tube are 25.4 mm and 33.4 mm, respectively. The test facility as presented in Figure 5-1 consists of a heat pipe used as a test section, data acquisition system, computer, variable transformer as a power supply, water tank storage and flowmeter. The tests were conducted for four powers (24, 60, 80 and 110 W) with a filling ratio of 50%. For wickless heat pipes as the ones used here, the gravity force has a great effect on the circulation of the working fluid between the two sections. Thus, the liquid level must be uniform.

6.3.1 Position of thermistors and accuracy of measurement data

Ten calibrated thermistors are used in various positions for measuring the outside and inside temperatures of the heat pipe. Fours thermistors (TH1, TH2, TB1, TB2) are attached to the evaporator's wall and two thermal sensors (TH3, TB3) are installed on condenser's wall (see Figure 6-4). Four thermistors ($T_{top\text{-}evap}$, $T_{bottom\text{-}evap}$, $T_{top\text{-}cond}$, $T_{bottom\text{-}cond}$) are inserted inside the evaporator and condenser, far enough from the wall, to measure the temperature of the liquid and vapor, separately. Beside two pressure gauges connected to a high precision differential pressure transmitter were installed to measure pressure difference between two sections [91].

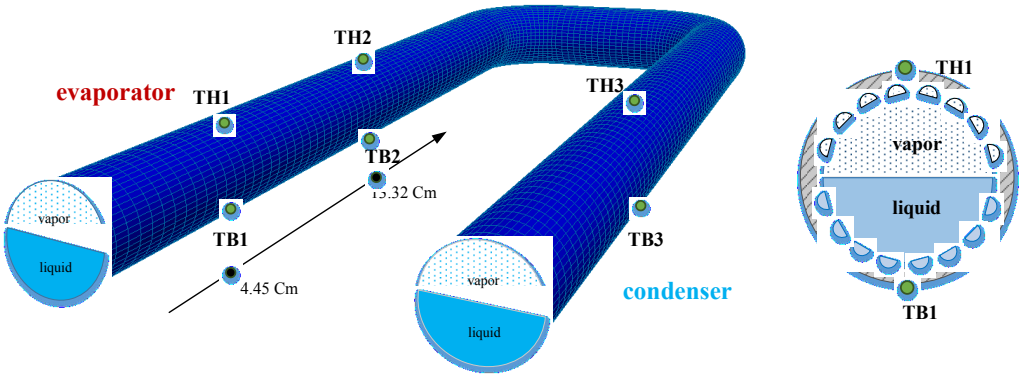

Figure 6-4: Position of thermistors on groove heat pipe

The shape, apex angle, width, height and space between grooves are all important parameters for the design of grooves. Some parameters such as shape and apex angle were fixed due to constraints in fabrication. Following plot was generated for identifying optimum values for the size of grooves, based on the analysis of available data in literature with the same refrigerant and same boiling regime. In Figure 6-5, the ratio parameter as width (W), space between grooves (W_t) and height (H) is presented in x-axis and y-axis, respectively. It seems that most researchers consider the same value for height and width of grooves within small gap between them.

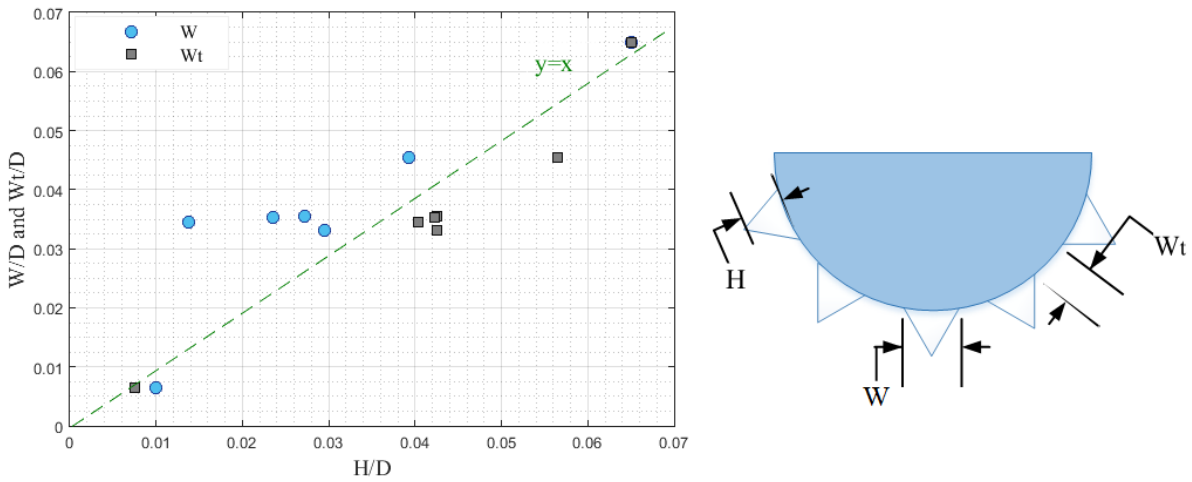

Figure 6-5:Non-dimensional width and space between groove vs height

The structure of final design and how groove increased surface area is presented in Figure 6-6 and TABLE 6-1.

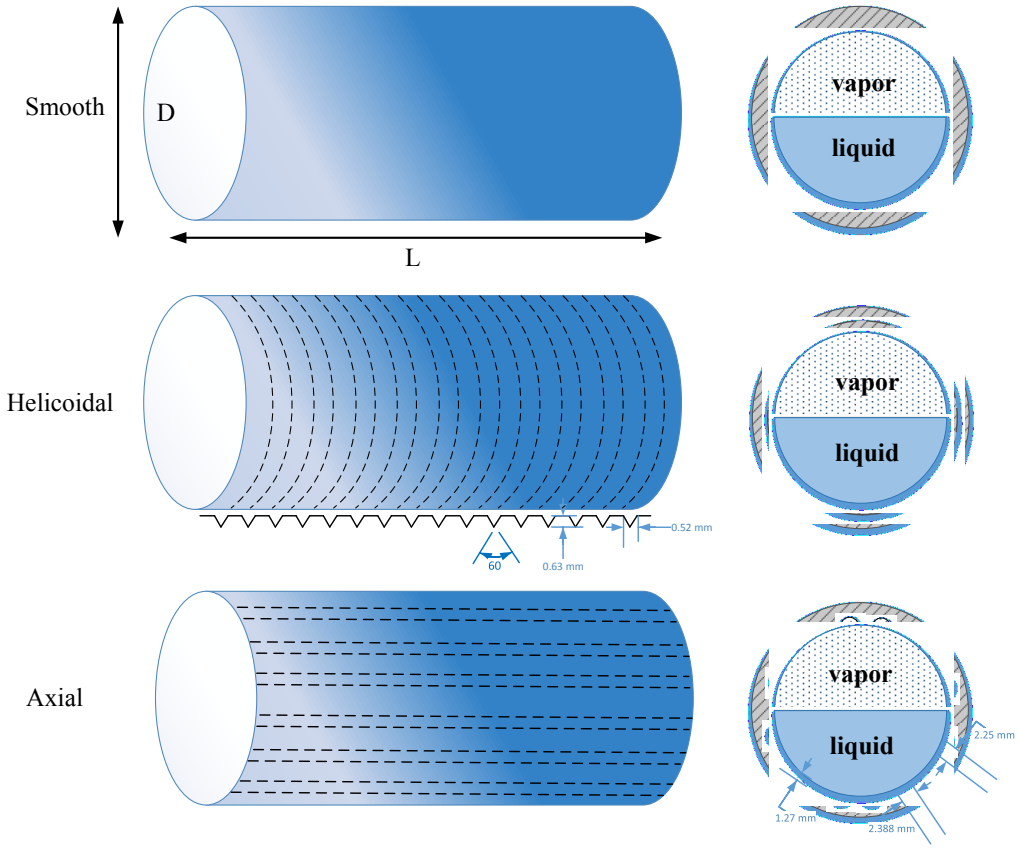

Figure 6-6: Schematic of smooth, helicoidal and axial grooved pipe

TABLE 6-1: Specification of tests tubes

Tube type	Outside diameter (mm)	Inside diameter (mm)	Apex angle	H (mm)	W (mm)	W_t (mm)	Number of grooves	Agroove/ Asmooth
Smooth	33.4	25.4	---	---	---	---	---	1
Helicoidal	33.4	25.4	60 °	0.65	0.52	0.52	40	2.007
Axial	33.4	25.4	---	3.27	2.388	2.25	18	1.272

6.3.2 Test procedure

The test is conducted for power inputs of 24, 60, 80 and 110 W. When a specific power is applied to the evaporator, the same energy is extracted in the condenser linked to a cooling system, a needed condition to obtain steady state where a balance of energy is satisfied in the whole system. Data acquisition system is connected to a computer to log and save the test data

including power input, temperature, pressure and water mass flow rate. All data is monitored and recorded in LabVIEW after reaching steady state conditions, which take about 2 hours. The steady state condition is considered when the temperature change in thermistors is less than ±1.0°C/hour.

6.3.3 Results of experimental works

The presented wall temperature for the evaporator and condenser is the average temperature recorded by the thermistors installed at the top and bottom of the wall.

$$T_{evap-wall} = \frac{T_{H1} + T_{H2} + T_{B1} + T_{B2}}{4}$$
$$T_{cond-wall} = \frac{T_{H3} + T_{B3}}{2} \qquad (6.1)$$

The power of the evaporator and condenser was estimated by Eq.(5.4). The temperature history of the helicoidal grooved pipe submitted to a power of 24 W is shown in Figure 6-7. As readers can see, the wall temperature is reaching to a steady state after 40 min. The vapor and liquid circulate continuously between evaporator and condenser due to the gravity force and pressure difference, which results in a merely constant filling ratio in the whole system.

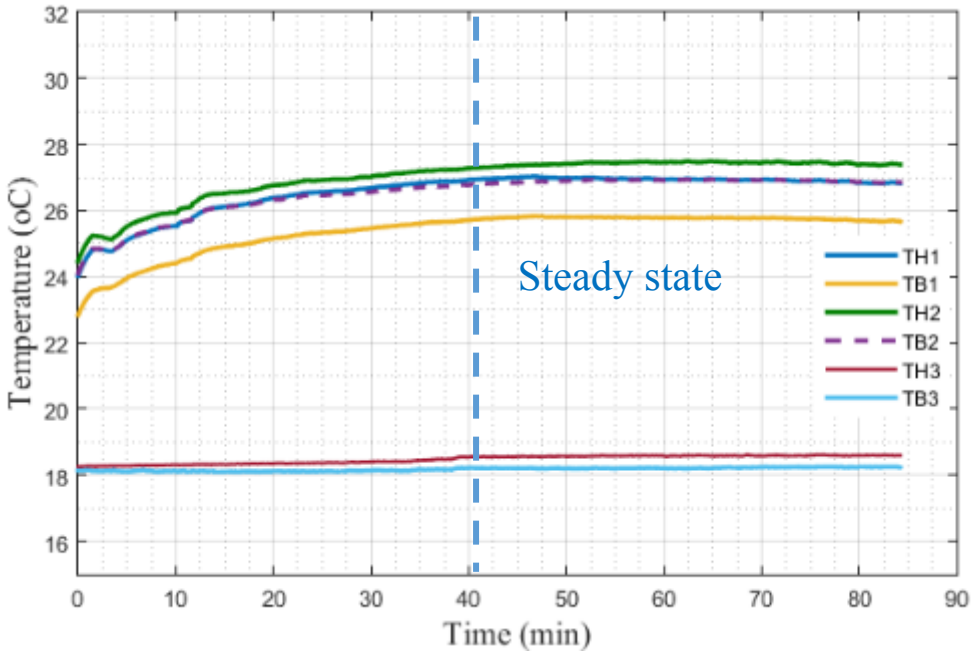

Figure 6-7: Wall temperature history of helicoidal grooved pipe at 24 W power

For axial grooved pipe at 24 W power, steady state condition is achieved after 70 minutes. Moreover, the liquid level is not considerably influenced by groove structure and merely constant at 50% (Figure 6-8).

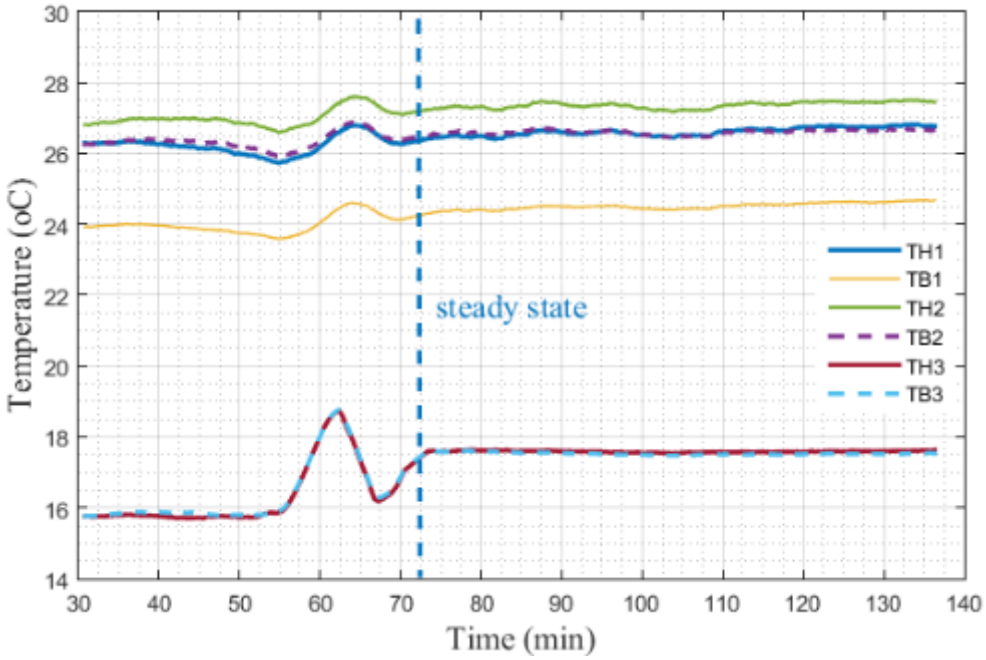

Figure 6-8: Wall temperature vs time for axial grooved pipe at 24W power

6.4 Comparing heat pipe performance

The performance of the heat pipes is typically estimated from the equivalent thermal resistance or from the estimated heat transfer coefficient. The equivalent thermal resistance is characterized by the temperature difference between evaporator and condenser divided by power of the evaporator or condenser (Eq.5.17). Beside the equivalent thermal resistance, one can define the thermal resistance of the evaporator and condenser, individually (Eq.5.18).

The result of equivalent thermal resistance for three heat pipes studied is depicted in Figure 6-9 in which shows that the thermal resistance has not been improved by the presence of grooves. Considering the ±15% error band (based on uncertainty analysis in TABLE 5-1) for the thermal resistance, it can be concluded that all three designs have the same performance. The tendency would even favor the smooth heat pipe since this design shows a consistent lower thermal resistance and better performance that the grooved designs.

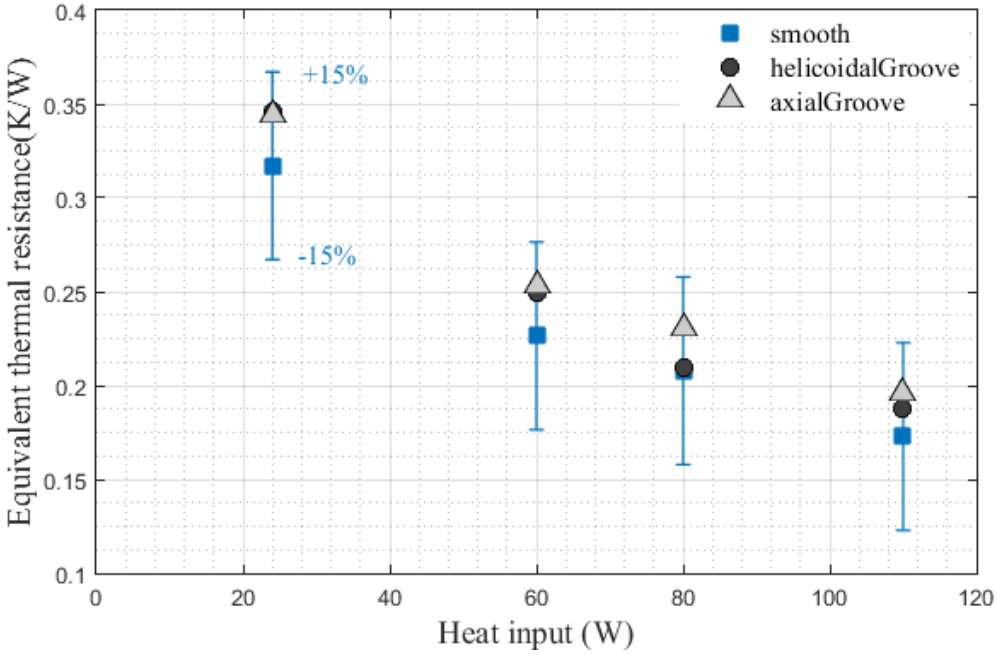

Figure 6-9: Equivalent thermal resistance for three different designs

Based on data presented in open literature, it was expected that making grooves would have positive effects on the heat pipe performance. The reason for the unexpected results are hidden on having this type of heat pipe, which has high portion of liquid without any wick structure. Moreover, no groove structure was added in the condenser section. Since evaporator and condenser are simultaneously working, they can strongly interact which affects the performance of the heat pipe. In condensation, gravity and surface tension play an important role. Cavities profiles on condenser surface not only enhance rate of condensing vapor but also increase surface tension in drawing back the liquid. Therefore, it is necessary to have the groove structure for both evaporator and condenser.

Since grooves were only added for the evaporator section, results of evaporator thermal resistance is presented in Figure 6-10. It is observed that the helicoidal groove shows a better performance since it has the lowest thermal resistance. Apparently, the helicoidal structure activates more nucleation sites for bubble generation and cannot block fluid motion. The reason of this unexpected behavior can be explained with minimum friction forces against fluid motion because of the high filling ratio. If a lower proportion of liquid was used, axial groove could

have better helped the circulation of fluid between evaporator and condenser in comparison to helicoidal groove and it might improve the heat pipe performance.

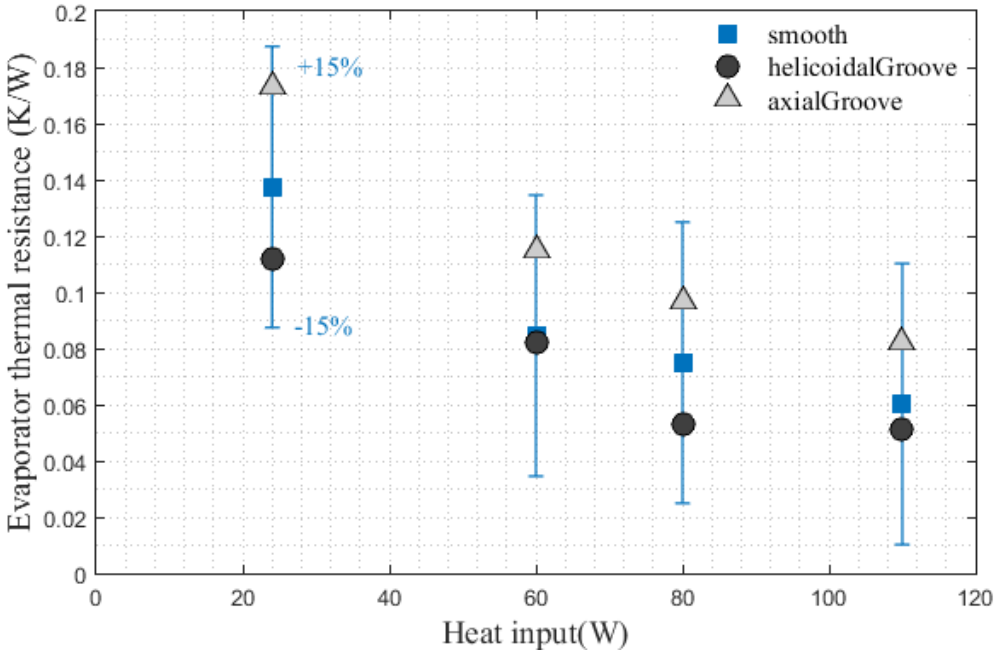

Figure 6-10: Evaporator thermal resistance for three different design

If one looks at boiling curve in Figure 2-1, nucleation boiling can be divided into two parts, subcooled region when the bulk of liquid has a lower temperature than saturation. In this region, bubbles mostly collapse and disappear after leaving the wall. When the bulk liquid is reaching to saturation, saturated boiling is starting with higher heat transfer coefficient and bubbles can grow and reach to upper surface.

As presented in Figure 6-11, the temperature of the bulk liquid in helicoidal grooved design is reaching to the saturation temperature and consequently it is entering saturated boiling region where bubbles were observed to reach the liquid-gas interface (they have small size and very high detachment frequency). However, for axial grooved design presented in Figure 6-12, bubbles have been scarcely seen in the bulk liquid since most of them collapsed and transfer their heat to the surrounding liquid, before reaching the liquid-gas interface. Therefore, helicoidal grooved pipe has a higher heat transfer coefficient and lower thermal resistance when compared to the axial grooved design.

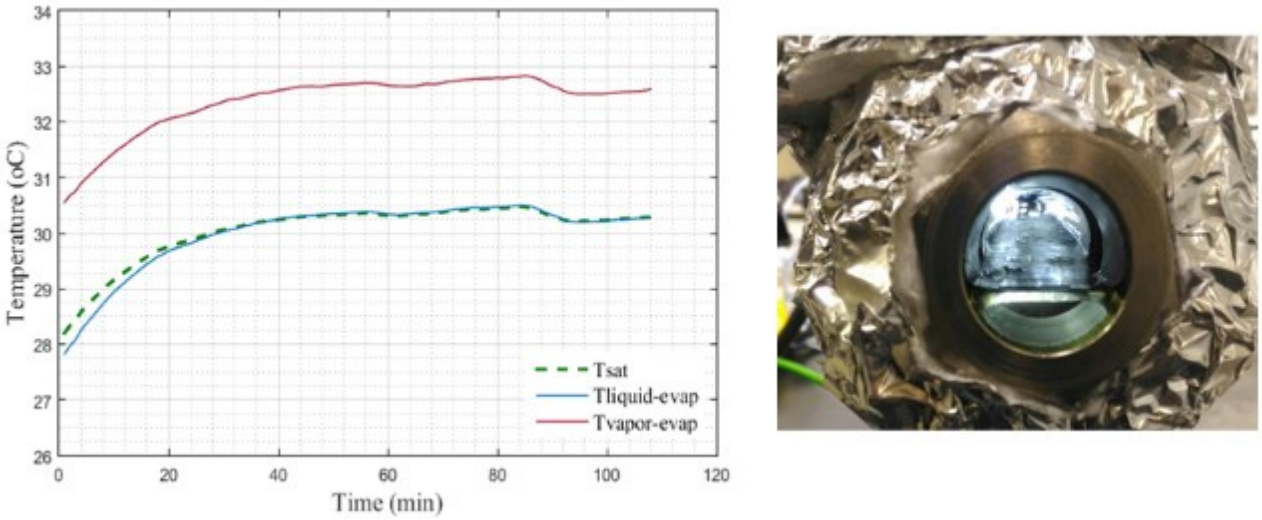

Figure 6-11: Helicoidal grooved pipe in saturated boiling region at power 110 W

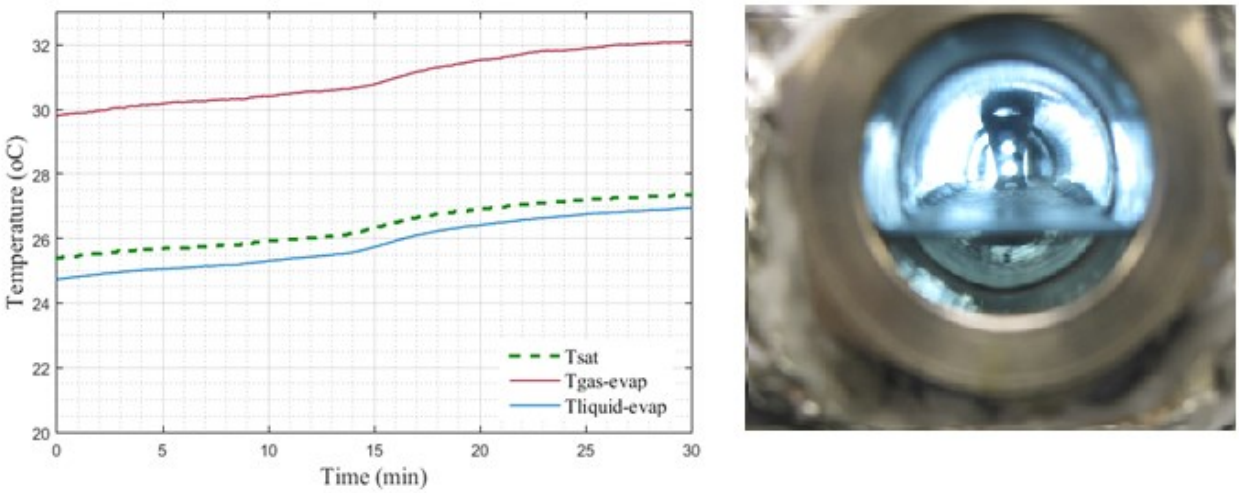

Figure 6-12: Axial grooved pipe in subcooled boiling region at power 110 W

6.5 Conclusion

Two types of groove structures were designed and analyzed their effects on thermal resistance to seeking improvement in heat pipe performance. It is observed that the helicoidal groove can improve evaporator thermal resistance of about 20%. However, the axial groove reduces thermal resistance between 7-10 %. Moreover, no improvements have been seen in equivalent thermal resistance. Having high filling ratio and neglecting condenser section can be two reasons that lead not to benefits from groove structure advantages.

7 CHAPTER SEVEN: Conclusion and futures works

Combining boiling, condensation and the mutual effect of evaporator and condenser on each other are crucial for a rigorous analysis of the heat transfer inside a heat pipe. In boiling or condensation, a large amount of heat transfer rate is obtained when compared to single-phase convection. Therefore, precise modeling of the phase change is considered as an essential step towards developing an accurate numerical model for the simulation of heat transfer inside a heat pipe

The purpose of this PhD project was to develop a new solver in OpenFOAM to simulate the phase changes occurring inside a heat pipe and to evaluate its performance. The bubble formation in early stages of evaporation affects the heat transfer coefficient. Moreover, the condenser interacts with the evaporator and eventually affect the global performance of the heat pipe. Therefore, critical items for the evaluation of the heat pipe performance were the separate comprehension of the boiling and of the condensation models, and the combination of both models to represent the behaviour of a closed system. In addition, the estimation of two-phase parameters such as phase fraction, dispersed phase size, velocity, temperature and pressure is also important for the implementation of the two-phase model.

The numerical model has been developed inside an open source code using OpenFOAM as the main framework. This program gives to the user the opportunity to modify any existing solver and create a new one. The nearest solver to this work is called "*reactingTwophaseEulerFoam"*. It has been selected since it is based on the Euler-Eulerian method and is suitable for modeling phase change. Since the phase change contributes to non-uniform fluid properties, the solver is extended to turbulent regime and additional source terms were added to the basic solver. Because the boiling model already existed in this solver, our work started with implantation of the energy and mass transfer terms for modeling condensation. Among interfacial forces, drag and virtual mass forces were only added since other forces did not have any significant effects on the presented results. For wall heat flux in condensation, two terms called condensation heat flux and single-phase convection heat flux were introduced, which depends on a new term: the condensation area fraction. Published experimental data found in open sources were used to prove the capability and versatility of the implemented model. Also, a new relation for the calculation of the heat transfer coefficient in flow condensation regime was proposed.

In order to complete the proposed modeling, in next step, both boiling and condensation models were coupled together. In a closed system, the drastic variation of variables like fluid properties or pressure severely affected the numerical solution. In order to reduce pressure instability, a high precision relation for coupling the saturation pressure and temperature was used. The numerical model performance was tested and validated using a scaled down experimental heat pipe built at Université de Sherbrooke. Satisfactory results were produced as shown by a comparison between the numerical predictions and the experimental data.

The special characteristics of this study has been briefly presented:

- The performance of a horizontal smooth heat pipe has been studied both numerically and experimentally.
- A new Euler-Euler model has been developed in OpenFOAM to analyze the heat transfer processes inside of a horizontal smooth heat pipe, when evaporator and condenser were simultaneously working.
- The proposed model applies the ideas of the partitioned heat transfer mechanisms developed for boiling and condensation based on Kurul model [60]. Two non-dimensional variables called boiling and condensation area fraction were introduced. They both represent the fraction of the total wall area affected by the phase change mechanisms.
- The interfacial momentum and energy transfer were applied to have a precise model of momentum and energy transferring between both phases.
- The experimental tests were conducted on a custom made experimental setup built at the chemical engineering department of Université de Sherbrooke.
- The experimental results such as temperature, pressure, heat flux and thermal resistance were used to validate the proposed numerical model.
- The numerical predictions show model's reliability and capability to simulate the key characteristics of boiling and condensation mechanisms when coupled in a closed system.
- Two models of groove design were tested to analyze improvement in heat pipe performance.
- The helicoidal groove showed lower evaporator thermal resistance than the axial groove since it provided more surface for heat transfer and more nucleation site for bubble generation.

Conclusion

The model can be improved through implementing the following suggestions:

- Having groove profile for condenser and evaporator. Adding a groove structure at the evaporator did not affect the thermal resistance of this particular model of heat pipe. Therefore, considering same profile can be a solution of improving heat pipe performance.
- Using a straight tube instead of U-type tube, since U-shape path can affect stability of fluid circulation between evaporator and condenser.
- Adding wick structure on the wall and decrease the filling ratio.
- Adding a coating to the surface by anodizing process or adding nanoparticles.
- Increasing accuracy of numerical model by improving the suggested equation for condensation area fraction
- Performing sensitivity analysis on wide range of parameters and having more experimental data

CHAPITER SEPT: Conclusion et Travaux Futurs

La combinaison de l'ébullition, de la condensation et de l'effet mutuel de l'évaporateur et du condenseur est cruciale pour une analyse rigoureuse du transfert de chaleur à l'intérieur d'un caloduc. En ébullition ou condensation, on obtient une large quantité de chaleur par comparaison à la convection monophasée. Par conséquent, la modélisation précise du changement de phase est considérée une étape essentielle dans le développement d'un modèle numérique précis pour la simulation du transfert de chaleur à l'intérieur d'un caloduc.

L'objectif de ce projet de thèse était de développer un nouveau solveur dans OpenFOAM pour simuler les changements de phase à l'intérieur d'un caloduc et évaluer ses performances. La formation de bulles dans les premiers stades de l'évaporation affecte le coefficient de transfert de chaleur. De plus, le condenseur interagit avec l'évaporateur et finit par affecter les performances globales du caloduc. Par conséquent, les éléments critiques pour l'évaluation de la performance du caloduc étaient la compréhension séparée des modèles d'ébullition et condensation, et la combinaison des deux modèles pour représenter le comportement d'un système fermé. En outre, l'estimation des paramètres à deux phases, tels que la fraction de phase, la taille de la phase dispersée, la vitesse, la température et la pression, est également importante pour la modèle à deux phases.

Le modèle numérique a été développé dans un code source en utilisant OpenFOAM. Ce programme donne à l'utilisateur la possibilité de modifier tout solveur existant et de créer un nouveau. Le solveur s'appelle «*reactingTwophaseEulerFoam*». Il a été sélectionné car il est basé sur la méthode Euler-Eulerian et convient à la modélisation du changement de phase. Le changement de phase contribue aux propriétés non-uniformes du fluide, le solveur est étendu au régime turbulent et des termes sources supplémentaires ont été ajoutés au solveur de base. Le modèle d'ébullition existait déjà dans ce solveur, notre travail a débuté par l'implantation des termes de transfert d'énergie et de masse pour la modélisation de la condensation. Pour les forces interfaciales, la drague et les forces de masse virtuelles ont été ajoutées parce que d'autres forces n'ont pas eu effet significatif sur les résultats présentés. Pour le flux thermique aux murs en condensation, deux termes appelés flux thermique de condensation et flux thermique de convection monophasé ont été introduits, ce qui dépend d'un nouveau terme : la fraction de surface de condensation. Les expérimentales publiées trouvées dans des sources ont été utilisées

pour prouver la capacité du modèle. En outre, une nouvelle relation pour le calcul du coefficient de transfert de chaleur en régime de condensation a été proposée.

Afin de compléter la modélisation, à l'étape suivante, les modèles d'ébullition et de condensation ont été couplés. Dans un système fermé, la variation radicale de variables telles que les propriétés des fluides comme la pression affectait gravement la solution numérique. Afin de réduire l'instabilité, une relation de haute précision pour coupler la pression de saturation et la température a été utilisée. Les performances du modèle numérique ont été validées à l'aide d'un caloduc à l'Université de Sherbrooke. Des résultats satisfaisants ont été produits, comme le montre une comparaison entre les prédictions numériques et les expérimentales.

Les caractéristiques spéciales de cette étude ont été brièvement présentées :

• Les performances d'un caloduc horizontal ont été étudiées numériquement et expérimentalement.

• Un nouveau modèle Euler-Euler a été développé dans OpenFOAM pour analyser les processus de transfert de chaleur à l'intérieur d'un caloduc horizontal, lorsque l'évaporateur et le condenseur ont simulé.

• Le modèle proposé applique les idées des mécanismes de transfert de chaleur partitionnés développés pour l'ébullition et la condensation sur la base du modèle de Kurul [56]. Deux variables non dimensionnelles appelées fraction d'aire d'ébullition et condensation ont été introduites. Ils représentent tous les deux la fraction de la surface totale de la paroi affectée par les mécanismes de changement de phase.

• Le moment interfacial et le transfert d'énergie ont été appliqués pour obtenir un modèle précis du transfert de mouvement et d'énergie entre les deux phases.

• Les tests expérimentaux ont été effectués sur un modèle construit au département de génie chimique de l'Université de Sherbrooke.

• Les résultats expérimentaux comme la température, la pression, le flux thermique et la résistance thermique ont été utilisés pour valider le modèle numérique proposé.

• Les prévisions numériques montrent la fiabilité du modèle et sa capacité à simuler les principales caractéristiques des mécanismes d'ébullition et de condensation lorsqu'elles sont couplées dans un système fermé.

• Deux modèles de conception de rainures ont été testés pour analyser l'amélioration des performances du caloduc.

• Le caloduc hélicoïdal présentait une résistance thermique de l'évaporateur inférieure à celle de la gorge axiale, car elle offrait plus de surface pour le transfert de chaleur et plus de site de nucléation pour la génération de bulles.

Le modèle peut être amélioré en appliquant les suggestions suivantes:

• Avoir un profil de gorge pour le condenseur et l'évaporateur. L'ajout d'une structure de gorge à l'évaporateur n'a pas affecté la résistance thermique de ce modèle particulier de caloduc. Par conséquent, considérer le même profil peut être une solution pour améliorer les performances du caloduc.

• Utiliser un tube droit au lieu d'un tube de type U, car le trajet en U peut affecter la stabilité de la circulation du fluide entre l'évaporateur et le condenseur.

• Ajouter une structure de mèche sur le mur et diminuer le taux de remplissage.

• Ajouter un revêtement à la surface par anodisation ou ajouter des nanoparticules.

• Augmenter la précision du modèle numérique en améliorant l'équation suggérée pour la fraction de surface de condensation

• Effectuer une analyse de sensibilité sur une large gamme de paramètres et disposer de davantage de données expérimentales

8 References

[1] A. Faghri, “Heat pipes: review, opportunities and challenges,” *Front. Heat Pipes FHP*, vol. 5, no. 1, 2014.

[2] “http://www.engineeredair.com/index.php/our_products/category/energy-recovery-and-iaq-products.”

[3] A. Faghri, “Review and advances in heat pipe science and technology,” *J. Heat Transf.*, vol. 134, no. 12, p. 123001, 2012.

[4] S. Launay, V. Sartre, and J. Bonjour, “Parametric analysis of loop heat pipe operation: a literature review,” *Int. J. Therm. Sci.*, vol. 46, no. 7, pp. 621–636, 2007.

[5] S. G. Kandlikar, *Handbook of phase change: boiling and condensation*. CRC Press, 1999.

[6] E. U. Schlunder, *Heat Transfer Atlas: Calculation of Heat Transfer*. Germany: VDI Verlag, Woodhead Publishing, 1990.

[7] Y. Naresh and C. Balaji, “Thermal performance of an internally finned two phase closed thermosyphon with refrigerant R134a: A combined experimental and numerical study,” *Int. J. Therm. Sci.*, vol. 126, pp. 281–293, 2018.

[8] M. Mahdavi, S. Tiari, S. De Schampheleire, and S. Qiu, “Experimental study of the thermal characteristics of a heat pipe,” *Exp. Therm. Fluid Sci.*, vol. 93, pp. 292–304, 2018.

[9] E. Michta, “Modeling of subcooled nucleate boiling with OpenFOAM,” KTH- Royal Institute of Technology Stockholm, Sweden, February 2011.

[10] A. Ghione, “Development and validation of a two-phase CFD model using OpenFOAM,” KTH-Royal Institute of Technology Stockholm, Sweden, 2012.

[11] R. Rabiee, M. Désilets, P. Proulx, M. Ariana, and M. Julien, “Determination of condensation heat transfer inside a horizontal smooth tube,” *Int. J. Heat Mass Transf.*, vol. 124, pp. 816–828, 2018.

[12] R. Rabiee, B. Rajabloo, M. Désilets, and P. Proulx, “Heat transfer analysis of boiling and condensation inside a horizontal heat pipe,” *Int. J. Heat Mass Transf.*, vol. 139, pp. 526–536, 2019.

[13] “OpenCFD Limited. OpenFOAM User Guide. http://www.openfoam.com/docs/user/, 2011.”

[14] A. C. Yunus, “Heat transfer: a practical approach,” *MacGraw Hill N. Y.*, 2003.

[15] Y. A. Cengel, S. Klein, and W. Beckman, *Heat transfer: a practical approach*, vol. 141. McGraw-Hill New York, 1998.

[16] M. G. Cooper, “Heat flow rates in saturated nucleate pool boiling-a wide-ranging examination using reduced properties,” in *Advances in heat transfer*, vol. 16, Elsevier, 1984, pp. 157–239.

[17] G. Ribatski and J. M. S. Jabardo, “Experimental study of nucleate boiling of halocarbon refrigerants on cylindrical surfaces,” *Int. J. Heat Mass Transf.*, vol. 46, no. 23, pp. 4439–4451, 2003.

[18] D. Jung, Y. Kim, Y. Ko, and K. Song, “Nucleate boiling heat transfer coefficients of pure halogenated refrigerants,” *Int. J. Refrig.*, vol. 26, no. 2, pp. 240–248, 2003.

[19] K. Stephan and M. Abdelsalam, “Heat-transfer correlations for natural convection boiling,” *Int. J. Heat Mass Transf.*, vol. 23, no. 1, pp. 73–87, 1980.

[20] J. Buongiorno, “Boiling heat transfer and phase changes, basic terms.” a review report for course in MIT university, 2010.

[21] M. MOHAMMED SHAH, “Generalized prediction of heat transfer during subcooled boiling in annuli,” *Heat Transf. Eng.*, vol. 4, no. 1, pp. 24–31, 1983.

[22] L. Wojtan, R. Revellin, and J. R. Thome, “Investigation of critical heat flux in single, uniformly heated microchannels,” in *ECI International Conference on Heat Transfer and Fluid Flow in Microscale*, 2005.

[23] W. Zhang, T. Hibiki, K. Mishima, and Y. Mi, “Correlation of critical heat flux for flow boiling of water in mini-channels,” *Int. J. Heat Mass Transf.*, vol. 49, no. 5–6, pp. 1058–1072, 2006.

[24] X. Fang, "A new correlation of flow boiling heat transfer coefficients based on R134a data," *Int. J. Heat Mass Transf.*, vol. 66, pp. 279–283, 2013.
[25] J. C. Chen, "Correlation for boiling heat transfer to saturated fluids in convective flow," *Ind. Eng. Chem. Process Des. Dev.*, vol. 5, no. 3, pp. 322–329, 1966.
[26] K. F. Gungor, "Simplified General Correlation for Saturrated Flow Boiling and Comparison of Correlation with Data," *Chem Eng Res Dev*, vol. 65, p. 148, 1987.
[27] L. Sun and K. Mishima, "An evaluation of prediction methods for saturated flow boiling heat transfer in mini-channels," *Int. J. Heat Mass Transf.*, vol. 52, no. 23–24, pp. 5323–5329, 2009.
[28] S. G. Kandlikar, "A general correlation for saturated two-phase flow boiling heat transfer inside horizontal and vertical tubes," *J. Heat Transf.*, vol. 112, no. 1, pp. 219–228, 1990.
[29] W. M. Rohsenow, J. P. Hartnett, and Y. I. Cho, *Handbook of heat transfer*, vol. 3. McGraw-Hill New York, 1998.
[30] J. C. Chato, "Laminar condensation inside horizontal and inclined tubes," Massachusetts Institute of Technology, 1960.
[31] A. Umur and P. Griffith, "Mechanism of dropwise condensation," *J. Heat Transf.*, vol. 87, no. 2, pp. 275–282, 1965.
[32] J. R. Thome, J. El Hajal, and A. Cavallini, "Condensation in horizontal tubes, part 2: new heat transfer model based on flow regimes," *Int. J. Heat Mass Transf.*, vol. 46, no. 18, pp. 3365–3387, 2003.
[33] M. M. Shah, "A general correlation for heat transfer during film condensation inside pipes," *Int. J. Heat Mass Transf.*, vol. 22, no. 4, pp. 547–556, 1979.
[34] W. W. Akers, "Condensation inside horizontal tubes," in *Chem. Engg. Prog. Symp. Ser.*, 1960, vol. 56, p. 145.
[35] M. K. Dobson and J. C. Chato, "Condensation in smooth horizontal tubes," *J. Heat Transf.*, vol. 120, no. 1, pp. 193–213, 1998.
[36] A. Cavallini and R. Zecchin, "A dimensionless correlation for heat transfer in forced convection condensation." 6th International Heat Transfer Congress, 1974.
[37] D. P. Traviss, W. M. Rohsenow, and A. B. Baron, "Forced-convection condensation inside tubes: a heat transfer equation for condenser design," *ASHRAE Trans*, vol. 79, no. 1, pp. 157–165, 1973.
[38] S. G. Kandlikar, "A model for correlating flow boiling heat transfer in augmented tubes and compact evaporators," *J. Heat Transf.*, vol. 113, no. 4, pp. 966–972, 1991.
[39] W.-T. Ji, M. Numata, Y.-L. He, and W.-Q. Tao, "Nucleate pool boiling and filmwise condensation heat transfer of R134a on the same horizontal tubes," *Int. J. Heat Mass Transf.*, vol. 86, pp. 744–754, 2015.
[40] R. G. Tripathi and V. V. Buwa, "Numerical Simulations of Gas-Liquid Boiling Flows Using OpenFOAM," *Procedia IUTAM*, vol. 15, pp. 178–185, 2015.
[41] M. Shademan, R. Balachandar, and R. Barron, "Cfd Simulation of Boiling Heat Transfer Using Openfoam," in *Proceedings of the ASME 2014 International Mechanical Engineering Congress and Exposition, Montreal*, 2014.
[42] S. P. Rocha, O. Kannengieser, E. M. Cardoso, and J. C. Passos, "Nucleate pool boiling of R-134a on plain and micro-finned tubes," *Int. J. Refrig.*, vol. 36, no. 2, pp. 456–464, 2013.
[43] E. Van Rooyen and J. R. Thome, "Pool boiling data and prediction method for enhanced boiling tubes with R-134a, R-236fa and R-1234ze (E)," *Int. J. Refrig.*, vol. 36, no. 2, pp. 447–455, 2013.
[44] C.-P. Yin, Y.-Y. Yan, T.-F. Lin, and B.-C. Yang, "Subcooled flow boiling heat transfer of R-134a and bubble characteristics in a horizontal annular duct," *Int. J. Heat Mass Transf.*, vol. 43, no. 11, pp. 1885–1896, 2000.
[45] A. Cavallini, G. Censi, D. Del Col, L. Doretti, G. A. Longo, and L. Rossetto, "Experimental investigation on condensation heat transfer and pressure drop of new HFC refrigerants (R134a, R125, R32, R410A, R236ea) in a horizontal smooth tube," *Int. J. Refrig.*, vol. 24, no. 1, pp. 73–87, 2001.

[46] R. Suliman, L. Liebenberg, and J. P. Meyer, "Improved flow pattern map for accurate prediction of the heat transfer coefficients during condensation of R-134a in smooth horizontal tubes and within the low-mass flux range," *Int. J. Heat Mass Transf.*, vol. 52, no. 25, pp. 5701–5711, 2009.
[47] M. A. Hossain, Y. Onaka, and A. Miyara, "Experimental study on condensation heat transfer and pressure drop in horizontal smooth tube for R1234ze (E), R32 and R410A," *Int. J. Refrig.*, vol. 35, no. 4, pp. 927–938, 2012.
[48] B. Panitapu, "Determination of Condensation Heat Transfer Coefficient inside a Horizontal Pipe at High Pressure using Experimental Analysis."
[49] R. Bassi and P. K. Bansal, "In-tube condensation of mixture of R134a and ester oil: empirical correlations," *Int. J. Refrig.*, vol. 26, no. 4, pp. 402–409, 2003.
[50] T. Brahim and A. Jemni, "Effect of the Heat Pipe Adiabatic Region," *J. Heat Transf.*, vol. 136, no. 4, p. 042901, 2014.
[51] B. Fadhl, L. C. Wrobel, and H. Jouhara, "Numerical modelling of the temperature distribution in a two-phase closed thermosyphon," *Appl. Therm. Eng.*, vol. 60, no. 1–2, pp. 122–131, 2013.
[52] Y. Naresh, K. S. Vignesh, and C. Balaji, "Experimental investigations of the thermal performance of self-rewetting fluids in internally finned wickless heat pipes," *Exp. Therm. Fluid Sci.*, vol. 92, pp. 436–446, 2018.
[53] S. N. R. Abadi and J. P. Meyer, "Numerical investigation into the inclination effect on conjugate pool boiling and the condensation of steam in a passive heat removal system," *Int. J. Heat Mass Transf.*, vol. 122, pp. 1366–1382, 2018.
[54] J.-C. Wang, "U-and L-shaped heat pipes heat sinks for cooling electronic components employed a least square smoothing method," *Microelectron. Reliab.*, vol. 54, no. 6–7, pp. 1344–1354, 2014.
[55] M. Khalili and M. B. Shafii, "Experimental and numerical investigation of the thermal performance of a novel sintered-wick heat pipe," *Appl. Therm. Eng.*, vol. 94, pp. 59–75, 2016.
[56] J. Corberán and M. G. Melon, "Modelling of plate finned tube evaporators and condensers working with R134a," *Int. J. Refrig.*, vol. 21, no. 4, pp. 273–284, 1998.
[57] M. MARENGO, S. ZINNA, and C. FUSTINONI, "Integration of a lumped parameters code with a finite volume code: numerical analysis of a heat pipe," in *UIT National Heat Transfer Conference*, 2009.
[58] H. Rusche, "Computational fluid dynamics of dispersed two-phase flows at high phase fractions," Imperial College London (University of London), 2003.
[59] F. Durst, D. Miloievic, and B. Schönung, "Eulerian and Lagrangian predictions of particulate two-phase flows: a numerical study," *Appl. Math. Model.*, vol. 8, no. 2, pp. 101–115, 1984.
[60] N. Kurul and M. Z. Podowski, "On the modeling of multidimensional effects in boiling channels," in *ANS Proceeding of the 27th National Heat Transfer Conference*, 1991.
[61] W. M. Rohsenow, "A new correlation of pool-boiling data including the effect of heating surface characteristics," *Stainl. STEEL*, vol. 1, no. 111, p. 1, 1968.
[62] V. I. Tolubinsky and D. M. Kostanchuk, "Vapour bubbles growth rate and heat transfer intensity at subcooled water boiling," in *International Heat Transfer Conference 4*, 1970, vol. 23.
[63] M. Lemmert and J. M. Chawla, "Influence of flow velocity on surface boiling heat transfer coefficient," *Heat Transf. Boil.*, vol. 237, p. 247, 1977.
[64] R. Cole, "A photographic study of pool boiling in the region of the critical heat flux," *AIChE J.*, vol. 6, no. 4, pp. 533–538, 1960.
[65] Y. Egorov and F. Menter, "Experimental implementation of the RPI wall boiling model in CFX-5.6," *Staudenfeldweg*, vol. 12, p. 83624, 2004.
[66] J. W. Palen and J. Taborek, "Prediction of horizontal tubeside condensation of pure components using flow regime criteria," *J. Heat Transf.*, vol. 102, p. 471, 1980.
[67] A. Cavallini, G. Censi, D. Del Col, L. Doretti, G. A. Longo, and L. Rossetto, "Condensation of halogenated refrigerants inside smooth tubes," *HVACR Res.*, vol. 8, no. 4, pp. 429–451, 2002.
[68] S. M. Zivi, "Estimation of steady-state steam void-fraction by means of the principle of minimum entropy production," *J. Heat Transf.*, vol. 86, no. 2, pp. 247–251, 1964.

[69] A. Cavallini *et al.*, "Condensation in horizontal smooth tubes: a new heat transfer model for heat exchanger design," *Heat Transf. Eng.*, vol. 27, no. 8, pp. 31–38, 2006.
[70] A. Cavallini *et al.*, "Condensation inside and outside smooth and enhanced tubes—a review of recent research," *Int. J. Refrig.*, vol. 26, no. 4, pp. 373–392, 2003.
[71] J. P. Holman, "Heat transfer, 1986," *Mc Gran–Hill Book Co. Soythern Methodist Univ.*, 1986.
[72] "https://en.wikipedia.org/wiki/Heat_pipe."
[73] T. Bouhal, Y. Agrouaz, T. Kousksou, T. El Rhafiki, and Y. Zeraouli, "Performance optimization of a two-phase closed thermosyphon through cfd numerical simulations," *Appl. Therm. Eng.*, vol. 128, pp. 551–563, 2018.
[74] H. Kavusi and D. Toghraie, "A comprehensive study of the performance of a heat pipe by using of various nanofluids," *Adv. Powder Technol.*, vol. 28, no. 11, pp. 3074–3084, 2017.
[75] "https://www.rogerscorp.com/ems/arlon/producttype/11/Secure-Silicone-Thermal-Transfer-Adhesives.aspx." .
[76] "http://www.stacoenergy.com/images/staco/literature_finder/english/variable-transformers-and-test-sets/stacovt/brochure/VT_ProdGuide_bro-042514.pdf." .
[77] "https://uk.rs-online.com/web/p/thermal-grease/0554311/." .
[78] "Cole-Parmer Valved Acrylic Flowmeter, 50 mm Scale for Air, 0.1-1 LPM from Cole-Parmer Canada." [Online]. Available: https://www.coleparmer.ca/i/cole-parmer-valved-acrylic-flowmeter-50-mm-scale-for-air-0-1-1-lpm/3246042. [Accessed: 23-Aug-2018].
[79] A. B. Solomon, R. Roshan, W. Vincent, V. K. Karthikeyan, and L. G. Asirvatham, "Heat transfer performance of an anodized two-phase closed thermosyphon with refrigerant as working fluid," *Int. J. Heat Mass Transf.*, vol. 82, pp. 521–529, 2015.
[80] Y. Naresh and C. Balaji, "Experimental investigations of heat transfer from an internally finned two phase closed thermosyphon," *Appl. Therm. Eng.*, vol. 112, pp. 1658–1666, 2017.
[81] W. Nakayama, "High-flux Heat Transfer Surface" THERMOEXCEL"," *Hitachi Rev*, vol. 24, p. 331, 1975.
[82] R. L. Webb and C. Pais, "Nucleate pool boiling data for five refrigerants on plain, integral-fin and enhanced tube geometries," *Int. J. Heat Mass Transf.*, vol. 35, no. 8, pp. 1893–1904, 1992.
[83] Z. H. Ayub and A. E. Bergles, "Pool boiling from GEWA surfaces in water and R-113," *Wärme-Stoffübertrag.*, vol. 21, no. 4, pp. 209–219, 1987.
[84] R. K. Al-Dadah and T. G. Karayiannis, "Passive enhancement of condensation heat transfer," *Appl. Therm. Eng.*, vol. 18, no. 9–10, pp. 895–909, 1998.
[85] A. E. Bergles, "Enhancement of pool boiling," *Int. J. Refrig.*, vol. 20, no. 8, pp. 545–551, 1997.
[86] "http://www.wieland-thermalsolutions.com/internet/en/products/finned_tubes/hochleistungsrohre/Hochleistungsrohre.jsp."
[87] Y. T. Kang, H. Hong, and Y. S. Lee, "Experimental correlation of falling film condensation on enhanced tubes with HFC134a; low-fin and Turbo-C tubes," *Int. J. Refrig.*, vol. 30, no. 5, pp. 805–811, 2007.
[88] M. B. Pate, Z. H. Ayub, and J. Kohler, "Heat exchangers for the air-conditioning and refrigeration industry: State-of-the-art design and technology," *Heat Transf. Eng.*, vol. 12, no. 3, pp. 56–70, 1991.
[89] D. Gstoehl and J. R. Thome, "Film condensation of R-134a on tube arrays with plain and enhanced surfaces: Part I—experimental heat transfer coefficients," *J. Heat Transf.*, vol. 128, no. 1, pp. 21–32, 2006.
[90] Z.-H. Liu, Y.-Y. Li, and R. Bao, "Compositive effect of nanoparticle parameter on thermal performance of cylindrical micro-grooved heat pipe using nanofluids," *Int. J. Therm. Sci.*, vol. 50, no. 4, pp. 558–568, 2011.
[91] "https://www.omega.ca/en/sensors-and-sensing-equipment/pressure-and-strain/pressure-transducers/p/PX654."
[92] A. Tomiyama, "Struggle with computational bubble dynamics," *Multiph. Sci. Technol.*, vol. 10, no. 4, pp. 369–405, 1998.

[93] C. F. X. Ansys, "ANSYS CFX-solver theory guide," *ANSYS CFX Release*, vol. 11, pp. 69–118, 2009.
[94] T. Frank, "Advances in computational fluid dynamics (CFD) of 3-dimensional gas-liquid multiphase flows," in *Proceedings of the NAFEMS Seminar, Niedernhausen/Wiesbaden, Germany, April*, 2005, pp. 25–26.
[95] A. D. Gosman, C. Lekakou, S. Politis, R. I. Issa, and M. K. Looney, "Multidimensional modeling of turbulent two-phase flows in stirred vessels," *AIChE J.*, vol. 38, no. 12, pp. 1946–1956, 1992.
[96] M. L. de Bertodano, R. T. Lahey, and O. C. Jones, "Turbulent bubbly two-phase flow data in a triangular duct," *Nucl. Eng. Des.*, vol. 146, no. 1, pp. 43–52, 1994.
[97] A. D. Burns, T. Frank, I. Hamill, and J.-M. Shi, "The Favre averaged drag model for turbulent dispersion in Eulerian multi-phase flows," in *5th international conference on multiphase flow, ICMF*, 2004, vol. 4.

9 Appendix

9.1 Capillary limit

As mentioned in section 1.4, for operation of heat pipe $\Delta P_{cap,max} \geq \Delta P_t$.

$$\Delta P_{cap,max} = P_{c,evap} - P_{c,cond} = \frac{2\sigma}{R_{eff,min}} cos\,\theta \quad (9.1)$$

Where θ is wetting angle, and $R_{eff,min}$ is minimum effective radius of curvature (TABLE 9-1). For having maximum pressure, liquid must be receded as far as possible into capillary structure at the evaporator end. At the condenser, liquid must flood the capillary structure.

TABLE 9-1: Minimum effective radii of curvature and wetting angles for typical fluids

Capillary structure	$R_{eff,min}$	Geometric parameter	
Circular artery	R	R	Radius of artery
Rectangular groove	w	w	Groove width
Triangle groove	w/cosβ	w	Groove width
		β	Opening angle
Screen wick/meshes	(w+d)/2	w	Mesh width
		d	Wire diameter
	1/(2N)	N	Mesh number per unit length
Sintered powders	0.41R	R	Particle radius

Total pressure drop is:

$$\Delta P_t = \Delta P_l + \Delta P_g = \Delta P_{l,fric} + \Delta P_{l,static} + \Delta P_{g,evap} + \Delta P_{g,cond} + \Delta P_{g,ad} + \Delta P_{g,static} \quad (9.2)$$

The mentioned pressure is obtained in following relation TABLE 9-2:

TABLE 9-2: Calculated parameters for equation (9.2)

Parameters	Note
$L_{eff} = \frac{1}{2}L_{evap} + L_{ad} + \frac{1}{2}L_{cond}$	L_{eff}: effective length
For groove: $\Delta p_{l,fric} = -\frac{32\vartheta_l}{A_l h_{fg} d_{c,h}^2}\dot{Q}L_{eff}$	ϑ_l=liquid kinetic viscosity A_l=cross section area of groove=$N \times A_{grrove}$ $d_{c,h}$=hydraulic diameter of capillary=$\frac{4A_{groove}}{p_{groove}}$ $\dot{Q}$=heat flux
For wick structure:	ϑ_l= liquid kinetic viscosity A_l=cross section area of channel

$\Delta p_{l,fric} = -\frac{\vartheta_l}{\widetilde{K} A_l h_{lv}} \dot{Q} L_{eff}$	$\widetilde{K}$=permeability of capillary $\dot{Q}$=heat flux
The hydrostatic pressure: $\Delta p_{l,stat} = -\rho_l g \Delta h$	For horizontal pipe is zero because $\Delta h = 0 \rightarrow$ height of fluid in channel
The hydrostatic pressure: $\Delta p_{g,stat} = 0$	For vapor static pressure is negligible. Only hydrodynamic is accounted
Parameters	**Note**
$\Delta p_{g,evap} = -\frac{32\vartheta_g}{A_{g,a} h_{fg} d_{g,h}^2} \dot{Q} \frac{L_{evap}}{2}$ $\Delta p_{g,cond} = -\frac{32\vartheta_g}{A_{g,a} h_{fg} d_{g,h}^2} \dot{Q} \frac{L_{cond}}{2}$	For laminar $Re_a = \frac{\dot{Q} d_{g,h}}{\vartheta_g \rho_g A_{g,a} h_{fg}} < 2300$ $d_{g,h}$: hydraulic diameter of channel $A_{g,a}$: axial cross section= $\pi \frac{d_{g,h}^2}{4}$
$\Delta p_{g,evap} = -\frac{0.3164\ \dot{Q}^2 L_{evap}}{\sqrt[4]{Re_a} 4 \rho_g A_{g,a}^2 h_{fg} d_{g,h}}$ $\Delta p_{g,cond} = -\frac{0.3164\ \dot{Q}^2 L_{cond}}{\sqrt[4]{Re_a} 4 \rho_g A_{g,a}^2 h_{fg} d_{g,h}}$	For turbulent $Re_a = \frac{\dot{Q} d_{g,h}}{\vartheta_g \rho_g A_{g,a} h_{fg}} > 2300$ $d_{g,h}$: hydraulic diameter of channel $A_{g,a}$: axial cross section
$\Delta p_{g,ad} = -\frac{32\vartheta_g}{A_{g,a} h_{fg} d_{g,h}^2} \dot{Q} L_{ad}$	For laminar $Re_a = \frac{\dot{Q} d_{g,h}}{\vartheta_g \rho_g A_{g,a} h_{fg}} < 2300$
$\Delta p_{g,ad} = -\frac{0.3164\ \dot{Q}^2 L_{ad}}{\sqrt[4]{Re_a} 2 \rho_g A_{g,a}^2 h_{fg} d_{g,h}}$	For turbulent $Re_a = \frac{\dot{Q} d_{g,h}}{\vartheta_g \rho_g A_{g,a} h_{fg}} > 2300$
• Note: the radial velocity and Reynolds effect is ignored due to Rer<<Rea • For Rer>>1 , pressure recovery due to inertia force, which act contrary in evaporator and condenser (about 40%) • $Re_r = \frac{\dot{Q} r_g}{\vartheta_g \rho_g A_{g,r} h_{fg}}$ where $r_g = \frac{d_{g,h}}{2}$ $and\ A_{g,r} = \pi d_{g,h} \times L$	

9.2 Euler-Euler or Two-Fluid model

In this section, interfacial momentum described in Eq (2.4) is described in detail. In following relation, it is assumed that boiling process is occurred when dispersed phase is vapor (phase *a*) and continuous phase is liquid (phase *b*).

9.2.1 Modeling lift force

The lift force influence radial distribution of phase fraction and cause bubble move towards wall or centerline of pipe based on bubble size. Lift force effect on the bubble is due to non-constant pressure distribution over a bubble. In fact assuming a spherical solid particle rising in a pipe, the relative velocity between the two phases is larger at the side with the lower liquid

velocity (i.e. at the side closer to the wall considering a turbulent liquid velocity profile) causing a lower pressure at that side that pushes the bubbles towards the pipe wall. For the sphere, the shape of the bubble the momentum is calculated:

$$M_a^l = -C_l \rho_b \alpha_a (U_r) \times \nabla \times U_b \quad (9.3)$$

When C_l is positive bubble moves towards walls and when C_l is negative bubble moves towards the centerline of pipe. C_l depends on bubble size. Experimental data and correlation from Tomiyama et al. [92] show that when D_s>5.8 mm the sign of C_l became negative and it means that larger bubble incline to move away from the wall and close to the enterline.

$$C_l = \begin{cases} \min[0.288\, tanh(0.121 Re_b), f(Eo_d)] & Eo_d < 4 \\ f(Eo_d) & 4 < Eo_d < 10 \\ -0.27 & Eo_d > 10 \end{cases} \quad (9.4)$$

$$f(Eo_d) = 0.00105 Eo_d^3 - 0.0159 Eo_d^2 - 0.0204 Eo_d + 0.474 \quad (9.5)$$

$$Eo_d = \frac{(\rho_b - \rho_a) g d_h^2}{\sigma} \quad (9.6)$$

$$d_h = D_s (1 + 0.163 E_o^{0.757})^{1/3} \quad (9.7)$$

Where Eo_d is modified Eotvos number describing the ratio between buoyancy force and those from surface tension. Another correlation is suggested by Rusche [58] and predict a positive value for *Cl*, which directly depends on phase fraction. In order to prevent fluctuation in cells close to walls, Cl option is turned off [92].

$$C_l = 6.51 \times 10^{-4} \alpha_a^{-1.2} \quad (9.8)$$

9.2.2 Modeling drag force

The drag force is a resistance opposed to the motion of bubble in the fluid and it depends on bubble size and relative velocity between two phases.

$$M_a^d = -\frac{3}{4} \frac{C_d}{D_s} \rho_b \alpha_a |U_r| U_r \quad , U_r = U_a - U_b \quad (9.9)$$

Where *a* is vapor and *b* is liquid phase. D_s is the mean Sauter bubble diameter (diameter of a sphere that has the same volume/surface ratio) and C_d is drag coefficient. Ghione [10] introduce various correlation for calculation of C_d but they all have the same problem. These models are only valid for spherical particles and low Reynolds number regimes. In high Reynolds number

when bubbles are distorted and deformed, these model are not suitable and do not have enough precision for modeling. Therefore, he used other models, which are implemented in CFX manual. In new models, distortion and deformation of bubble and shape of bubble on drag force take account.

1) The Ishii-Zuber [93] model for densely distributed fluid particles
   - For sphere shape:

$$C_d(sphere) = \frac{24}{Re_{bm}}\left(1 + 0.15Re_{bm}^{0.687}\right) \quad , Re_{bm} = \frac{\rho_b|U_a - U_b|D_s}{\mu_m} \ , \qquad (9.10)$$

$$\mu_m = \mu_b(1 - \frac{\alpha_a}{\alpha_{max}})^{-2.5\alpha_{max}\mu^*}, \mu^* = \frac{\mu_a + 0.4\mu_b}{\mu_a + \mu_b}$$

Here $\alpha_{max}$is the phase fraction at the maximum packing equal to 0.52 and $\mu^*$is dimensionless dynamical viscosity.

   - For ellipse shape:

$$C_d(ellipse) = E(\alpha_a)C_{d\infty} \ , C_{d\infty} = \frac{2}{3}E_0^{1/2} \ , E_0 = \frac{(\rho_b - \rho_a)gD_s^2}{\sigma} \qquad (9.11)$$

$$E(\alpha_a) = \frac{1 + 17.67f(\alpha_a)^{6/7}}{18.67f(\alpha_a)} \quad , f(\alpha_a) = \frac{\mu_b}{\mu_m}(1 - \alpha_a)^{1/2}$$

   - For cap shape:

$$C_d(cap) = C_{d\infty}(1 - \alpha_a)^2 \quad in\ this\ case\ C_{d\infty} = \frac{3}{8} \qquad (9.12)$$

According CFD algorithm, an automatic regime selection is applied.

$$C_d = C_d(sphere) \qquad if\ C_d(sphere) \geq C_d(ellipse) \quad (9.13)$$

$$C_d = \min[C_d(ellipse), C_d(cap)] \qquad if\ C_d(sphere) \leq C_d(ellipse) \quad (9.14)$$

2) The Ishii-Zuber model [93] for sparsely distributed fluid particles
   - For sphere shape:

$$C_d(sphere) = \frac{24}{Re_{bm}}\left(1 + 0.15Re_{bm}^{0.687}\right) \qquad (9.15)$$

   - For ellipse shape:

$$C_d(ellipse) = C_{d\infty} \ = \frac{2}{3}E_0^{1/2} \ , E_0 = \frac{(\rho_b - \rho_a)gD_s^2}{\sigma} \qquad (9.16)$$

- For cap shape:

$$C_d(cap) = C_{d\infty} = \frac{3}{8} \qquad (9.17)$$

According CFD algorithm, an automatic regime selection is applied [92].

$$C_d = \max[C_d(sphere), C_d(dist)] \quad where\ C_d(dist) = \min[C_d(ellipse), C_d(cap)] \quad (9.18)$$

9.2.3 Modeling virtual mass force

Acceleration and deceleration of bubble inside of fluid add inertia force (virtual mass or added mass forces) to the system, which added to the model. This term has fewer effects rather than other term and when we deal with steady state condition, due to zero value of acceleration, this term is zero. However, the effects of this term considered because this term has a stabilizing effect on the solution procedure. Two models suggested for estimation of virtual mass as below [92]:

First model: $M_a^{vm} = -C_{vm}\rho_b\alpha_a\left(\frac{DU_a}{Dt} - \frac{DU_b}{Dt}\right)$, $C_{vm} = 0.5$ (9.19)

Second model: $M_a^{vm} = -\frac{1}{2}\rho_b\alpha_a\frac{1+2\alpha_a}{1-\alpha_a}\left(\frac{DU_a}{Dt} - \frac{DU_b}{Dt}\right)$ (9.20)

9.2.4 Modeling wall lubrication force

Wall lubrication force is a repulsive force which is shown in experiments. it prevents the concentration of phase fraction and bubble close the walls [92]. In other words, if bubble concentrated close to the wall, they are never attached to it. Regard to Frank et al. [94] work, the wall lubrication model is calculated:

$$M_a^{wl} = C_w\rho_b\alpha_a|U_r - (U_r.n_w)n_w|^2(-n_w) \qquad (9.21)$$

Where n_w is a normal vector to the wall, $U_r - (U_r.n_w)n_w$ is the projection of relative velocity parallel to the wall. The C_w coefficient must be positive in order to push away bubbles from walls. There are three models to estimate C_w and the best model matches better with experimental data is Tomiyama model [92].:

$$C_w = \frac{1}{2}C_{wl}D_s\left(\frac{1}{y_w^2} - \frac{1}{(D_{pipe}-y_w)^2}\right) \qquad (9.22)$$

$$C_{wl} = \begin{cases} 0.47 & E_o < 1 \\ \exp(-0.923E_o + 0.179) & 1 < E_o < 5 \\ 0.00599\,E_o - 0.0187 & 5 < E_o < 33 \\ 0.179 & E_o > 33 \end{cases} \quad \text{(Equation 9.23)}$$

9.2.5 Modeling turbulent dispersion force

This force is due to turbulent fluctuation effects on liquid velocity and bubble movement. Reduction in turbulent dispersion force leads to sharp peak in phase fraction in close cells near walls. This term depends on gradient of phase fraction and causes instability in results. Actually, it plays an important role in radial phase fraction distribution. There are three models, which used in [92].:

The Gosman model [95]:

$$M_a^{td} = -\frac{3}{4} C_d \frac{\rho_b}{D_s} \frac{\vartheta_b^t}{\sigma_t} |U_r| \nabla \alpha_a \qquad (9.24)$$

Where $\sigma_t = 0.9$ and Cd is Schiller-Naumann Drag force coefficient.

The Lopez and Bertodono model [96]: (stable and best performance model)

$$M_a^{td} = -C_{td} \rho_b k_b \nabla \alpha_a \quad , C_{td} = 1 \quad (9.25)$$

The Burns model [97]:(the simplified model)

$$M_a^{td} = -\frac{3}{4} C_d \frac{\rho_b}{D_s} \frac{\vartheta_b^t}{\sigma_t} U_r \frac{1}{1-\alpha_a} \nabla \alpha_a \quad (9.26)$$

Where $\sigma_t = 0.9$ and C_d is Schiller-Naumann Drag force coefficient [92].

9.2.6 Two-phase turbulent modeling using k-ε

If k-ε model is used for turbulent flow, some terms (additional source terms in effects of dispersed phase on turbulent) add to k and ε transport equations:

$$\frac{\partial k_b}{\partial t} + (\overline{U}_b . \nabla) k_b - \nabla . \left(\frac{\vartheta_b^{eff}}{\sigma_k} \nabla k_b \right) = P_b - \varepsilon_b + S_k \qquad (9.27)$$

$$\frac{\partial \varepsilon_b}{\partial t} + (\overline{U}_b . \nabla) \varepsilon_b - \nabla . \left(\frac{\vartheta_b^{eff}}{\sigma_\varepsilon} \nabla \varepsilon_b \right) = \frac{\varepsilon_b}{k_b} (C_1 P_b - C_2 \varepsilon_b) + S_\varepsilon \qquad (9.28)$$

$$P_b = 2\vartheta_b^{eff} (\nabla \overline{U}_b . dev\, (\nabla \overline{U}_b + (\nabla \overline{U}_b)^T)$$

$$\vartheta_b^{eff} = \vartheta_b + \vartheta^t \quad ,\vartheta^t = C_\mu \frac{k_b^2}{\varepsilon_b}$$

C_μ	C_1	C_2	C_3	σ_k	σ_ε	σ_α	C_i
0.09	1.44	1.92	1.0	1.0	1.3	1.0	C_t

The additional two-phase source terms are

$$S_k = \frac{2k_b\alpha_a A_d(C_i-1)}{\rho_b} + \frac{A_d\vartheta^t}{\rho_b\sigma_\alpha}\frac{\nabla\alpha_a}{\alpha_b}.\bar{U}_r \qquad (9.29)$$

$$S_\varepsilon = \frac{2C_3\varepsilon_b\alpha_a A_d(C_i-1)}{\rho_b} \qquad (9.30)$$

A_d is drag multiplier term and C_i is equal to the turbulence response function: $C_i = C_t$. A_d can be calculated based on relation proposed by Gosman et al. [95]:

$$A_d = \alpha_a \frac{3}{4}\frac{\rho_b}{d_a} C_d|\bar{U}_r| \quad \rightarrow Gosman\ et\ al. relation \qquad (9.31)$$

Where d_a is diameter of a DPE, C_d is drag coefficient, ρ_b is density of phase b and $\bar{U}_r$ is relative velocity. C_t is defined as the ratio of r.m.s of dispersed phase velocity fluctuation to those of the continuous phase given by:

$$C_t = \frac{\acute{U}_a}{\acute{U}_b} \qquad (9.32)$$

For calculation of C_t, the model proposed by Issa is used:

$$C_t = \frac{3+\beta}{1+\beta+2\rho_d/\rho_b} \qquad \beta = \frac{2A_d L_e^2}{\rho_b\vartheta_b Re_t} \qquad (9.33)$$

Where ϑ the kinematic viscosity of continuous phase and R_{et} is is turbulence Reynolds based on eddy length scale L_e and the r.m.s of liquid velocity fluctuation.

9.3 Mass and Heat flux at boundary and bulk fluid

In OpenFOAM, there is two different models for estimation of heat flux at boundary and inside of fluid. The wall heat flux was the main concern of this thesis and described in details in chapter

3, 4 and 5. In this section, relations for calculation of mass and heat flux at bulk fluid is explained.

9.3.1 Interphase heat transfer (boiling or condensation) inside of bulk fluid

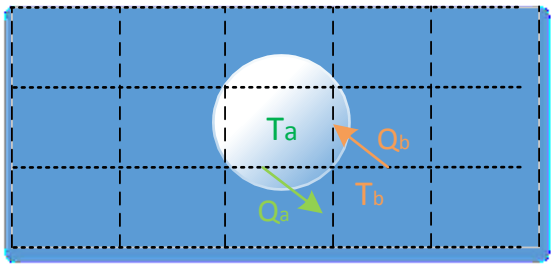

Note: Phase *a*→ vapor or dispersed phase , phase *b*→ liquid or continuous phase

$$\frac{\partial(\rho_a\alpha_a i_a)}{\partial t}+\nabla.(\rho_a\alpha_a i_a \vec{\upsilon}_a)=-\nabla.[\alpha_a(\vec{q}_a+\vec{q}_{a,t}+\cdots_a \frac{DP}{Dt}+(\Gamma^+_{ab}i_b-\Gamma^+_{ba}i_a)+Q_i+q''_w A''_w \quad (9.34)$$

Q_i denotes interphase heat transfer from phase *a* to *b* across interfaces with other phases. It is directly related to temperature changes between two phases.

9.3.1.1 Thermal phase change model

In this approach, mass and heat flux is estimated based on this assumption: interfacial temperature is equal to saturation temperature $T_{int}=T_{sat}$.

Interphase heat transfer occurs due to thermal non-equilibrium (temperature difference) across phase interfaces. The total heat per unit volume transferred to phase *a* due to interaction with other phases *b* is given by:

$$Q_i \rightarrow Q_{ab}=h_{ab}a_i(T_a-T_b) \quad (9.35)$$

It is convenient to express the heat transfer coefficient in terms of a dimensionless Nusselt number: In the particle model, the thermal conductivity scale λ is taken to be the thermal conductivity of the continuous phase, and the length scale d is taken to be the mean diameter of the dispersed phase:

$$h_{ab} = \frac{\lambda_b Nu_{ab}}{d_a} \quad (9.36)$$

For laminar forced convection around a spherical particle, theoretical analysis shows that *Nu=2*. For a particle, the Nusselt number is a function of *Re* and *Pr*. We can use from following relation as below:

$$Nu_{ab} = 2 + 0.6\,\mathrm{Re}_{ab}^{1/2}\,\mathrm{Pr}_{ab}^{1/3}$$
$$\mathrm{Re}_{ab} = \frac{\rho_b |U_a - U_b|}{\mu_b}, \quad \mathrm{Pr}_{ab} = \frac{\mu_b C_{p,b}}{\lambda_b} \quad (9.37)$$

In OpenFoam, they define a coefficient called K which convert energy equation to simple model:

$$\frac{\partial(\rho_a \alpha_a i_a)}{\partial t} + \nabla.(\rho_a \alpha_a i_a \vec{U}_a) - - \nabla.[\alpha_a(\vec{q}_a \cdot \vec{q}_a) \cdot \cdot_{ab} i_b - \Gamma^{+}_{ba} i_a) + Q_i + q''_w A''_w$$

$\mathrm{K}(T_a - T_b)$

```
// Member Functions

    //- The heat transfer function K used in the enthalpy equation
    //    ddt(alpha1*rho1*ha) + ... = ... K*(Ta - Tb)
    //    ddt(alpha2*rho2*hb) + ... = ... K*(Tb - Ta)
    tmp<volScalarField> K() const;

    //- The heat transfer function K used in the enthalpy equation
    //    ddt(alpha1*rho1*ha) + ... = ... K*(Ta - Tb)
    //    ddt(alpha2*rho2*hb) + ... = ... K*(Tb - Ta)
    //  with a specified residual volume fraction
    virtual tmp<volScalarField> K(const scalar residualAlpha) const = 0;
```

For modeling of K, one assumes that dispersed phase is spherical and surrounded by continuous phase, then:

- Ranz-Marshall: $K = hA = \frac{6\alpha_a \lambda_b Nu_{ab}}{d_a^2}, where \quad A = \frac{6\alpha_a}{d_a}$
- Spherical model: $K = hA = \frac{6\alpha_a \lambda_b}{d_a^2}$

Note: $k_{appa} = \lambda$ is thermal conductivity coefficient and calculated for continuous phase.

Re	`magUr()*dispersed().d()/continuous().nu();`	$\mathrm{Re}_{ab} = \frac{\rho_b \lvert U_a - U_b \rvert}{\mu_b}$

Pr	continuous().nu() *continuous().thermo().Cpv() *continuous().rho() /continuous().kappa();	$\mathrm{Pr}_{ab} = \frac{\mu_b C_{p,b}}{\lambda_b}$

9.3.2 Interphase mass transfer (boiling or condensation) inside of bulk fluid

As mentioned in Chapter 2.3.2, a portion of mass transfer happened inside of bulk fluid. For example when vapor surrounded by liquid, it is collapsed and transfer its heat to liquid. On the hand, when liquid surrounded by hot vapor, it can be evaporated. In this section, method for calculation of interfacial mass transfer is presented. According to the case, this interfacial can be related to condensation or evaporation.

9.3.2.1 Thermal phase change model

In this approach, mass flux is estimated based on this assumption: interfacial temperature is equal to saturation temperature. It means the interface temperature is calculated such that the net rate at which the heat is transferred to the interface is equal to the latent heat consumed by the mass transfer.

Total heat flux to phase *a*: $Q_a = q_a + \dot{\imath}$

Total heat flux to phase *b*: $Q_b = q_b + \dot{\imath}$

Where: $q_a = h_a(\mathrm{T}_s - \mathrm{T}_a)$ and $q_b = h_b(\mathrm{T}_s - \mathrm{T}_b)$

h_a, h_b are heat transfer coefficient of phase *a* and phase *b*. The interfacial temperature is determined by thermodynamic equilibrium assumption, so $T_s = T_{sat}$

The total heat balance at interface lead us to this equation:

$$\dot{\imath} \qquad \frac{q_b}{\imath_{bs} - i_{as}} \qquad 9.38)$$

$i_{\alpha s}, i_{\beta s}$ Represent interfacial value of enthalpy carried into and out due to phase change

If $\dot{\imath}$ $\qquad i_{as} = i_{a,sat}, i_{bs} = i_b \rightarrow evaporation$

If $\dot{\imath}$ $\qquad i_{as} = i_a, i_{bs} = i_{b,sat} \rightarrow condensation$

In openFoam, different notation is presented for parameters as below $\dot{m}_{ab}$=iDmdt

```
iDmdt =
    (1 - iDmdtRelax)*iDmdt
  + iDmdtRelax*(H1*(Tf - T1) + H2*(Tf - T2))
   /min
    (
        (pos(iDmdt)*he2 + neg(iDmdt)*hef2)
      - (neg(iDmdt)*he1 + pos(iDmdt)*hef1),
        0.3*mag(hef2 - hef1)
    );
```

$$\dot{m}_{ab} = \frac{H_1(T_f - T_1) + H_2(T_f - T_2)}{h_{ef1} - h_{ef2}} \quad (9.39)$$

H_1,H_2: heat transfer coefficient calculated by Ranz-Marshall or Spherical model (see previous section)

h_{ef1}, h_{ef2}: specific enthalpy at interface,

T_f=interfacial temperature →T_f=T_{sat}

```
*eqns[name] += fvm::Sp(dmdt21, eqns[name]->psi()) - dmdt21;
*eqns[otherName] += dmdt12 - fvm::Sp(dmdt12, eqns[otherName]->psi());
```